

**IMPROVING SHALLOW-WATER MULTIBEAM TARGET DETECTION AT
LOW GRAZING ANGLES**

by

Douglas Luiz da Silva Pereira

B.Sc. Naval Sciences, Brazilian Naval School, 2003
Extension Course in Hydrography (IHO Category “A”), Brazilian Navy Directorate of
Hydrography and Navigation, 2006

A Thesis Submitted in Partial Fulfillment
of the Requirements for the Degree of

Master of Science in Engineering

in the Graduate Academic Unit of Geodesy and Geomatics Engineering

Supervisor: J. E. Hughes Clarke, Ph.D., Geodesy and Geomatics Engineering

Examining Board: Marcelo C. Santos, Ph.D., Geodesy and Geomatics Engineering
Jonathan Beaudoin, Ph.D., QPS Canada Ltd.

This thesis is accepted by the
Dean of Graduate Studies

THE UNIVERSITY OF NEW BRUNSWICK

July, 2015

©Douglas Luiz da Silva Pereira, 2015

ABSTRACT

Beyond approximately 60° incidence angle, many modern multibeam echo sounders have difficulty maintaining sufficient depth accuracy and seabed target detection to comply with International Hydrographic Organization (IHO) standards. In some cases, a target at such a low grazing angle is not detected due to limitations of the existing bottom detection method and filters applied by the manufacturer. In lieu of clear positive bathymetric indicators, a data gap within the bathymetric surface or a shadow in the backscatter image may be the only indication of the presence of that target.

This research presents a refined bottom detection algorithm based on the Bearing Direction Indicator (BDI) method. The BDI approach can markedly improve target detection capability at low grazing angles in shallow waters by independently discriminating each echo's direction of arrival irrespective of the beam spacing. The algorithm can be applied in post-processing as long as the water column data is retained. Two test datasets were collected using an EM 2040D employing angular sectors as wide as $\pm 82^\circ$. Data were acquired over a site with multiple IHO-compliant anthropogenic objects to assess the EM 2040D ability to detect low-grazing-angle targets prior to, and after, application of the newly developed algorithm. Results obtained clearly illustrate that the BDI algorithm can enhance low-grazing-angle target detection/definition.

DEDICATION

This thesis is dedicated to my beloved wife, Luciani Steffen Pereira, for her constant support and incentive.

ACKNOWLEDGEMENTS

This thesis is certainly not an individual accomplishment. Many people and institutions somehow helped me out to achieve my objectives. For that reason, I thank:

- my wife Luciani, for her emotional and psychological support at the comfort of our home in Fredericton. Her love and care kept me motivated to pursue my master degree.
- my mother Eliane, my father Carlos, and my sisters Karla and Karina, for their stimuli coming out from Brazil.
- the Brazilian Navy, for giving me the opportunity to study abroad and for supporting me financially. I am sure the knowledge I have acquired during these two years will be of upmost usefulness in my hydrographic career.
- my supervisor Dr. John E. Hughes Clarke, for guiding me throughout this work. It was a great experience to be supervised by a world-renowned hydrographic professor and researcher.
- Dr. Marcelo Santos and Dr. Jonathan Beaudoin, for the willingness to assess this thesis. Their comments and suggestions were extremely welcome.
- Cdr. Aluizio, Lt. Cdr. Adriano Vieira, and Lt. Cdr. Rodrigo Carvalho, all from the Brazilian Navy, for the general support and technical guidance before and during this work.
- the NavO (U.S. Navy), for giving me the opportunity to partake with them in a hydrographic data collection mission using an EM 2040D, and also for providing me the data I used to test the algorithm developed to support this thesis.

- everyone in the Department of Geodesy and Geomatics Engineering of the UNB, especially those from the Ocean Mapping Group (OMG), for the knowledge exchange and friendly sociability.

Table of Contents

| | |
|---|------|
| ABSTRACT | ii |
| DEDICATION | iii |
| ACKNOWLEDGEMENTS | iv |
| Table of Contents | vi |
| List of Tables..... | viii |
| List of Figures | ix |
| List of Symbols, Nomenclature or Abbreviations..... | xi |
| 1. Introduction | 1 |
| 1.1 Problem Statement..... | 1 |
| 1.2 Research Questions | 7 |
| 1.3 Research Objectives | 7 |
| 1.4 Thesis Structure | 7 |
| 2. Background | 9 |
| 2.1 Bottom Detection Methods..... | 9 |
| 2.1.1 Overview..... | 9 |
| 2.1.2 Weighted Mean Time (WMT)..... | 11 |
| 2.1.3 Bearing Direction Indicator (BDI)..... | 13 |
| 2.1.4 Phase Detection | 17 |
| 2.1.5 High Definition Beam Forming (HDBF) | 20 |
| 2.2 MBES Kongsberg® EM 2040D..... | 22 |
| 2.3 Discussion of Previous Works..... | 24 |
| 3. Methodology | 31 |
| 3.1 Overview | 31 |
| 3.2 DOA Refinement..... | 33 |
| 3.2.1 Overview..... | 33 |
| 3.2.2 Three-Point Parabola Fitting..... | 40 |
| 3.2.3 Five-Point Parabola Fitting..... | 43 |
| 3.3 Number of BDI Solutions per TWTT | 46 |
| 3.4 Detection Thresholding | 49 |
| 3.4.1 Manual Thresholding..... | 49 |
| 3.4.2 Automatic Thresholding | 53 |
| 3.5 Sector Boundaries..... | 58 |

| | | |
|-------|------------------------------------|----|
| 3.6 | Minimum Slant Range (MSR)..... | 60 |
| 3.7 | Filtering | 62 |
| 3.8 | Compression | 67 |
| 4. | Tests, Results, and Analyses | 73 |
| 4.1 | Test Area | 73 |
| 4.2 | Test Data..... | 74 |
| 4.3 | Target Detection Criterion..... | 75 |
| 4.4 | Data Presentation..... | 77 |
| 4.5 | Results and Analyses | 78 |
| 4.5.1 | 1-meter cube at 40 m depth | 78 |
| 4.5.2 | 1-meter cube at 20 m depth | 84 |
| 4.5.3 | 0.5-meter cube at 20 m depth | 89 |
| 5. | Conclusions | 95 |
| 5.1 | Summary..... | 95 |
| 5.2 | Future Work..... | 96 |
| 5.3 | Contribution..... | 97 |
| | Bibliography..... | 98 |
| | Curriculum Vitae | |

List of Tables

| | |
|---|----|
| Table 1.1: Maximum allowable TVU coefficients (after IHO special publication S-44, 2008) | 2 |
| Table 1.2: Feature (or target) detection standards (after IHO special publication S-44, 2008) | 4 |
| Table 2.1: EM 2040D main specifications..... | 23 |
| Table 4.1: 1-meter cube at 40 m depth - manual threshold BDI, 2013 dataset, +67° incidence angle..... | 79 |
| Table 4.2: 1-meter cube at 40 m depth - automatic threshold BDI, 2013 dataset, +67° incidence angle..... | 80 |
| Table 4.3: 1-meter cube at 40 m depth - manual threshold BDI, 2014 dataset, +68° incidence angle..... | 81 |
| Table 4.4: 1-meter cube at 40 m depth - automatic threshold BDI, 2014 dataset, +68° incidence angle..... | 82 |
| Table 4.5: 1-meter cube at 20 m depth - manual threshold BDI, 2013 dataset, -65° incidence angle..... | 85 |
| Table 4.6: 1-meter cube at 20 m depth - automatic threshold BDI, 2013 dataset, -65° incidence angle..... | 86 |
| Table 4.7: 1-meter cube at 20 m depth - manual threshold BDI, 2013 dataset, +71° incidence angle..... | 87 |
| Table 4.8: 1-meter cube at 20 m depth - automatic threshold BDI, 2013 dataset, +71° incidence angle..... | 88 |
| Table 4.9: 0.5-meter cube at 20 m depth - manual threshold BDI, 2013 dataset, +57° incidence angle..... | 90 |
| Table 4.10: 0.5-meter cube at 20 m depth - automatic threshold BDI, 2013 dataset, +57° incidence angle..... | 91 |
| Table 4.11: 0.5-meter cube at 20 m depth - manual threshold BDI, 2014 dataset, +70° incidence angle..... | 92 |
| Table 4.12: 0.5-meter cube at 20 m depth - automatic threshold BDI, 2014 dataset, +70° incidence angle..... | 93 |

List of Figures

| | |
|--|----|
| Figure 1.1: MBES depth uncertainty \times depth-dependent TVU portion (Special Order) ... | 3 |
| Figure 1.2: Example of an undetected 1-meter cube at low grazing angles in shallow waters (after Hughes Clarke <i>et al.</i> , 2013) | 6 |
| Figure 2.1: Understanding the water column pie (A) and time-angle (B) diagrams (same swath) | 10 |
| Figure 2.2: Within-beam sound wave interaction with seafloor | 12 |
| Figure 2.3: BDI bottom detection method: determining maximal amplitude directions, given the sound wave two-way travel time | 13 |
| Figure 2.4: The influence of the beam pattern over the record of echo amplitudes as a result of the sound wave being reflected back by a point scatterer (four beams example) | 14 |
| Figure 2.5: BDI accuracy and its dependence on incidence angle | 16 |
| Figure 2.6: Receiver split-aperture (after Hughes Clarke, 2013b) | 17 |
| Figure 2.7: Illustrating the zero-phase crossing identification for normal (noisier) and oblique incidence | 18 |
| Figure 2.8: Example of a linear regression to estimate the zero-phase crossing | 19 |
| Figure 2.9: High definition beam forming (HDBF) (from Nilsen, 2012) | 21 |
| Figure 2.10: Example of an EM 2040D transducers installation (after Hughes Clarke <i>et al.</i> , 2013) | 23 |
| Figure 2.11: The within-beam common slant range (layover) phase disturbance | 27 |
| Figure 2.12: WMT arc of solutions when facing a high-aspect-ratio target (after Hughes Clarke, 2009) | 28 |
| Figure 2.13: One-swath across-track WCI (section) highlighting the inboard edge (green circle) of the undetected 1-meter cube presented in Figure 1.2 (after Hughes Clarke <i>et al.</i> , 2013) | 29 |
| Figure 3.1: The preexisting OMG Swathed WC Toolkit (top) and the new BDI widget (bottom) | 32 |
| Figure 3.2: Preliminary BDI solutions based on choosing peak intensity, resulting in poor angular discrimination | 34 |
| Figure 3.3: Angle series plot when echo direction coincides with a beam axis (three beams illustration) | 36 |
| Figure 3.4: Angle series plot when echo direction is not coincident with a beam axis (three beams illustration) | 36 |
| Figure 3.5: The effective receiver main-lobe beamwidth and its relationship with the maximum allowable beam spacing for the viability of BDI parabola fitting | 39 |
| Figure 3.6: Example of three-point parabola fitting using the Lagrange Formula | 42 |
| Figure 3.7: Closest peak \times three-point parabola BDI (same seafloor section) | 43 |
| Figure 3.8: Example of five-point parabola fitting using Least Squares Approximation | 45 |
| Figure 3.9: Closest peak \times three-point \times five-point parabola BDI (same seafloor section) | 46 |
| Figure 3.10: The variable number of BDI solutions per TWTT | 47 |
| Figure 3.11: The maximum number of two BDI solutions per time slice in the developed algorithm | 48 |

| | |
|---|----|
| Figure 3.12: The minimum height of target (H) to get base and top at the same time, considering a maximum of two BDI solutions per time slice | 48 |
| Figure 3.13: Example of an user-defined threshold for a particular EM 2040S swath..... | 50 |
| Figure 3.14: Within-swath linearly variable manual threshold..... | 51 |
| Figure 3.15: Comparing fixed with linearly variable manual threshold | 52 |
| Figure 3.16: Automatic threshold algorithm – Step 1 | 53 |
| Figure 3.17: Automatic threshold algorithm – Step 2..... | 54 |
| Figure 3.18: Automatic threshold algorithm – Step 3 (case 1) | 55 |
| Figure 3.19: Automatic threshold algorithm – Step 3 (case 2) | 56 |
| Figure 3.20: The limitation on the minimum number of three peaks required to allow automatic thresholding calculation | 57 |
| Figure 3.21: Illustrating the boundary region between sectors (after Hughes Clarke, 2013b) | 58 |
| Figure 3.22: Example of a data gap on the sector boundaries caused by the application of five-point parabola BDI | 59 |
| Figure 3.23: The MSR identification in the WC pie diagram..... | 60 |
| Figure 3.24: The MSR identification based on the plot of the mean of all peaks for each time slice | 61 |
| Figure 3.25: False BDI solutions in manual threshold..... | 62 |
| Figure 3.26: False BDI solutions in automatic threshold..... | 63 |
| Figure 3.27: Maximum allowable sample-number-based standard deviation (σ_{\max})..... | 64 |
| Figure 3.28: The within-beam BDI filtering process (final step)..... | 65 |
| Figure 3.29: Comparing before and after filtering for manual threshold BDI (Filter Index = 9) | 66 |
| Figure 3.30: Comparing before and after filtering for automatic threshold BDI (Filter Index = 9) | 66 |
| Figure 3.31: Comparing BDI solutions before and after filtering in the vicinity of a 1-meter cube at 40 m depth (Filter Index = 9)..... | 67 |
| Figure 3.32: Illustrating the 1 st , 2 nd , and 3 rd steps of the compression algorithm | 69 |
| Figure 3.33: Illustrating the 4 th step of the compression algorithm | 70 |
| Figure 3.34: Illustrating the 5 th step (final) of the compression algorithm | 71 |
| Figure 3.35: Comparing before (top) and after (bottom) application of the compression algorithm (400 virtual beams)..... | 72 |
| Figure 4.1: Test Area..... | 73 |
| Figure 4.2: Target schema of the test area | 74 |

List of Symbols, Nomenclature or Abbreviations

| | |
|------|--|
| BDI | Bearing Direction Indicator (or Beam Deviation Indicator) |
| BSL | Backscatter strength level |
| DOA | Direction of arrival |
| HDBF | High definition beam forming |
| IHO | International Hydrographic Organization |
| KM | Kongsberg® Maritime |
| MBES | Multibeam echo sounder(s) |
| MLO | Mine-like object |
| MSR | Minimum slant range |
| NavO | United States Navy's Naval Oceanographic Office |
| OMG | Ocean Mapping Group |
| SNR | Signal-to-noise ratio |
| S-44 | Special Publication N° 44 – IHO Standards for Hydrographic Surveys |
| TOA | Time of arrival |
| TVG | Time varying gain |
| TVU | Total vertical uncertainty |
| TWTT | Two-way travel time |
| WC | Water column |
| WCI | Water column imagery |
| WMT | Weighted Mean Time |

1. Introduction

1.1 Problem Statement

Multibeam echo sounders (MBES), in comparison with single beam echo sounders, provide larger seafloor coverage due to the use of multiple beams distributed over an angular sector oriented transversally to the ship. This capability allows MBES users to ensonify the bottom at incidence angles other than simply the nadir direction. However, the data quality from the inner beams, including both accuracy and resolution, is generally significantly better than those from the outer beams.

Most single-head MBES have an angular coverage of approximately 130° (or $\pm 65^\circ$). Dual-head MBES, in contrast, can potentially cover the entire sector (180°) underneath the ship. Even with dual receivers, however, for the purpose of seabed mapping, usable angular coverage is generally limited due to factors such as sound wave attenuation, refraction, and weak low-grazing-angle backscattering. In shallow waters (less than 40 m), sectors of up to approximately 160° to 170° are possible. Nevertheless, beyond approximately 120° (or $\pm 60^\circ$), both depth accuracy and target detection capability degrade rapidly.

International Hydrographic Organization (IHO) special publication S-44 - IHO Standards for Hydrographic Surveys, 5th edition, 2008, classifies hydrographic surveys into four different orders (Special, 1a, 1b, and 2) and defines minimum standards for each of them. Special Order survey places the most stringent requirements, followed by 1a, 1b, and 2 in this sequence. In shallow waters, as a reflection of the highest concerns with the safety of navigation, the majority of surveys are required to meet Special Order specifications. Within all S-44 standards, two of them are of special interest in this

study: maximum allowable total vertical uncertainty (TVU) and feature (or target) detection.

Vertical uncertainty is the uncertainty of the reduced depths. Maximum allowable TVU at 95% confidence level is defined by the formula $\pm\sqrt{a^2 + (b \times d)^2}$, where

a represents the portion of the uncertainty that does not vary with depth,

b is a coefficient that represents the portion of the uncertainty that varies with depth,

d is the depth, and

$b \times d$ represents the portion of the uncertainty that varies with depth.

Coefficients a and b , presented in Table 1.1, are order-dependent values.

Table 1.1: Maximum allowable TVU coefficients (after IHO special publication S-44, 2008)

| | | Survey Order | | | |
|--------------|--------------|--------------|-----|-----|-----|
| | | Special | 1a | 1b | 2 |
| Coefficients | a (meters) | 0.25 | 0.5 | 0.5 | 1.0 |
| | b (%) | 0.75 | 1.3 | 1.3 | 2.3 |

Considering a normal distribution of errors for the depths (one dimensional quantity), the standard deviation (σ) scale factor at 95% confidence level is equal to 1.96. Thus, simply analyzing the depth-dependent vertical uncertainty $b \times d$, its expression can be rewritten in terms of 1σ as $(b \times d)/1.96$. For a Special Order survey, the depth-dependent vertical uncertainty (1σ) is equal to approximately $0.0038 \times d$ (or $0.38\% \times d$).

Under ideal oceanographic and weather conditions, and also considering correct and calibrated installation and good quality external sensors (position, velocity, motion,

and sound speed), most modern MBES provide an uncertainty (1σ) of ± 0.1 to 0.2% of the depth, which is comfortably below the Special Order depth-dependent vertical uncertainty $0.38\% \times d$. However, that value is only achievable up to approximately 60° incidence angle. Beyond that, it worsens rapidly as the angle grows. Therefore, for some incidence angle over 60° , it is expected that the MBES uncertainty overpasses the depth-dependent TVU portion, $(b \times d)/1.96$ (equal to $0.38\% \times d$ for a Special Order Survey). Figure 1.1 illustrates this concept.

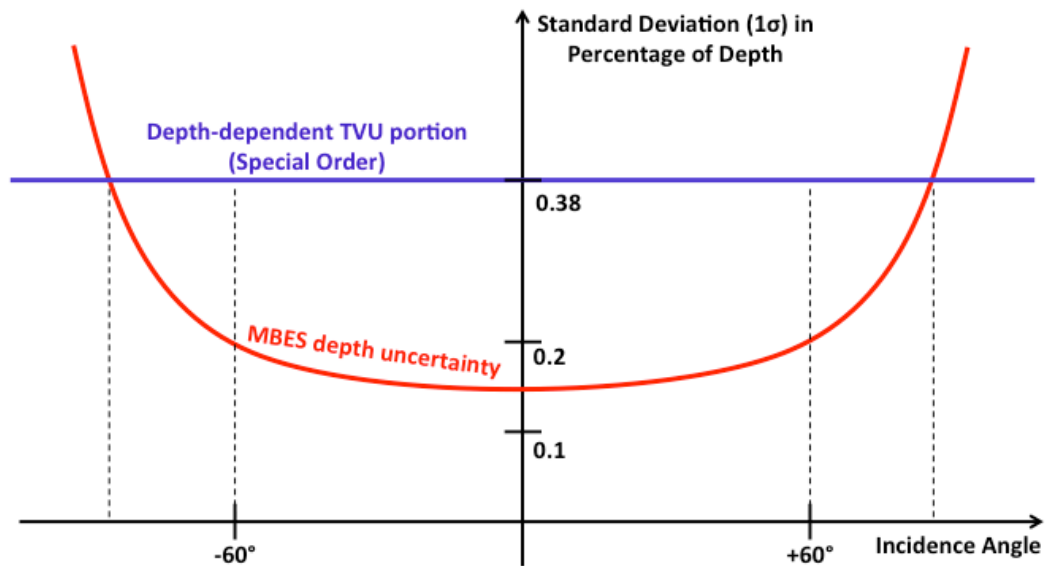


Figure 1.1: MBES depth uncertainty \times depth-dependent TVU portion (Special Order)
Generic illustration showing points somewhere beyond $\pm 60^\circ$ incidence angle where MBES depth uncertainty overcomes the depth-dependent TVU portion (Special Order survey in shallow waters)

Imperfect compensation for refraction is the predominant factor degrading depth accuracy in the outer beams. Beams close to horizontal are more susceptible to errors in depth measurement, especially in an environment with rapidly varying sound velocity structure. In this case, many successive layers (with their own uncertainties) associated

with high beam incidence angle lead to greater depth errors. Roll sensor errors, in particular, greatly contribute to the depth accuracy degradation away from nadir. Small roll errors are disproportionately detrimental to the outer beam data. Due to these amplified errors, generally, users do not rely on bathymetric data beyond approximately 60° incidence angle. Many users simply disregard these data without conducting further analysis.

However, note that even with the MBES depth uncertainty increasing quickly beyond 60° and certainly overpassing the depth-dependent TVU portion at some point, the constant a allows the overall maximum allowable TVU to become a greater percentage of the depth as it gets shallower. Thus, in shallower waters, especially those with stable water masses such as well-mixed fresh water rivers, wider swaths can be considered, if only depth accuracy is required.

Regarding target detection, as with depth accuracy, IHO special publication S-44 places order-dependent specifications (Table 1.2).

Table 1.2: Feature (or target) detection standards (after IHO special publication S-44, 2008)

| | Survey Order | | | |
|---|--------------|---|--------------|--------------|
| | Special | 1a | 1b | 2 |
| Minimum size of features to be detected | 1-meter cube | 2-meter cube up to 40 m depth; 10% of depth beyond 40 m | Not required | Not required |

Previous experiments have shown that IHO-level multibeam target detection in shallow waters is successfully achieved until approximately 60° incidence angle in some modern MBES (Hughes Clarke *et al.*, 2013). Beyond that point, detection capability

typically degrades. Many factors, individually or in combination, are responsible for this difficulty. The bottom-projected beam footprint, which is dependent on the beamwidth, depth, and grazing angle, is one of the major controls on the spatial resolution and therefore affects the system's ability to resolve small targets. In flat seafloors, the greater the beamwidth, depth, and incidence angle, the larger the projected beam footprint. Targets at the size of or smaller than the beam footprint may not be adequately resolved (Hughes Clarke, 1998).

Other factors that limit outer swath detection include the widening effect of beams steered away from broadside to the receiver, which augments the loss in spatial resolution. The across- and along-track sounding densities derived from the beam spacing and the combination of vessel speed, ping rate, and yaw stabilization capability, respectively, also restrain the feature detection capacity.

In addition to geometric aspects, even when the system embodies the required range and angular resolution to resolve small targets out of 60° , limitations of the built-in bottom detection algorithms and filters applied by the manufacturer may cause target omission. The result is a data gap in the bathymetric surface and a shadow in the backscatter image (Fig. 1.2).

To cover more ground and therefore to reduce survey time, the Brazilian Navy (author's sponsor) has recently purchased some units of a contemporary dual-head MBES, manufacturer Kongsberg[®], model EM 2040D (D stands for dual), to be used in the well-mixed fresh and shallow waters of the Amazon River and Paraguay River basins. The dual-receiver version of the EM 2040 is particularly adapted to wide swaths, as the tilted receivers maintain narrower beams at wider incidence angles. Thus,

potentially, wider-swath angular sectors (greater than $\pm 60^\circ$) could be employed. Beyond that point, however, the target detection becomes the limiting factor.

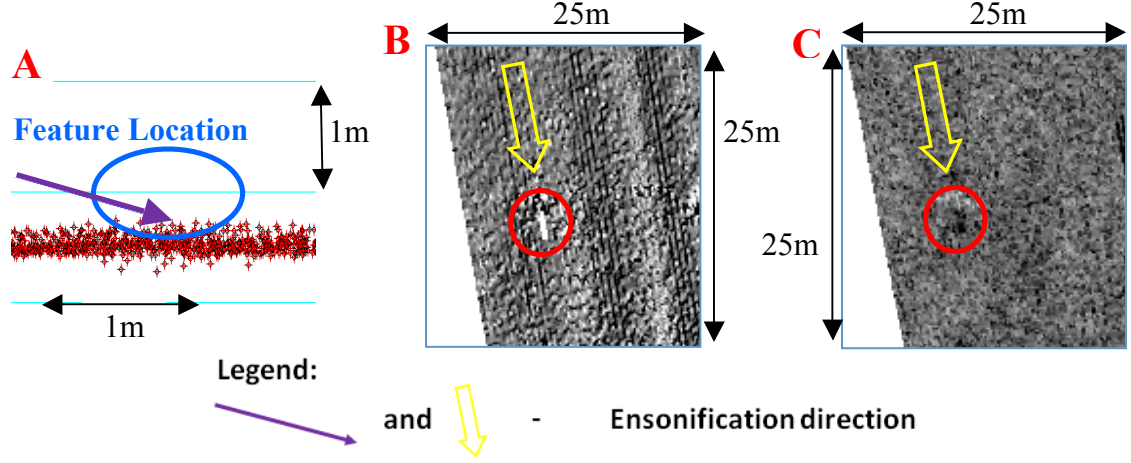


Figure 1.2: Example of an undetected 1-meter cube at low grazing angles in shallow waters (after Hughes Clarke *et al.*, 2013)

Across-track depth profile (A), bathymetric surface (B), and backscatter image (C) in the vicinity of a 1-meter cube imaged with 68° incidence angle using a MBES Kongsberg[®] EM 2040D at 20 m depth. Note that the object may not be considered detected. The combined analysis of the data gap in (B) and the shadow in (C) (red circles) at the same location is a possible, yet not necessarily sufficient, indication of the object presence

Motivated by the EM 2040D acquisition, this research worked on that issue of unreliable target detection at low grazing angles that affects some Kongsberg[®] MBES (Fig. 1.2). The project focused on developing an enriched nonconventional bottom detection algorithm based on the Bearing Direction Indicator (BDI) method. Unlike conventional methods, the developed BDI-based algorithm is capable of successfully providing positive bathymetric solutions over a target at very low grazing angles, which certainly contributes to a better object discrimination within the surrounding area. This, ultimately, leads to an improvement in the target detection and definition capability.

1.2 Research Questions

To what extent can the detection/definition of low-grazing-angle IHO-compliant targets in shallow waters be improved by applying an alternate bottom detection method based on the BDI approach? Does BDI always detect a target when conventional methods do not? How reliable would the BDI method be compared to conventional methods?

1.3 Research Objectives

This research has three objectives:

- (1) Develop a BDI-based bottom detection algorithm.
- (2) Test the algorithm using appropriate datasets.
- (3) Assess its capability of detecting IHO-compliant targets at very low grazing angles in shallow waters.

1.4 Thesis Structure

This thesis is structured in five chapters. The current chapter introduces the problem being studied and the approach used to potentially minimize it. Research questions and objectives are also discussed here. Chapter 2 provides a review of some essential concepts related to this research. The main specifications and characteristics of the EM 2040D are presented as well. In addition, discussion and critical analysis of previous works are provided. Chapter 3 presents the methodology used in this research, and the details and constraints of the developed algorithm. Performed tests, achieved

results, and analyses are discussed in chapter 4. Chapter 5 states the conclusions, future works, and contribution of this work to the field of hydrography.

2. Background

2.1 Bottom Detection Methods

2.1.1 Overview

After a pulse is transmitted and until the next one is released, MBES receivers record any acoustic energy within their bandwidth coming from all directions within the resultant transmitter-receiver beam pattern of all beams. For each beam, the signals are recorded with a certain duration that reflects the achievable range resolution of the pulse in discrete and uniformly separated time intervals. The cumulative time corresponds to the amount of time that the transmitted sound wave travels from the transmitter to a reflector and then back to the receiver. This is called echo time of arrival (TOA) (Fig. 2.1). Essentially, the TOA represents the two-way travel time (TWTT) of the sound wave reflected back.

All incoming acoustic energy perceived by a specific beam is stored as if it were coming from the center of the beam (boresite), even though, in reality, it is coming from all sensitive directions of the resultant transmitter-receiver beam pattern. The apparent direction from where the echo is received is called echo direction of arrival (DOA) (Fig. 2.1). Mixed with the echoes or apart from them, environmental noise is perceived and recorded as well.

Fundamentally, for the purpose of navigation, the most important MBES output in which users are interested is the bottom location, which allows them to see the ground relief and any submerged object that may cause safety concerns. Calculation of bottom location is based on the proper identification of the water-seafloor or water-object interface. This is accomplished by comparing the strong echoes reflected back by those

Bearing Direction Indicator (BDI), and phase detection (both zero-phase and high definition).

2.1.2 Weighted Mean Time (WMT)

WMT computation is based on the intensity time series recorded within a single receiver beam channel (de Moustier, 1993). Given the echo DOA implicitly assumed to be the maximum response axis of the steered beam, the TOA is calculated. The goal of WMT is to determine the instant when the boresite of the transmitter beam hits the bottom.

In MBES oblique incidences, considering a flat seabed, a sound wave front first touches the bottom in the inboard edge of the physical beam, continues to interact with the seafloor within the beamwidth, and eventually ends its interaction by passing through the outboard edge of the physical beam. The resultant echo envelope reflects the modulation imposed by the within-beam spatial variations in seabed backscatter strength to the receiver beam pattern in elevation (Fig. 2.2).

Due to that modulation, the boresite instant is very hard to determine accurately. Essentially, it depends on both the receiver beam pattern in elevation and the seafloor within-beam relief and composition. It is reasonable to conclude that that moment is neither necessarily the echo envelope mean time nor the echo envelope maximum amplitude time. In practice, the most common approach to calculate center-beam instant is to consider it as being the center of mass of the echo envelope (weighted mean time) over a defined threshold. Thus, a DOA/TOA couple is determined: the first element is the angle of the center of the beam, and the second one is the center of mass of the echo

envelope. WMT, therefore, is just an approximation of real boresite instant, and the method by itself provides one solution per beam.

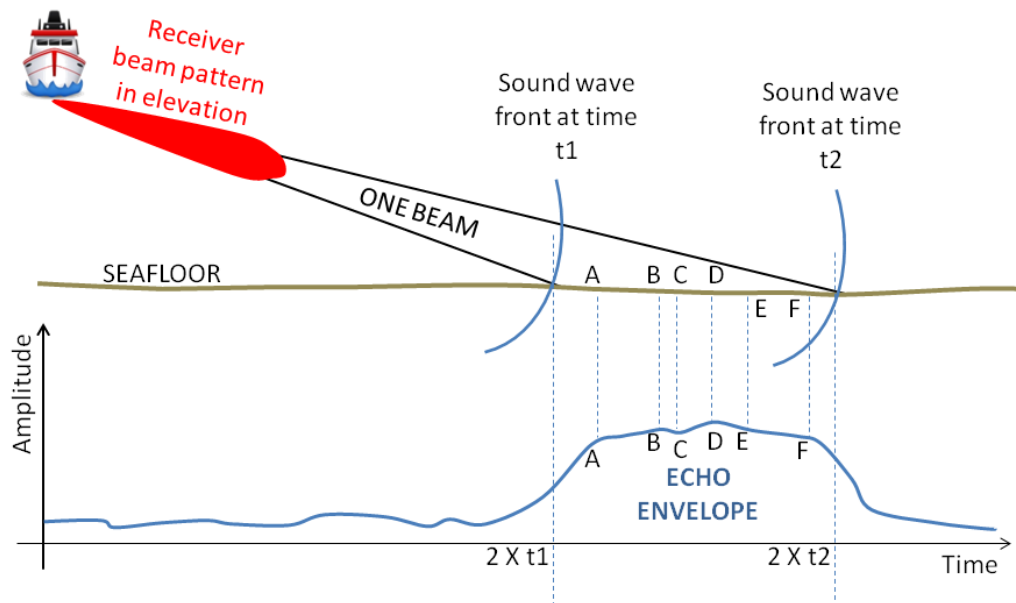


Figure 2.2: Within-beam sound wave interaction with seafloor

WMT accuracy strongly depends on the echo envelope width. For low incidence angles, WMT yields more accurate results, as echo envelopes are shorter under these conditions. On the other hand, for high incidence angles or low grazing angles, the WMT method of determining the center-beam instant produces more inaccurate solutions as echo envelopes become wider. Consequently, uncertainties of the boresite instant become greater. For a flat seafloor, WMT accuracy decays with increase in incidence angle.

2.1.3 Bearing Direction Indicator (BDI)

The second bottom detection method, BDI, is based on the angle series at a specific TWTT (time slice). BDI is an inverse approach to WMT. Given the echo TOA, DOA(s) is(are) calculated (Satriano *et al.*, 1991; de Moustier, 1993). The goal is to determine the direction(s) from where acoustic intensity is maximum, which represent locations on the seabed being ensonified at the TWTT considered (Fig. 2.3). BDI calculation provides one or more angle solutions per time slice.

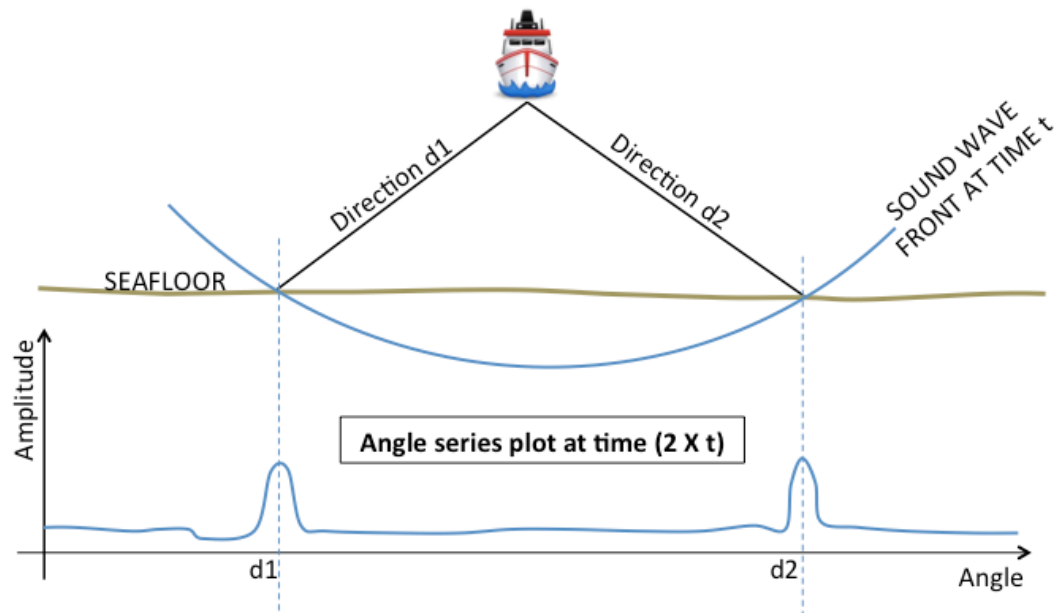


Figure 2.3: BDI bottom detection method: determining maximal amplitude directions, given the sound wave two-way travel time

One of the limitations of MBES that impact BDI accuracy is the number of channels recording echo directions (or the number of physical beams) and their angular spacing. When a sound wave strikes a point scatterer on the seabed, the returned energy is sensed and recorded by many surrounding beams as a function of the angular

separation between the scatterer's elevation angle and the main lobe (or side lobe) maximum response axis of the beam considered.

If an echo direction is inside a beam's main lobe angular sector, the smaller that angular separation, the greater the stored echo amplitude. The same concept applies to the side lobes. The closest beam to the scatterer registers the strongest magnitude, followed by its close neighbors, and so on. Other distant beams may, or may not, sense that returned energy, depending on whether the scatterer's elevation angle is within their main lobe (or any side lobe) angular sector or is exactly at a null direction, respectively (Fig. 2.4).

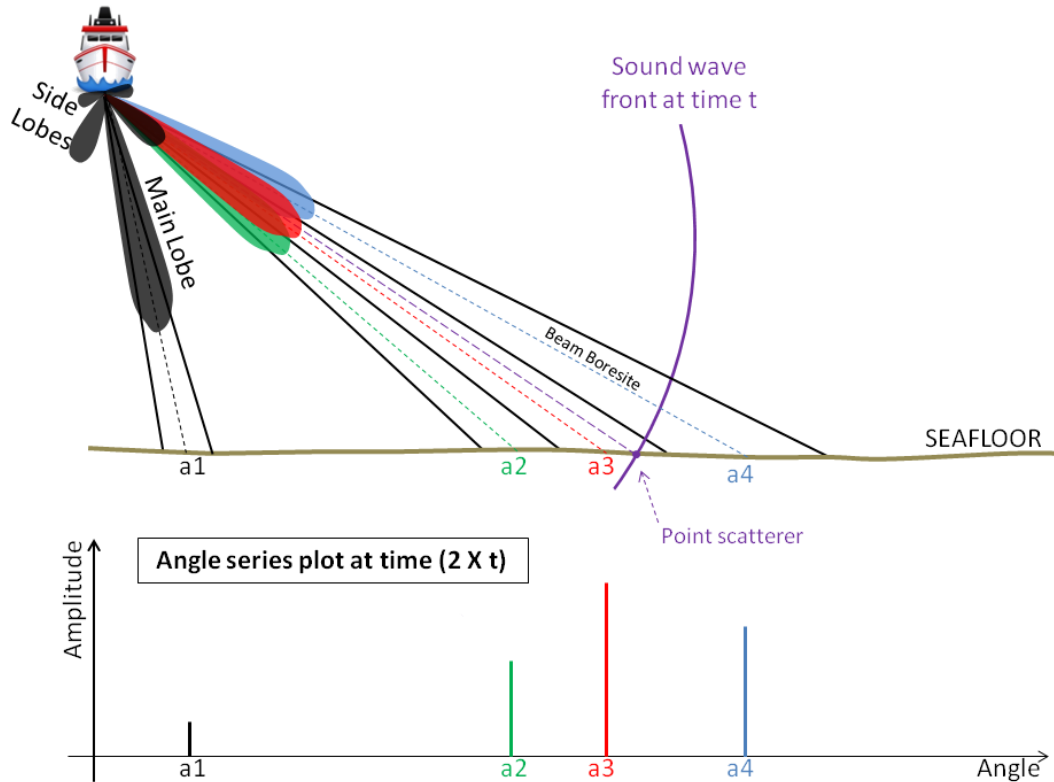


Figure 2.4: The influence of the beam pattern over the record of echo amplitudes as a result of the sound wave being reflected back by a point scatterer (four beams example)

For simplification reasons, side lobes of beams represented in green, red, and blue were not drawn

Therefore, the maximal recorded amplitude is not necessarily the actual maximum echo amplitude of the water-seafloor interface at the TWTT considered, except if the scatterer's elevation angle coincides with a particular beam's main lobe maximum response axis (boresite). Thus, taking the beam axis angle with the maximum amplitude in a particular time slice as the BDI angle solution does not convey a sufficiently accurate result. A better angular discrimination is needed. As part of this research, a refined BDI DOA calculation is presented in chapter 3. Notably, unlike WMT, the variability in seabed backscatter strength across-track has no effect, as all intensities share the same TWTT (the exact same seabed).

The angle of incidence of the transmitter beam onto the seabed also influences the BDI accuracy. Where a sound wave front can be considered almost parallel to the bottom (close-to-normal incidence), a wide area of the seafloor is ensonified nearly instantaneously (broader bottom-projected pulse length). Therefore, echo amplitudes of surrounding beams will have very similar values within that broad angular sector (considering uniform seabed backscatter strength). This situation creates a wide and flattened angle envelope on the angle series plot. Thus, the definition of the maximal amplitude direction (BDI angle solution) can result in a misleading or inaccurate value, especially if a long pulse is used.

Alternately, for oblique incidences, the bottom-projected pulse length becomes narrower, and only a few beams (the closest one and its very close neighbors that lie within its main-lobe width) mark strong echo amplitudes. This makes the angle envelope of the angle series plot thinner. In this case, lower uncertainty is obtained when calculating the maximum amplitude direction. Figure 2.5 illustrates the two discussed

concepts. For a flat seafloor, therefore, the BDI accuracy increases with the increase of the incidence angle, contrary to the behavior of WMT. Due to this characteristic, BDI can be considered an alternate to WMT for low-grazing-angle incidence.

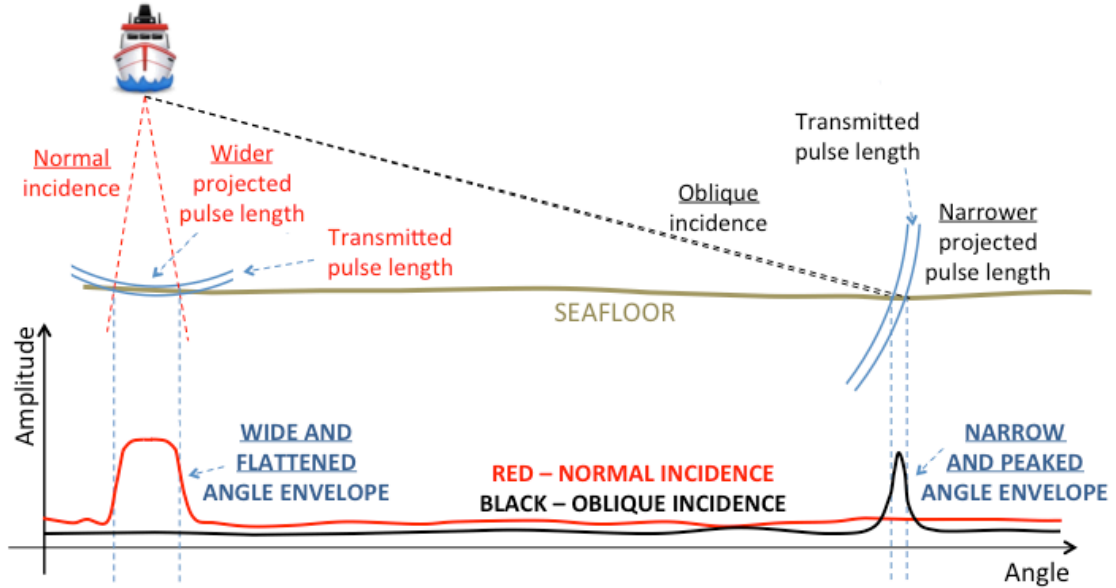


Figure 2.5: BDI accuracy and its dependence on incidence angle

The wide and flattened angle envelope of close-to-normal incidence provides greater uncertainties for the BDI angle solution, in contrast with the narrow and peaked envelope of the oblique incidence

Rarely used today, BDI was introduced by the former company L-3 Communications SeaBeam® Instruments (2000). The method is first recorded in the literature back in the 90s (Satriano *et al.*, 1991). The very first MBES in the market were produced by SeaBeam®. They employed WMT and BDI jointly in their equipment. With the evolution of the technology, manufacturers began replacing BDI by phase detection. The sonar array sounding system on board the British Navy ship “Scott” may be the last remaining operational system using BDI. As discussed in the next section (2.1.4), the

phase detection technique provides more accurate solutions than BDI for most geometries, although it has some weaknesses.

2.1.4 Phase Detection

The third bottom detection method is called phase detection (Hammerstad *et al.*, 1991). Similarly to WMT, phase detection calculates the TOA, given the DOA. The calculation is based on the echo phase difference between two overlapping and offset virtual arrays of transducer elements arranged perpendicularly to the beam axis (Fig. 2.6). For each time sample within a beam, an echo phase difference computation is performed. When the value is zero, the signal is assumed to be coming from the beam axis, and this moment is recorded as being the TOA. Zero-crossing phase detection yields one solution per beam as well as WMT.

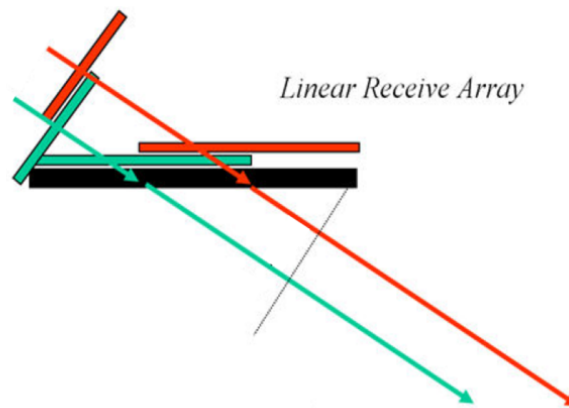


Figure 2.6: Receiver split-aperture (after Hughes Clarke, 2013b)

In practice, zero-phase calculation is carried out using the phase difference's time series plot. For each beam, to constrain only the phase wrap of the bottom interaction, an initial maximum amplitude detection is performed.

Generally, phase difference curves near normal incidence are narrow in time, steep in shape, and have rapid and large variations. This complicates the zero-phase crossing identification. Under these circumstances, a WMT solution is more reliable and robust than phase detection. Conversely, for grazing incidence, phase curves are wide in time, gentle in shape, and have slower and more stable variations. In this case, the zero-phase crossing is more easily and precisely computed (Fig. 2.7), as long as the signal-to-noise ratio (SNR) is good enough. Phase detection, therefore, is only trustworthy at low grazing angles.

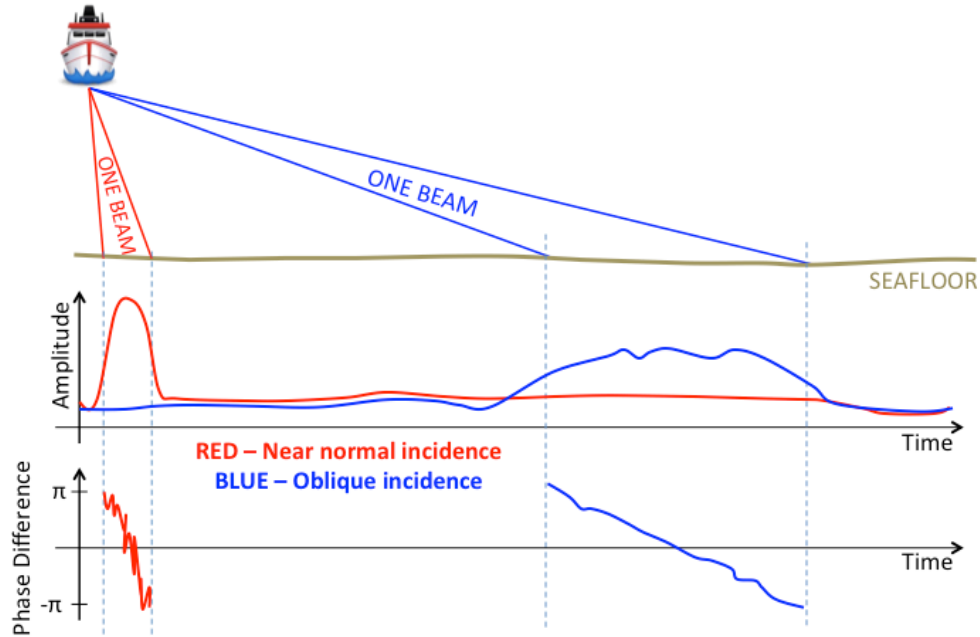


Figure 2.7: Illustrating the zero-phase crossing identification for normal (noisier) and oblique incidence

In contrast with WMT, phase detection is not affected by seafloor patchiness (Hughes Clarke, 1998). The within-beam seabed backscatter strength variations do not significantly influence the phase difference calculation. The only minor effect is that the

lower the SNR, the poorer the phase angle discrimination. This is, however, a random process, not a systematic bias. Thus, zero-phase crossing computation usually accurately determines the beam boresite bottom-striking time, irrespective of the within-beam seafloor patchiness.

The quality of phase detection is considerably limited by signal-to-noise ratio. Even with the more-defined phase ramp in oblique incidence, the zero-phase crossing is rarely determined using only one phase difference sample, except if sufficient SNR. Under poor signal-to-noise conditions, the estimate of the zero crossing requires a low-order polynomial regression through multiple samples (Fig. 2.8), which results in range smearing or across-track relief smoothing. To be considered a valid detection, however, the variance of the fitted curve must be below a certain threshold. If not, phase detection is aborted and an alternate method such as WMT provides the bottom solution.

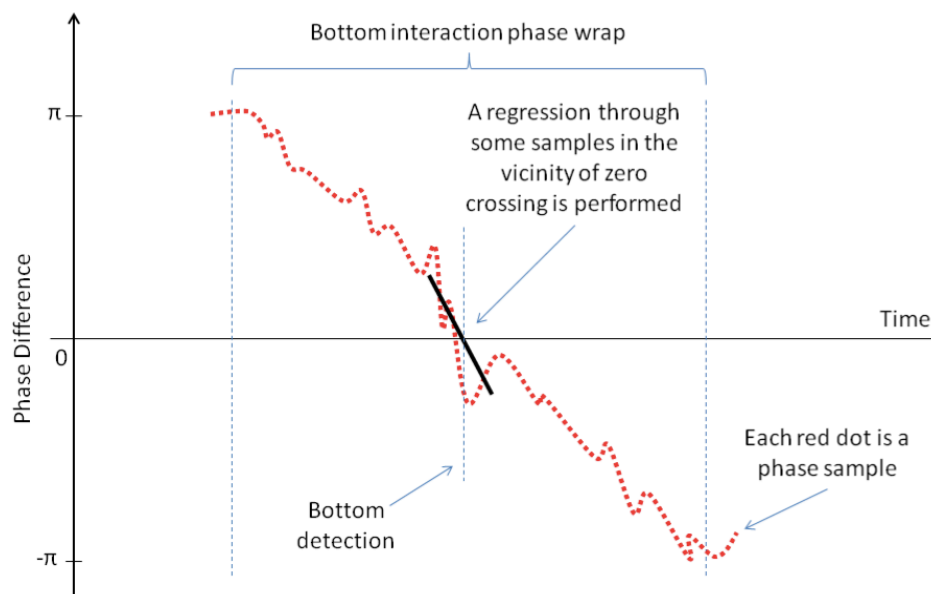


Figure 2.8: Example of a linear regression to estimate the zero-phase crossing

In the same manner as bathymetric sidescan sonars, the phase detection method is also affected by layover (or the common slant range problem). In this case, the layover problem is restricted to within a single receiver beamwidth (within-beam layover). Under near-specular incidence geometry, more than one physically distant point scatterer simultaneously reflects back the incoming energy. Their relative phases interact constructively and destructively, and a reliable phase estimate is not possible (de Moustier, 2009). The special case of a high-aspect-ratio target (such as a 1-meter cube) at a low grazing angle is an example where layover within a single beam can occur.

2.1.5 High Definition Beam Forming (HDBF)

By expanding the phase detection method to values of phase difference other than zero (Fig. 2.9, left-hand image), it is possible to obtain more than one depth solution per beam. For instance, phase differences of $-\pi/4$, $+\pi/4$, $-\pi/2$, $+\pi/2$, $-3\pi/4$, and $+3\pi/4$ are values commonly used. This broadened phase detection method is called high definition beam forming (HDBF) (Nilsen, 2012).

HDBF is extremely useful for the outer beams in a flat bottom and equiangular beam-spacing configuration. It allows the computation of more soundings within the larger footprints, significantly increasing the across-track sounding density (Fig. 2.9, right-hand image). The result is a gain in spatial resolution as well as an improvement in the within-beam topography definition.

Analogously to zero-crossing phase detection, HDBF viability and accuracy is dependent on good signal-to-noise conditions. HDBF also suffers from the same issue of incoherent solutions when facing within-beam layover. Range smearing due to the

application of linear or quadratic regression through several phase difference samples is of concern as well.

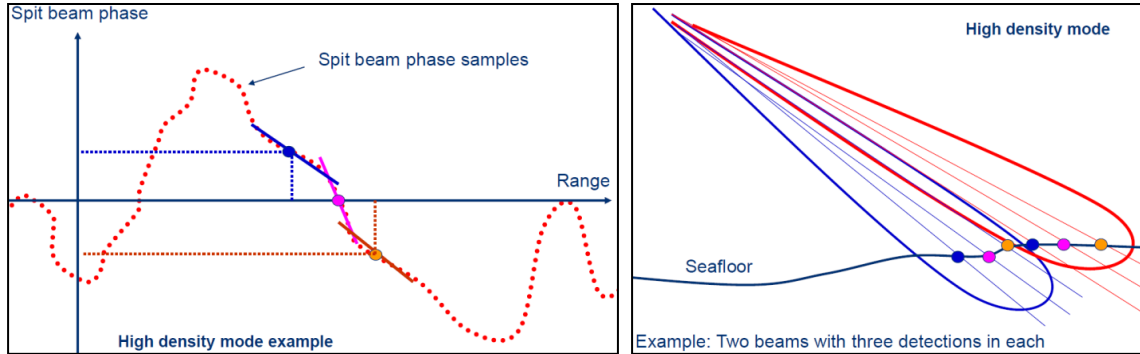


Figure 2.9: High definition beam forming (HDBF) (from Nilsen, 2012)

Concerning the three discussed bottom detection methods (assuming that zero-crossing and HDBF are both part of phase detection), it is worth mentioning that:

- (1) WMT is used predominantly for normal incidence by many manufacturers.
- (2) Phase detection is applied, generally, only for oblique incidence. Under this geometry, phase detection has been the preferred method by the majority of companies nowadays due to the higher accuracy (compared with BDI).
- (3) BDI is also applied primarily for oblique incidence. BDI “was used at a time for a minority of MBES and looks likely to be abandoned today” (Lurton, 2010).

In practice, the combination of WMT, phase detection, and BDI coherently employed yields the most reliable bottom detection solutions (de Moustier, 2009).

2.2 MBES Kongsberg® EM 2040D

The experimental component of this research was conducted using a MBES Kongsberg® EM 2040D (chapter 4). Data collected by this sonar was used to assess the capability of its built-in bottom detection algorithm to detect IHO-compliant targets at low grazing angles in shallow waters and also to test the algorithm developed for this research (chapter 3). For that reason, this section presents the main technical characteristics and specifications of the EM 2040D that are relevant to this thesis.

The EM 2040D is composed of three transducer arrays. One array is used only for transmitting. It is installed having its long axis aligned with the ship's head. The other arrays are receivers. They are installed in each side of the platform (Mills Cross arrangement, V-shape configuration) having their long axes perpendicular to the transmitter array and tilted (roll angle) between 35° and 40° (Fig. 2.10). Across-track distance between the two receiver arrays must be as small as possible. Internally, the transmitter array is subdivided into three line arrays, tilted -55° , 0° , and 55° . This allows pinging up to three sectors simultaneously. Angular coverage across-ship is up to 200° .

The dual receiver mounting is an additional option of the EM 2040 (without D) echo sounder. EM 2040 employs just one receiver array, which is usually mounted parallel to the sea surface (non-tilted). By physically tilting the two EM 2040D receiver arrays, the beamwidths at low grazing angles are steered less and thus are narrower. This gives the EM 2040D a better angular resolution at wider incidence angles.

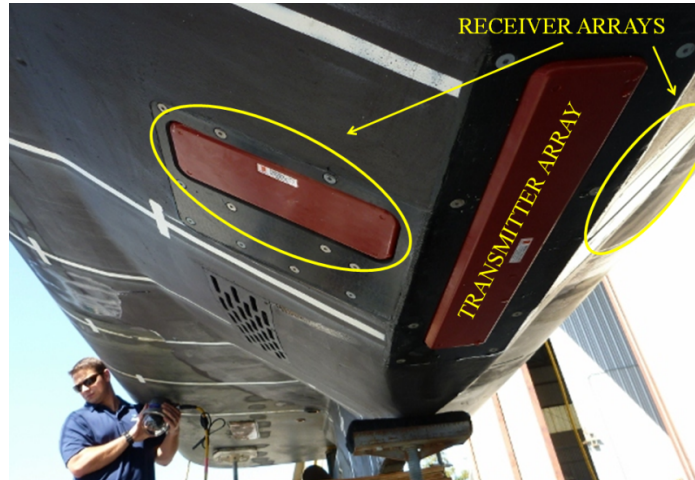


Figure 2.10: Example of an EM 2040D transducers installation (after Hughes Clarke *et al.*, 2013)

The EM 2040D main specifications are summarized in Table 2.1.

Table 2.1: EM 2040D main specifications

| | |
|------------------------------------|--|
| Number of Swaths | up to 2 |
| Number of Sectors | up to 3 (per swath) |
| Frequencies of Operation | 200 kHz, 300 kHz, or 400 kHz |
| Type of Stabilization | Roll, Pitch, and Yaw |
| Sounding Patterns | Equidistant, Equiangular, or High Density |
| Number of Physical Beams | 512 per swath (256 per receiver) |
| HDBF Capability | Yes. The spacing of the soundings is chosen so that equidistant sampling of the bottom is achieved |
| Number of Soundings in Normal Mode | One swath → up to 512 (256 per receiver) |
| | Dual swath → up to 1024 (512 per swath) |
| Number of Soundings in HDBF | One swath → up to 800 (400 per receiver) |
| | Dual swath → up to 1600 (800 per swath) |
| Bottom Detection Methods Employed | WMT and phase detection |
| Transmitter Array Models | EM 2040-04 (727 mm length) |
| | EM 2040-07 (407 mm length) |
| Beamwidth | 200 kHz mode: $0.75^\circ \times 1.50^\circ$ (EM 2040-04) or $1.50^\circ \times 1.50^\circ$ (EM 2040-07) |
| | 300 kHz mode: $0.50^\circ \times 1.00^\circ$ (EM 2040-04) or $1.00^\circ \times 1.00^\circ$ (EM 2040-07) |
| | 400 kHz mode: $0.40^\circ \times 0.75^\circ$ (EM 2040-04) or $0.75^\circ \times 0.75^\circ$ (EM 2040-07) |

In brief, the EM 2040D algorithm to detect the bottom proceeds as follows (Nilsen, 2012):

- (1) An initial WMT solution is calculated for all beams.
- (2) If the echo envelope is short, which indicates near-specular incidence, that WMT solution is used.
- (3) For the case of the echo envelope being long enough and having a minimum number of phase samples, a phase detection (either only zero-crossing or with HDBF) is employed. Phase solutions will only be accepted if residuals of the linear or quadratic regression are below a maximum value and the slope of the regression curve is between predefined limits.

2.3 Discussion of Previous Works

Some authors recently addressed the issue of in-water object identification and tracking by exploring water column (WC) data. Van der Werf (2010) proposed a post-acquisition method to identify the peak of any mast-like object in-between surface and bottom, and then translate the correspondent WC sample to the geographic reference frame. Although his method is efficient and extremely useful for safety of navigation purposes where least depth determination is critical, only in-water high-aspect-ratio (fraction of height over width) target identification was addressed. In addition, the methodology is highly dependent on well-trained hydrographers.

Rubrio Videira Marques (2012) went beyond van der Werf and implemented an automatic mid-water target detection and tracking method, even though no seabed-located object identification technique had been approached as well. His method

involved picking a peak in intensity in all of time, elevation angle, and along-track, making use of predicted pulse length, and receiver and transmitter beamwidths. In this sense, the DOA picking is equivalent to BDI, although Marques had not interpolated the samples to estimate the “real” maximum acoustic direction (this estimation is presented in section 3.2 as part of the algorithm developed for this thesis).

In contrast to in-water targets, literature investigation reveals that shallow-water seabed target detection in the very outermost beams (beyond 60° incidence angle) has been poorly explored, to date. The issue of accuracy and resolution loss in the outer beams is well known by the hydrography community. However, very few works have addressed and explored those sometimes-disregarded data for seabed target detection purposes. Some of the reasons for this gap in the feature detection research area include the limited use of dual-head MBES and the lack of proper locations (with some known and measured seafloor objects) to gather and evaluate data. During hydrographic surveys, when time is not a critical factor, reducing MBES angular coverage and, consequently, line spacing has been frequently adopted as the solution to keep accuracy, resolution, and target detection capability within predefined standards.

In a research tailored specifically to investigate vertical accuracy and target detection capability in shallow waters, Hughes Clarke *et al.* (2013) showed that, for some Kongsberg® MBES, both bathymetric tracking and feature detection in compliance with the IHO Special Order standards are only reliable up to 60° incidence angle. In that study, the researchers analyzed data collected by the EM 2040D and EM 710 over a site with several artificial cubic targets of different sizes (Hughes Clarke, 2013a). At the lowest grazing angles, they demonstrated that phase detection, primary bottom detection

method applied by Kongsberg[®] Maritime (KM) under this geometry, is clearly corrupted around a target, resulting in loss of bottom tracking. Although the target-derived shadow is shown in most analyzed cases, that shadow by itself is not an unquestionable evidence of an object presence.

In fact, high-aspect-ratio targets (such as 1-meter cubes) when illuminated at low grazing angles may lead to a within-beam layover geometry (Fig. 2.11). Under this circumstance, the sound wave front hits the inboard face of the feature practically at normal incidence (the target-projected pulse length spreads out over a wide range of elevation angles). Those simultaneous echoes from the target and the seabed in front corrupt the phase calculation, because more than one scattering point comes into play. Subsequent to the disturbed echo, random phase in the shadow window further invalidates the phase. The resultant split-aperture phase difference might be a meaningless or a very misleading value (Fig. 2.11).

Therefore, the regression curve through some phase difference samples around any boresite-relative angle will be strongly biased by those “spikes,” resulting in a curve-derived large variance and/or an out-of-bounds slope. Thus, normally, the bottom detection is aborted (Hammerstad *et al.*, 1991; Nilsen, 2012). The outcome is a characteristic sounding data gap (Fig. 1.2B).

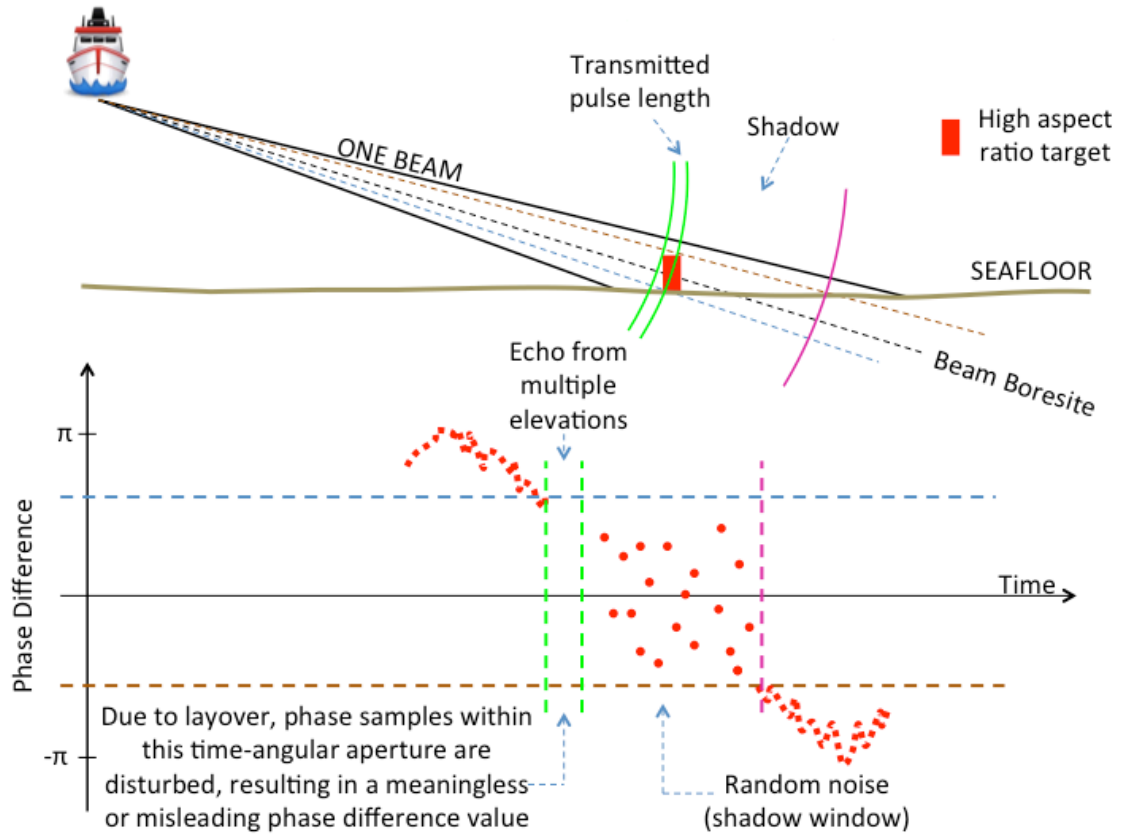


Figure 2.11: The within-beam common slant range (layover) phase disturbance

In the event of a rejected phase detection, if WMT is used as the alternate method, multiple beams around the target report the identical slant range resulting in a false arc of solutions (Fig. 2.12A). This happens because the relative level of the near-specular target strength, compared to the surrounding seabed, is often greater than the side lobe suppression. Bottom detection implementations by KM prior to 2010 (Fig. 2.12B) proved exactly that result over targets (Hughes Clarke, 2009). Subsequent tests on the same targets with a modified algorithm indicate that WMT solutions of similar slant range are now rejected, leaving just a hole (Hughes Clarke, 2010). Somehow the current KM bottom detection algorithm filters out those unrealistic depths. Consequently, no solution is provided. Only a characteristic data gap remains (Fig.

1.2B). Indeed, filters applied by manufacturers can omit a small target (van de Werf, 2010).

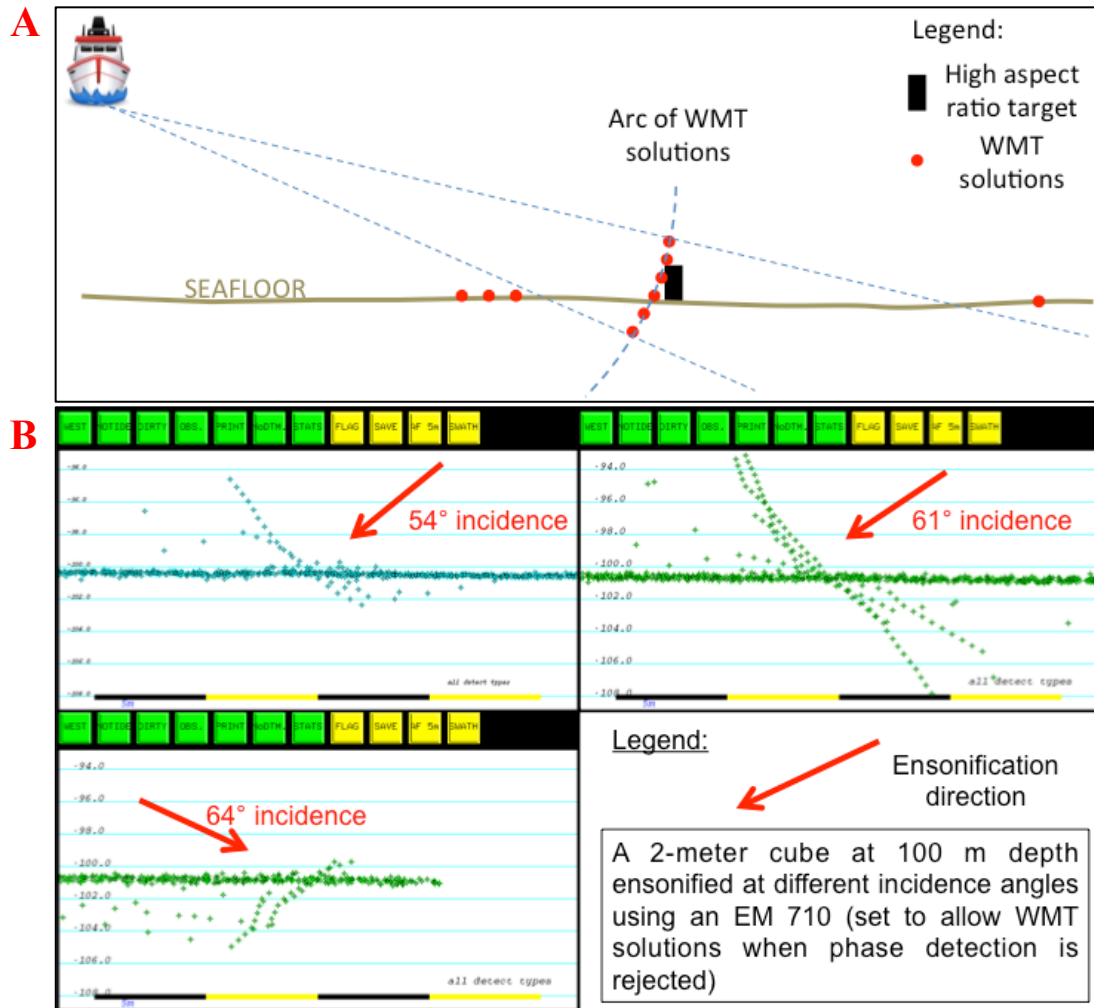


Figure 2.12: WMT arc of solutions when facing a high-aspect-ratio target (after Hughes Clarke, 2009)

While the current KM bottom detection algorithm might not identify an outer beam target, the logged water column imagery (WCI) can be used to recognize its presence (Fig. 2.13). The same arc of potential solutions that corrupts WMT is indicative of the target. If an alternate approach can be taken, then perhaps the target could be

recovered. WCI data have many applications and uses (Hughes Clarke, 2006). One of them is to calculate a new bottom pick.

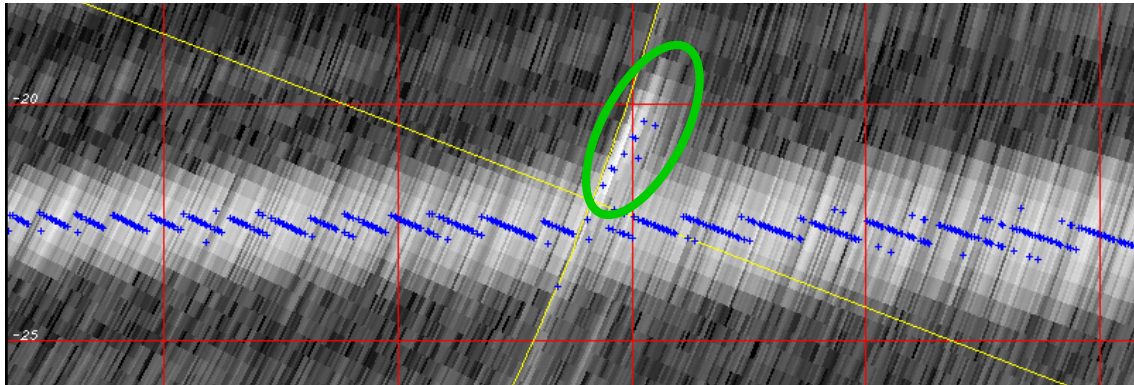


Figure 2.13: One-swath across-track WCI (section) highlighting the inboard edge (green circle) of the undetected 1-meter cube presented in Figure 1.2 (after Hughes Clarke *et al.*, 2013)

The small blue crosses represent, for each time slice, the strongest echoes (in the beam axis direction)

In the same 2013 study, Hughes Clarke *et al.* illustrated that the BDI method could provide such an alternate approach to the KM depth solutions as a way of improving high-aspect-ratio target detection/definition at low grazing angles. By their proposal, a composite WMT, phase detection, and BDI technique would be combined, thus corroborating de Moustier (2009).

Over recent years, for oblique incidence, phase detection has generally replaced BDI because finer angular discrimination was made possible (as a result of the application of a curve fitting through multiple samples only in the close vicinity of the boresite-relative intended angle), resulting in more accurate solutions. This, however, is strictly true only in the absence of high-aspect-ratio targets. This limitation becomes more acute at incidence angles beyond 60° . Under that geometry, the target

“appearance” in the WCI indicates that BDI is less affected by layover and poor signal-to-noise conditions than phase detection is. BDI may thus potentially be used as an alternate method to reveal any previously undetected abrupt seabed object at the very low grazing angles.

3. Methodology

3.1 Overview

To investigate and assess the potential BDI ability to improve multibeam shallow-water target detection/definition at low grazing angles, an enriched BDI bottom detection algorithm was developed. It runs within the Ocean Mapping Group (OMG) code. Calculations are performed based on the recorded WC data. The most relevant characteristics of the algorithm are:

- (1) The echo DOA refinement.
- (2) The option to compress the final depth solutions.
- (3) The possibility of selecting the detection threshold either manually (user-defined) or automatically.

The two last characteristics allow computing the BDI solutions in different manners.

Three softwares (subroutine packages) were created. The first one is called “bdi_funcs.c.” This software contains the functions that sweep all time slices, find the angle solution(s) over a defined threshold (each solution is a beam axis), and apply the calculation to refine the echo DOA. In addition, minimum slant range, filtering, automatic threshold, and compression are coded inside “bdi_funcs.c.”

The second subroutine package is termed “SE_BDI_DP.c.” This software is responsible for generating an additional customized widget to analyze the different possibilities of BDI solutions, extending the existing OMG Swathed WC Toolkit. The widget provides buttons, sliders, and graphics to allow the user to apply, visualize, and analyze the different modes of BDI. Essentially, the buttons and sliders call functions in “bdi_funcs.c.” Figure 3.1 presents an overview of the BDI widget. The BDI solutions

are plotted on the pie diagram of the already existing Swathed WC Toolkit, where a button to call the newly developed BDI widget (“SE_BDI_DP.c”) was created beforehand (Fig. 3.1).

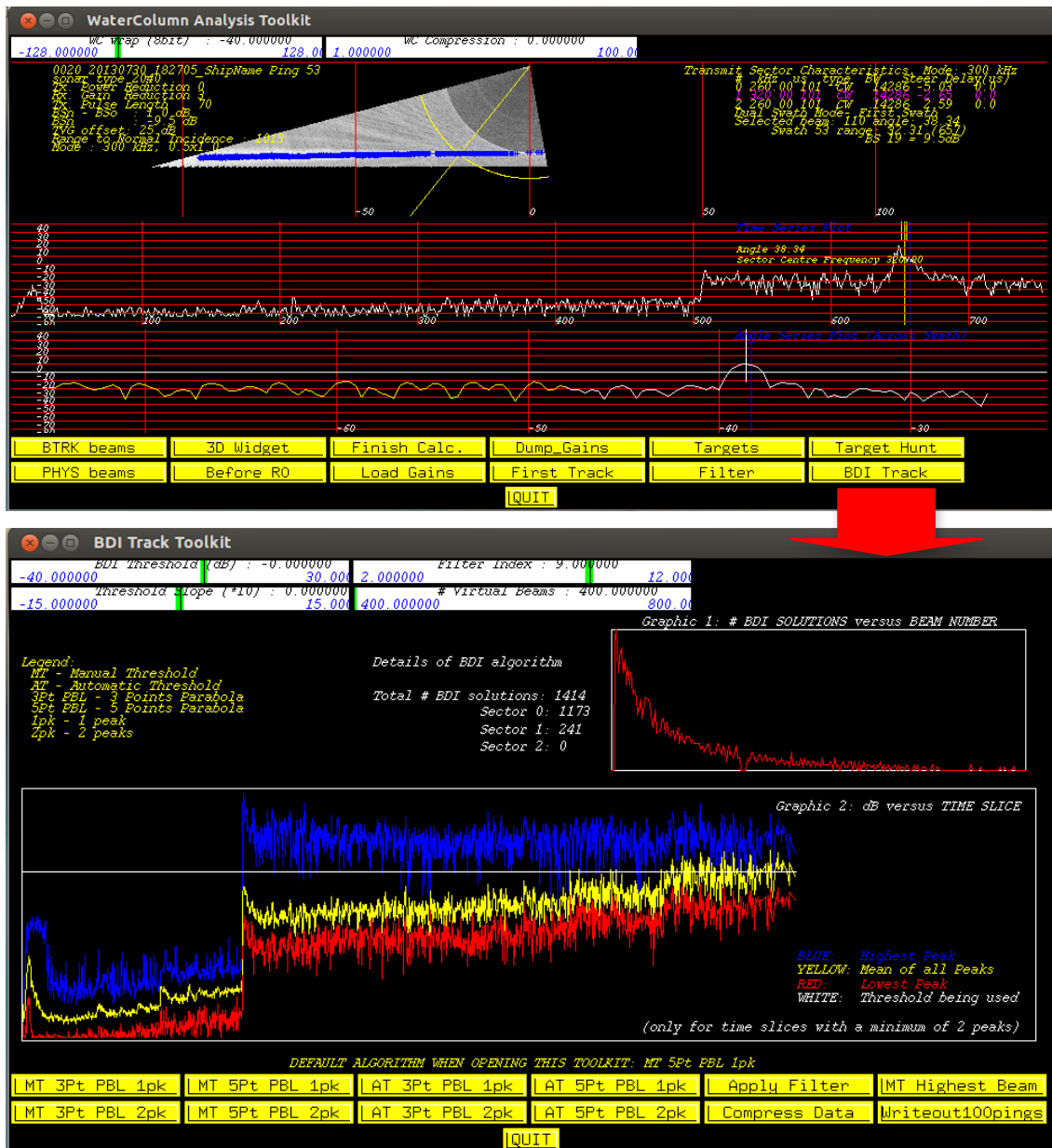


Figure 3.1: The preexisting OMG Swathed WC Toolkit (top) and the new BDI widget (bottom) The blue dots in the WC pie diagram represent the BDI solutions in the manner selected by the user through the buttons and sliders of the BDI widget. Graphics 1 and 2 of the BDI widget present data relative to the swath showed in the WC Toolkit

The third and last piece of software developed, called “applyBDI.c,” is a command line program. In the program, BDI solutions are computed for each swath of a chosen line of survey. The software allows for batch processing of large volumes of existing data. Computations are performed based on the parameters, defined by the user, input on the command line. These parameters include selection of either manual or automatic threshold, compressed data or not, and so on. In a similar way to “SE_BDI_DP.c,” the “applyBDI.c” program calls functions in “bdi_funcs.c”. The final output is a new merged file containing the calculated BDI solutions.

3.2 DOA Refinement

3.2.1 Overview

The task of determining TOA/DOA pairs by applying the BDI technique is, in principle, straightforward. Having the WC data, the algorithm just needs to sweep all time slices (TOAs) and, for each of them, find the beams (DOAs) with the highest amplitudes (over a predefined threshold) among their close neighbors. In practice, however, this approach results in solutions with angular discrimination no finer than the physical beam spacing (Fig. 3.2). This happens because, within a beam, all echoes are stored into the WC data as coming from the beam axis (not true, actually). This is referred to as the MBES angular discrimination limitation, which is defined thus by the number of beams and the sector over which they are spaced.

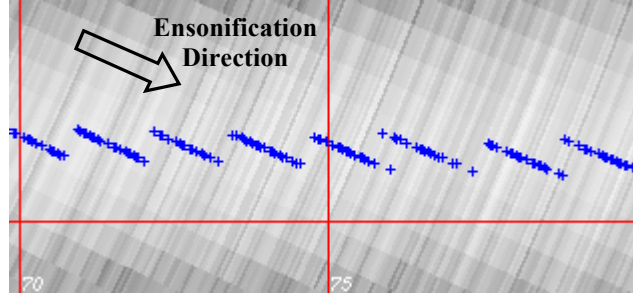


Figure 3.2: Preliminary BDI solutions based on choosing peak intensity, resulting in poor angular discrimination

To obtain an angular discrimination smaller than the beam spacing, a curve-fitting technique was applied around the representation of the receiver main-lobe beamwidth in the angle series plot. The receiver beam pattern in elevation was considered. By refining the DOA, more than one solution per beam with its own DOAs other than the beam axis can be computed. Under these circumstances, the outer beams will provide more BDI solutions, as their longer footprints accommodate more time samples. This results in an increased across-track sounding density and, potentially, a better short-wavelength object definition at low grazing angles.

Many surrounding beams, not only the closest, sense a specific seabed scattering target. Also, the receiver beam pattern in elevation is almost symmetric around its maximum response axis. Thus, in a hypothetical noise-free environment, when an echo is coming from a direction that coincides exactly with a beam axis at a particular time, the closest beam records the strongest magnitude and its adjacent neighbors a lower and equal amplitude (Fig. 3.3). This reasoning is true only if, at that particular time: (1) the transducer is receiving only that echo, (2) all beams have the same pattern, and (3) an equiangular beam-spacing configuration is being used. In the case of an incoming energy direction not coincident with a beam axis, prior and posterior beams store

different amplitudes. The closest neighbor beam reports the higher value (Fig. 3.4). The same concept applies to other close beams.

Hence, following the model of Satriano *et al.* (1991) and SeaBeam[®] (2000), it seems reasonable to fit a parabola passing through the highest amplitude beam and its close neighbors to estimate the echo direction (BDI angle solution) (Figs. 3.3 and 3.4). For that reason, parabola fitting was used in the BDI algorithm developed for this thesis as a way of refining the DOA, instead of considering it the closest beam axis. Based on the equation of the fitted parabola, $F(x) = ax^2 + bx + c$, the abscissa of the peak $\left(x_v = \frac{-b}{2a}\right)$ provides the estimation of the echo DOA. In the algorithm, there are two options for the parabola in terms of number of points, presumably associated with a detection, used in the fitting process:

- (1) **Three-point parabola.** Three points (angle-amplitude pairs) are considered: the highest intensity beam and its closest two adjacent beams (one in each side).
- (2) **Five-point parabola.** Five points are considered: the highest intensity beam and its closest four adjacent beams (two in each side).

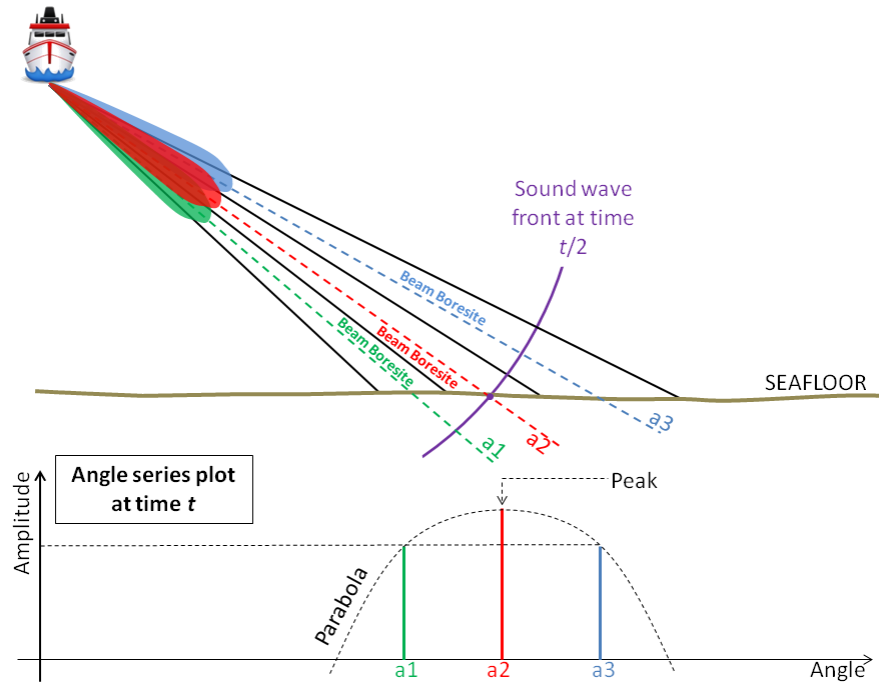


Figure 3.3: Angle series plot when echo direction coincides with a beam axis (three beams illustration)

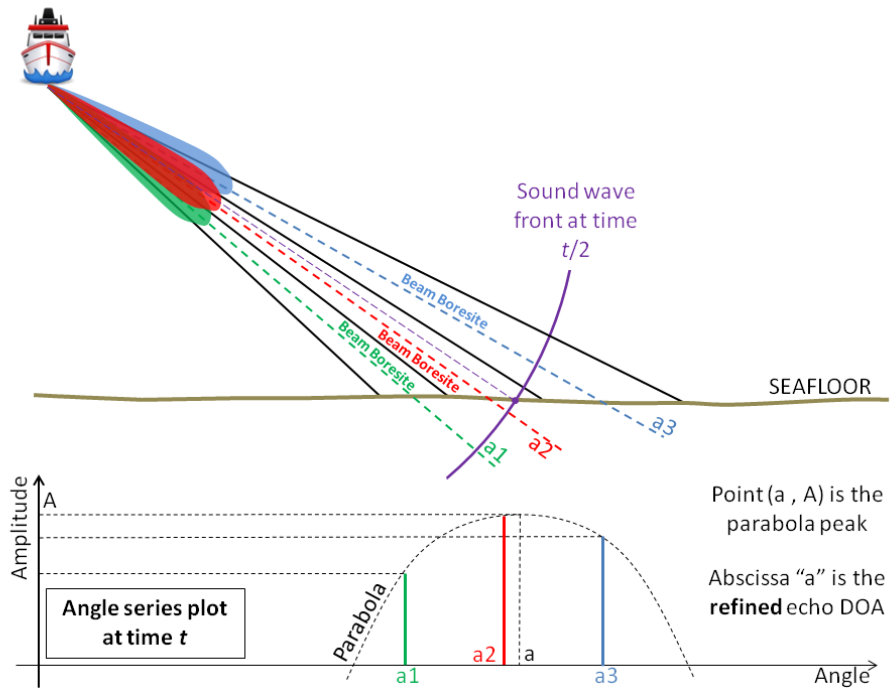


Figure 3.4: Angle series plot when echo direction is not coincident with a beam axis (three beams illustration)

Parabola fitting technique for the estimation of the maximal amplitude direction is fundamentally an attempt to model the receiver beam pattern in elevation. The term “estimation” is well suited because, in reality, due to the electronic beam steering process applied to flat transducers (case of EM 2040D) and its consequent beamwidth fattening effect with the increase of steering angle, each beam has its own pattern. Parabola fitting then is just an approximation, as even adjacent beams have slightly different patterns (the steering is slightly distinct).

In addition, noise and water column and sub-bottom backscatter strength variations across the entire angular coverage, at a particular time, interfere and mix with the bottom return signal recorded by the central and surrounding beams. This could bias the values for each discrete beam, resulting in an apparent offset DOA. Interestingly, even if noise is present, because all beams are sampled at the same instance, as long as the noise is not strongly directional, it will overprint on all beams similarly, thereby not significantly distorting the DOA.

The viability of parabola fitting is dependent on the receiver main-lobe beamwidth and the beam spacing. To make sense to use DOA parabola fitting as an attempt to model the shape of the receiver main-lobe beamwidth, a simple relation must be met. The beam spacing must be smaller than the effective receiver main-lobe beamwidth divided by the number of beams used in the fitting process (three or five). In other words, all beams (three or five) must be within the effective receiver main-lobe beamwidth.

For the case of the EM 2040D set to 300 kHz (configuration used in the datasets collected to test the developed algorithm), the nominal (-3 dB limit) receiver main-lobe

beamwidth at the beam perpendicular to the receiver array face (broadside) is equal to 1° . Away from broadside, however, the beamwidth grows with the secant of the steering angle. Regarding the -3 dB limit, note that it is just a convention. It means that the nominal receiver main-lobe beamwidth spans the angular sector between the points where the beam power is half of it in the maximum response axis. Nevertheless, the effective receiver main-lobe beamwidth is usually larger than the nominal value, typically three times more (Rubrio Videira Marques, 2012). It is defined by the main-lobe beamwidth measured above the background noise level. The greater the noise, the narrower the effective receiver main-lobe beamwidth.

For the worst case of an EM 2040D swath spanning from -10° to 80° (90° in total), the 256 physical beams in equiangular configuration (HDBF mode—configuration used in the experiments carried out in this thesis) result in a beam spacing of approximately 0.35° ($90^\circ \div 256$). Considering the effective receiver main-lobe beamwidth equal to 3° at broadside, the number of beams covered by it is at least eight ($3^\circ \div 0.35^\circ$), which is absolutely enough for the purposes of this research (three or five beams parabola fitting). Figure 3.5 presents an analysis with real data.

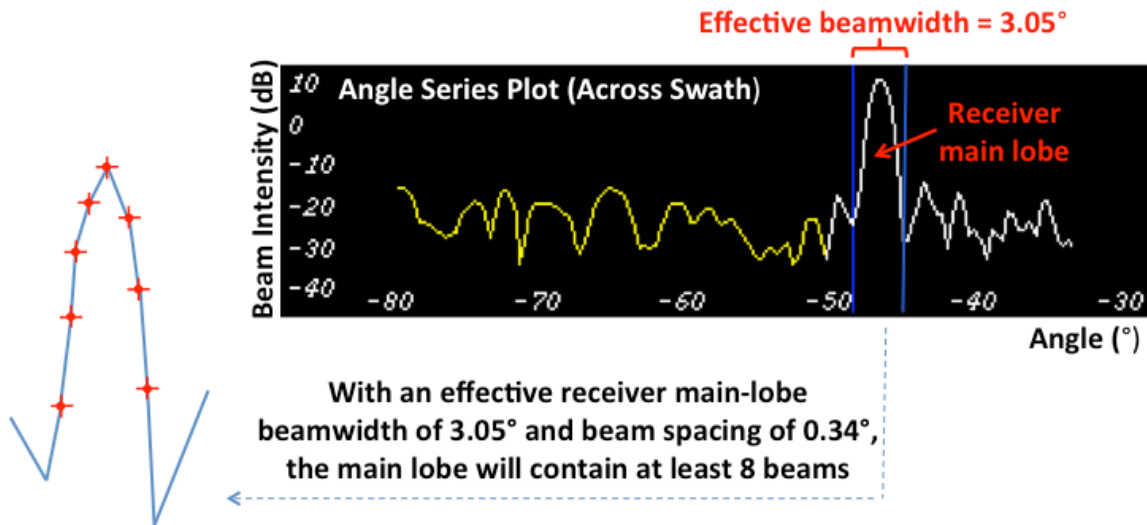


Figure 3.5: The effective receiver main-lobe beamwidth and its relationship with the maximum allowable beam spacing for the viability of BDI parabola fitting

In this EM 2040D example, the swath goes from -10.05° to 77.76° (87.81° in total). Assuming an effective receiver main-lobe beamwidth of 3° at broadside and a receiver mount angle of -35° , the effective receiver main-lobe beamwidth at the displayed incidence angle (-45°) is approximately 3.05° ($3^\circ \times \sec 10^\circ$ — 10° is the steering angle). As the beam spacing is 0.34° , the main lobe encloses at least eight beams ($3.05^\circ \div 0.34^\circ$). Thus, parabola fitting using three or five beams is viable

Additionally, note that the tighter the beam spacing, the more the number of samples within the effective receiver main-lobe beamwidth. Theoretically, the more the number of samples used in the parabola fitting with respect to the number of all samples within the physical beamwidth, the better the model. Thus, a five-point parabola is potentially a better approximation of the receiver main-lobe real shape if compared with the three-point approach, as long as the five samples are spaced within the main lobe and well above the noise. Also, the narrower the physical receiver beam, the more confident the angle solution and the less likely that layover within the beam will occur. To this end, for high incidence angles, the tilted receivers of the EM 2040D are significantly

superior to the horizontal single receiver of the EM 2040S, as their outer beams are steered less and consequently are narrower.

The accuracy of the BDI angle solution through parabola fitting also depends on how close the fitted parabola resembles the expected shape of the beamwidth. To provide a good estimation of the echo DOA, the width of the fitted parabola at the -3 dB level must be close enough to the expected nominal receiver main-lobe steered beamwidth (beamwidth at broadside multiplied by the secant of the steering angle). If they are not (usually the fitted parabola is wider), the calculated DOA may not be so accurate. In this case, at least one of these three situations may be present:

- (1) The pulse is hitting the seabed perpendicularly (e.g., around the nadir in a flat bottom).
- (2) The noise for the beams adjacent to the highest intensity beam is too high.
- (3) In the case of oblique incidence, a within-beam layover is occurring, which means the possible presence of a high-aspect-ratio target.

The following sections 3.2.2 and 3.2.3 present the mathematical techniques used to fit the three- and five-point parabolas, respectively.

3.2.2 Three-Point Parabola Fitting

The simplest theorem of polynomial interpolation (Davis, 1975) states that given $n + 1$ distinct (real or complex) points x_0, x_1, \dots, x_n and $n + 1$ (real or complex) values y_0, y_1, \dots, y_n , there exists a unique polynomial $p_n(x) \in P_n$ for which $p_n(x_i) = y_i$, where P_n represents the class of polynomials of degree $\leq n$ and $i = 0, 1, \dots, n$. Thus, given three distinct two-dimensional real points (x_1, y_1) , (x_2, y_2) , and (x_3, y_3) , a unique

parabola or straight line fits in them. Typically, a parabola is obtained. A first-degree or constant polynomial (horizontal straight line) only happens when the three sample points are geometrically aligned into the two-dimensional space. In this research, as the adjustment is always around a peak, the result is a concave parabola.

Derived interpolation polynomial (parabola or straight line equation given three distinct two-dimensional real points) can be computed in many different ways. A common approach is the Lagrange Formula (Davis, 1975), which for the case of three two-dimensional real points can be written as

$$L(x) = y_1L_1(x) + y_2L_2(x) + y_3L_3(x),$$

where

$L(x)$ is the interpolation polynomial,

$$L_1(x) = \frac{(x-x_2)(x-x_3)}{(x_1-x_2)(x_1-x_3)},$$

$$L_2(x) = \frac{(x-x_1)(x-x_3)}{(x_2-x_1)(x_2-x_3)}, \text{ and}$$

$$L_3(x) = \frac{(x-x_1)(x-x_2)}{(x_3-x_1)(x_3-x_2)}.$$

After a few developments, an equation in the form of $L(x) = ax^2 + bx + c$, where a, b , and c are constants (real numbers), is obtained. Based on water column data for each time slice, making

x_1 equal to the beam pointing angle immediately before the highest amplitude beam pointing angle,

x_2 equal to the highest amplitude beam pointing angle,

x_3 equal to the beam pointing angle immediately after the highest amplitude beam pointing angle, and

y_n equal to the amplitude of the sample x_n , where $n = 1, \dots, 3$,

the refined DOA (BDI angle solution) is straightforwardly obtained by calculating the fraction $\frac{-b}{2a}$ (abscissa of parabola peak).

The interpolated parabola given three points fits perfectly, and residuals of the adjustment are always zero. As an example, given the points $(75^\circ, 5 \text{ dB})$, $(76^\circ, 10 \text{ dB})$, and $(77^\circ, 6 \text{ dB})$, the resultant interpolated parabola equation using the Lagrange Formula is $L(x) = -\frac{9}{2}x^2 + \frac{1369}{2}x - 26020$, and the refined echo DOA approximately 76.0556° . Figure 3.6 shows this example graphically.

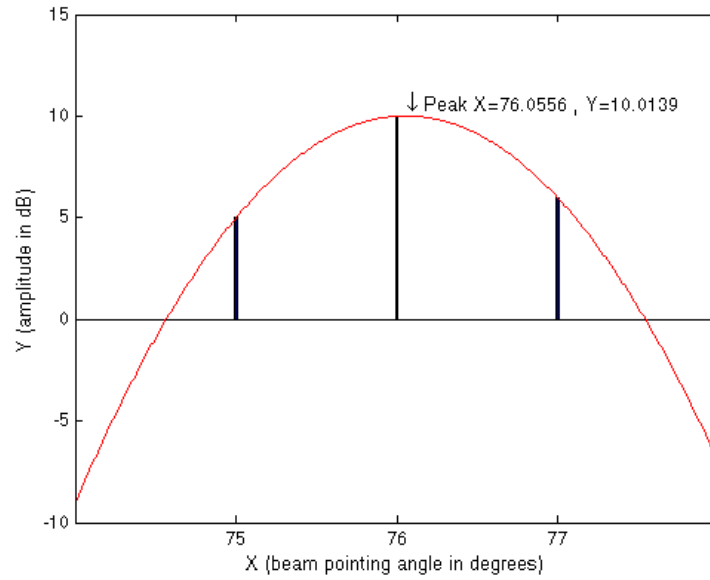


Figure 3.6: Example of three-point parabola fitting using the Lagrange Formula
Note that the fit is perfect and residuals are null

Figure 3.7 demonstrates how better three-point parabola BDI provides angular discrimination, compared with closest peak BDI.

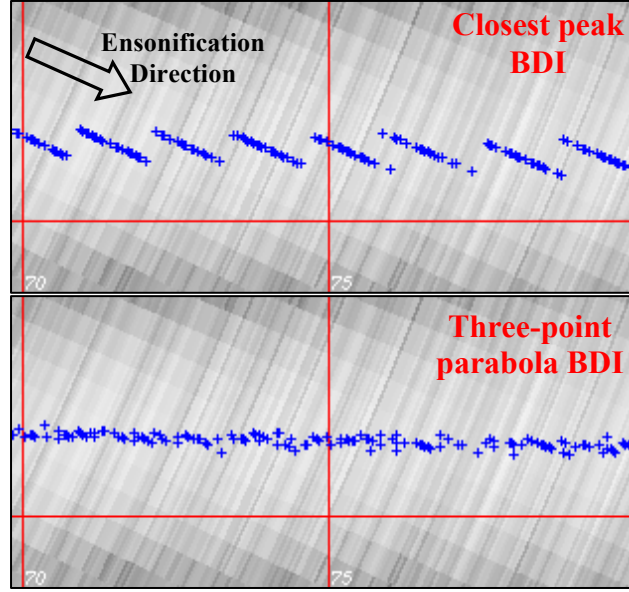


Figure 3.7: Closest peak \times three-point parabola BDI (same seafloor section)

Note that three-point parabola BDI provides smaller angular discrimination, compared with closest peak BDI (no parabola fitting)

3.2.3 Five-Point Parabola Fitting

Parabola fitting given five points leads to the resolution of an over-determined system of linear equations where the number of equations (five) overpasses the number of unknown variables (three). This system is inconsistent (no solution). Many methods exist to calculate an approximate solution. The method that minimizes the sum of the squares of the errors (residuals) in each equation of the system is called Least Squares Approximation, also known as regression.

Coefficients a, b , and c of the linear least squares parabola equation $F(x) = ax^2 + bx + c$ given the points (x_0, y_0) , (x_1, y_1) , (x_2, y_2) , (x_3, y_3) , and (x_4, y_4) , equally weighted, are computed by the expression (Davis, 1975)

$$\begin{bmatrix} a \\ b \\ c \end{bmatrix} = (XX^T)^{-1}XY,$$

where

$$X = \begin{bmatrix} x_0^2 & x_1^2 & x_2^2 & x_3^2 & x_4^2 \\ x_0 & x_1 & x_2 & x_3 & x_4 \\ 1 & 1 & 1 & 1 & 1 \end{bmatrix},$$

X^T is the transpose matrix of X , and

$$Y = \begin{bmatrix} y_0 \\ y_1 \\ y_2 \\ y_3 \\ y_4 \end{bmatrix}.$$

Similarly to the three-point parabola, making

x_0 equal to the beam pointing angle two positions before the highest amplitude beam pointing angle,

x_4 equal to the beam pointing angle two positions after the highest amplitude beam pointing angle,

y_0 equal to the amplitude of the sample x_0 ,

y_4 equal to the amplitude of the sample x_4 , and

$(x_1, y_1), (x_2, y_2), (x_3, y_3)$ as described in the previous section 3.2.2,

again the refined DOA is easily obtained by calculating the fraction $\frac{-b}{2a}$. As an example,

given the points $(74^\circ, 2 \text{ dB}), (75^\circ, 5 \text{ dB}), (76^\circ, 10 \text{ dB}), (77^\circ, 6 \text{ dB}),$ and $(78^\circ, 3 \text{ dB}),$ the

resultant parabola equation using Least Squares Approximation is $F(x) = -\frac{3}{2}x^2 +$

$\frac{2283}{10}x - \frac{43393}{5},$ and the refined echo DOA 76.1° . Figure 3.8 shows this example

graphically.

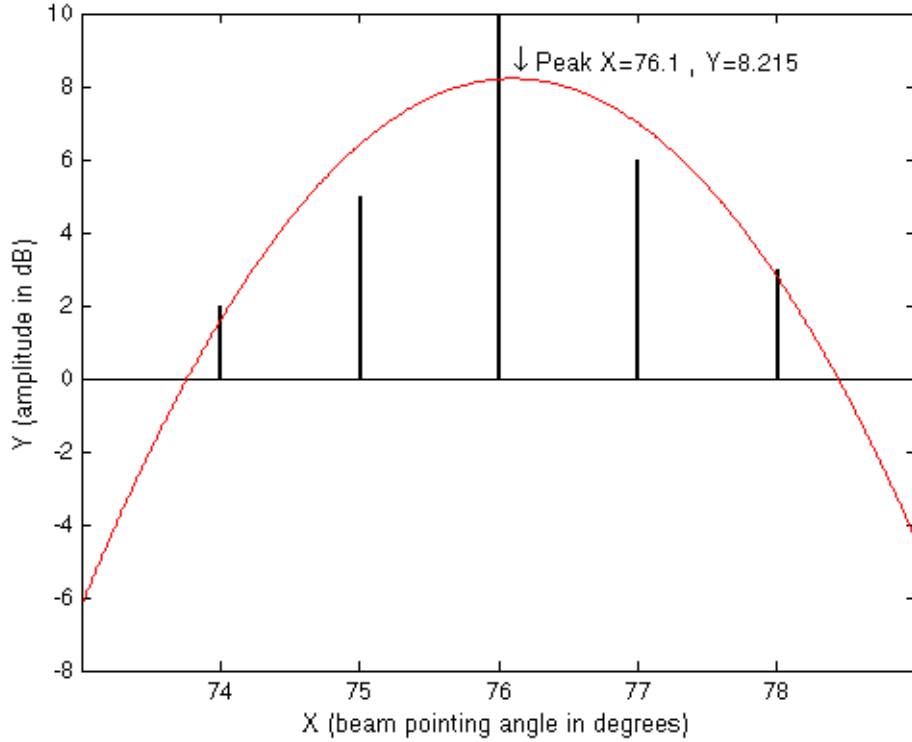


Figure 3.8: Example of five-point parabola fitting using Least Squares Approximation
Note that the fit is not perfect

Note that, as five-point parabola is not a perfect fit, the calculated maximum amplitude value (ordinate of parabola peak) may be smaller than the recorded highest amplitude (Fig. 3.8), which is not true in reality. Alternately, the five-point parabola maximum amplitude direction (abscissa of parabola peak) yields coherent results. When recorded amplitudes after the highest amplitude beam are higher than their corresponding beams on the other side (before the highest amplitude beam), the calculated maximum amplitude direction results in a value greater than the maximum amplitude beam pointing angle (case of Fig. 3.8). If the situation is the opposite, the resultant value is lower. As this research is not interested in estimating the “real” maximum amplitude value and solely in the direction associated with it, five-point parabola can be reasonably used to estimate the BDI angle solution.

Figure 3.9 shows the bottom solutions for the same seafloor section in three different ways: closest peak, three-, and five-point parabola BDI.

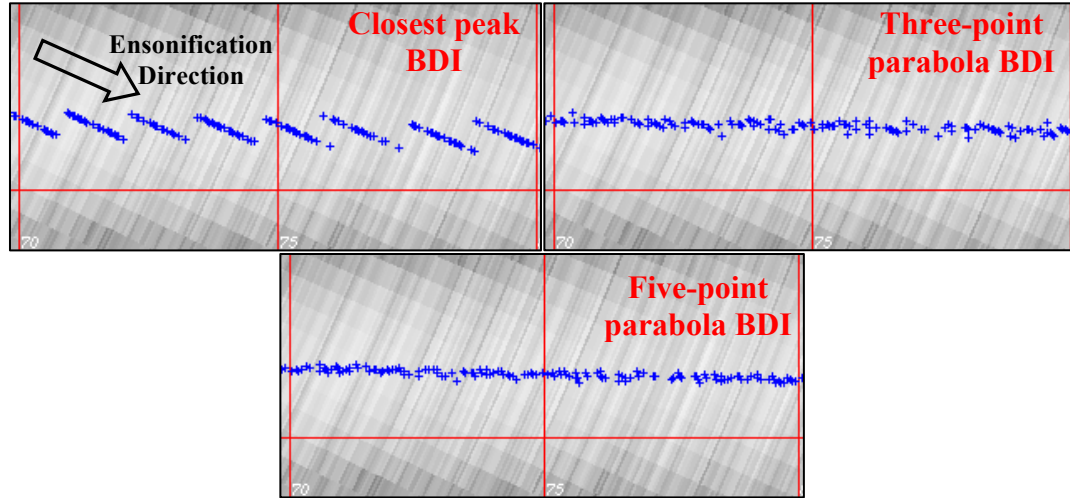


Figure 3.9: Closest peak × three-point × five-point parabola BDI (same seafloor section)

Note that five-point parabola BDI better discriminates the angle solutions, meaning, ultimately, a more representative shape of the actual seafloor topography. This happens because more samples within the physical beamwidth come into play, resulting in finer and more confident angle solutions

3.3 Number of BDI Solutions per TWTT

The number of BDI solutions per TWTT depends, essentially, on the seafloor topography and the receiver roll mounting angle. In a flat seafloor and non-tilted receiver configuration, the number of solutions is usually two, one for each side of the swath. If the receiver is tilted, the region closely around the nadir usually still has two solutions (Fig. 3.10A). Out of that region, only one solution is normally found (Fig. 3.10A). However, in an irregular seabed topography (Fig. 3.10B), the number of BDI solutions per time slice can be more than two for horizontal receivers (or one for tilted receivers).

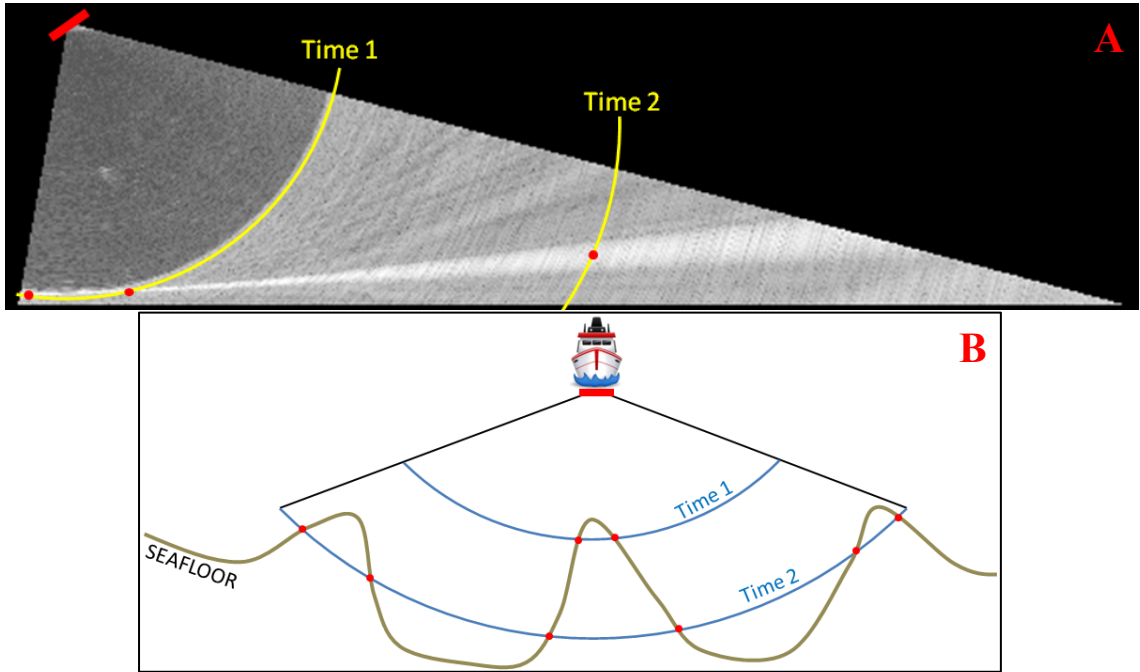


Figure 3.10: The variable number of BDI solutions per TWTT

For the purposes of this thesis, the developed algorithm was built to detect up to two BDI solutions per time slice, because the focus is the EM 2040D (generally one solution away from nadir). The first and second detections are always the first and second highest peaks above the threshold, respectively. To be considered a second detection, the second highest peak must be at least four beams apart from the first highest peak (Fig. 3.11). This requirement was implemented to allow fitting a five-point parabola for each peak. However, it implies a minimum height of target to get the base and the top simultaneously (for each elevation angle) (Fig. 3.12).

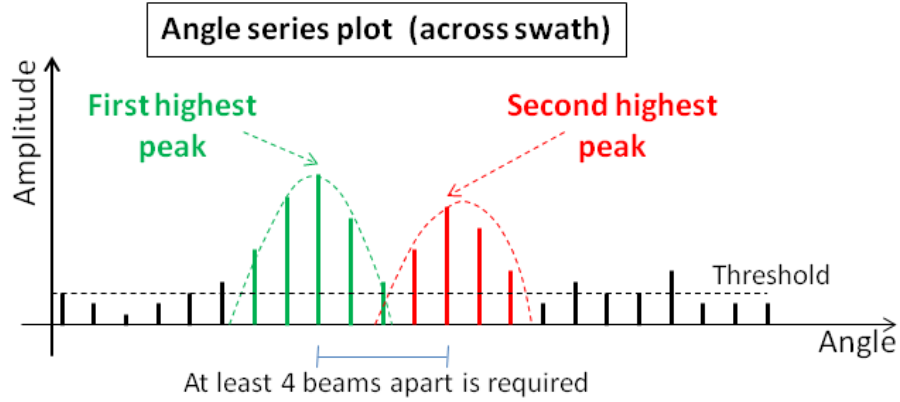


Figure 3.11: The maximum number of two BDI solutions per time slice in the developed algorithm

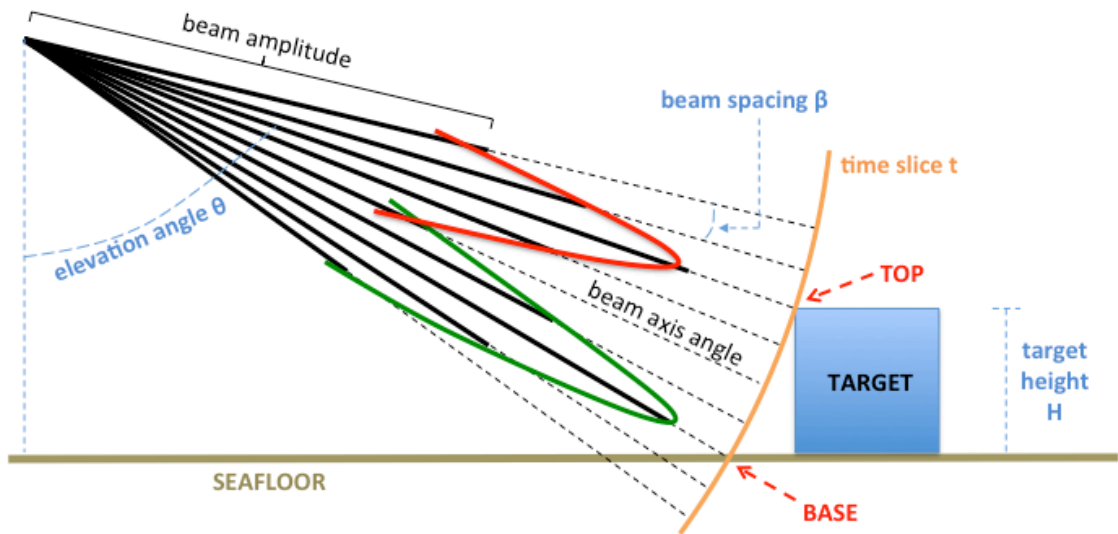


Figure 3.12: The minimum height of target (H) to get base and top at the same time, considering a maximum of two BDI solutions per time slice

At that particular elevation angle θ , when a maximum two BDI solutions per time slice is considered, it is only possible to detect, simultaneously, the base and the top for targets taller than H . This means at least four beams apart. For shorter targets, at the same elevation angle, less than four beams will separate the base and the top. In this case, even though two peaks might still be distinguished, only the strongest echo (either the base or the top—probably the top due to the near-specular incidence) will be retained because two distinct five-point parabolas are not possible. In the case of only one peak, certainly a layover is occurring. The final angle solution will be then somewhere between the base and the top

3.4 Detection Thresholding

While the echo of interest is at the intended DOA, at all angles for a given TWTT, there will always be spurious noise or side lobe echoes resulting in secondary peaks. To avoid mistakenly picking a false detection, a minimum cut-off intensity value (detection threshold) must be set. The detection threshold has to be somehow adjusted to a value greater than the background noise level and the peaks of the side lobes. The main outcomes of incorrect threshold setting are loss of real solutions and appearance of undesirable (and sometimes unavoidable) outliers. The BDI algorithm developed for this thesis has two options for the threshold setting:

- (1) Manually (user-defined).
- (2) Automatically.

Only peaks above the threshold are considered as potential detections. The manual approach was intended for development purposes to design an optimal operational automatic threshold.

3.4.1 Manual Thresholding

For the manual approach, the user chooses a threshold value based on the previous analysis of the peaks extracted from each time slice of the normalized WC data (with the time varying gain, TVG, implemented). The ideal threshold must clearly separate the peak echoes from the body. The chosen value is applied for all time slices within the selected swath. Figure 3.13 shows an example of an user-defined threshold applied for a particular EM 2040S swath.

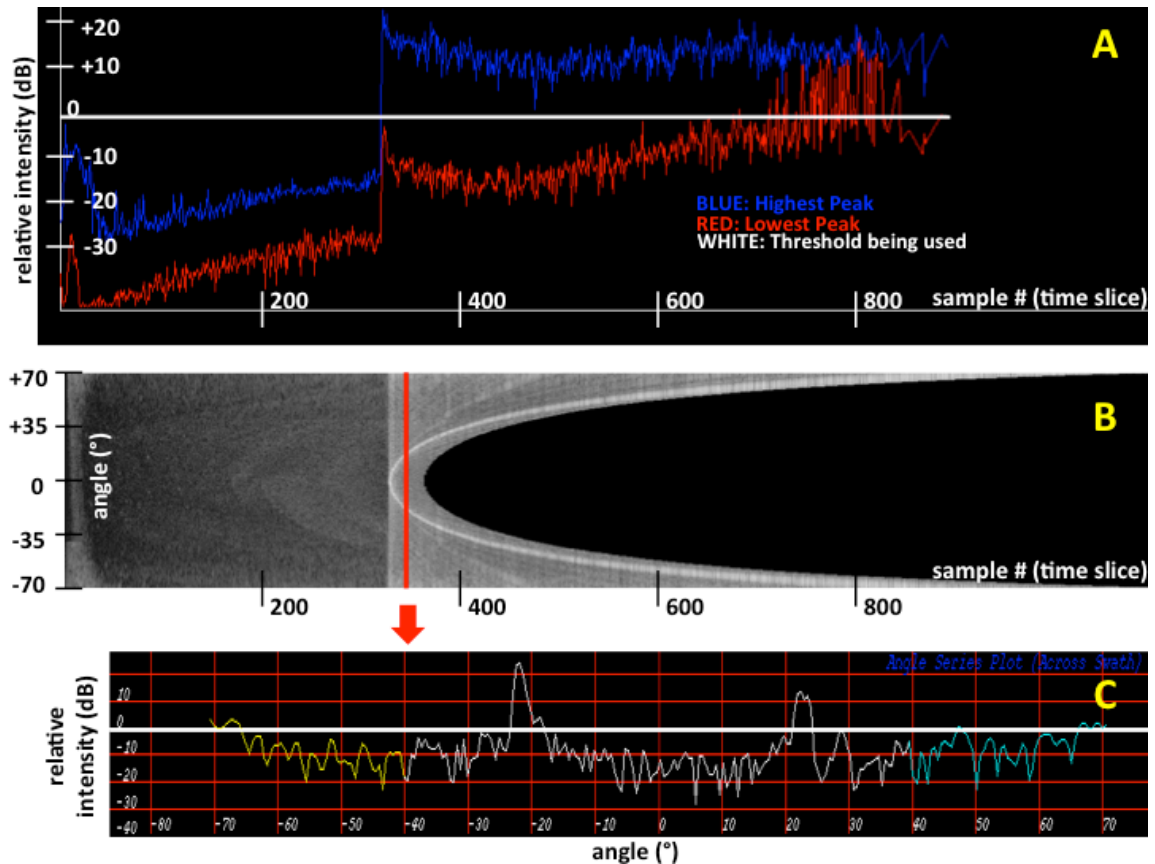


Figure 3.13: Example of an user-defined threshold for a particular EM 2040S swath

A – the blue and red lines represent the highest and lowest peaks, respectively, for each time slice of the recorded WC data for that particular swath in (B). The WC data has had a $30\log R$ TVG applied (R is the slant range). The white horizontal straight line at 0 dB represents the manually set threshold value. In this example, only peaks above 0 dB are solutions to be considered. B – the corresponding WC time-angle plot from which the highest and lowest peaks in (A) are extracted. C – the angle series plot (across swath) for the time slice highlighted in red in (B). Note that the two peaks approximately at -22° and $+23^\circ$ are the solutions to be considered in the BDI algorithm. They denote one detection (seafloor interaction) for each side of the swath

The aforementioned manual thresholding approach adopts the same threshold value for all time slices within the swath, assuming, therefore, that TVG echoes don't fade with range. This is not completely true. Essentially, the TVG tries to compensate the range-dependent signal losses due to the spherical spreading and attenuation, although it also makes the noise "rise", which is undesirable. On the other hand, the

TVG does not compensate the echo weakening as the incidence becomes grazing with range (considering a flat seafloor).

In addition to the instantaneous ensonified area (A), the backscatter strength level (BSL) that is part of the sonar equation also depends on the grazing angle. Besides, the BSL decreases with the reduction of the grazing angle. Thus, in a flat and non-variable sediment type seafloor, even though A increases with the increment of the incidence angle, the BSL as a whole reduces. The end result is a gradual and slight decay of the seabed echo intensities with range, even with application of the TVG. The challenge, then, is to have a threshold that stays above the TVG-gained noise while remaining below the BSL that is dropping with grazing angle. As can be seen in Fig. 3.13A, the two converge at the lowest grazing angles, especially when shadows start to be cast.

For that reason, an additional option for the user-defined thresholding was developed. It considers a unique threshold for each time slice within the swath. The value decreases linearly with range. In the algorithm, the threshold value entered by the user is assigned to the half-way maximum WC length. Around this point, the horizontal threshold line (Fig. 3.13A) is rotated clockwise (Fig. 3.14) in fixed steps of approximately 0.00175 dB/time sample.

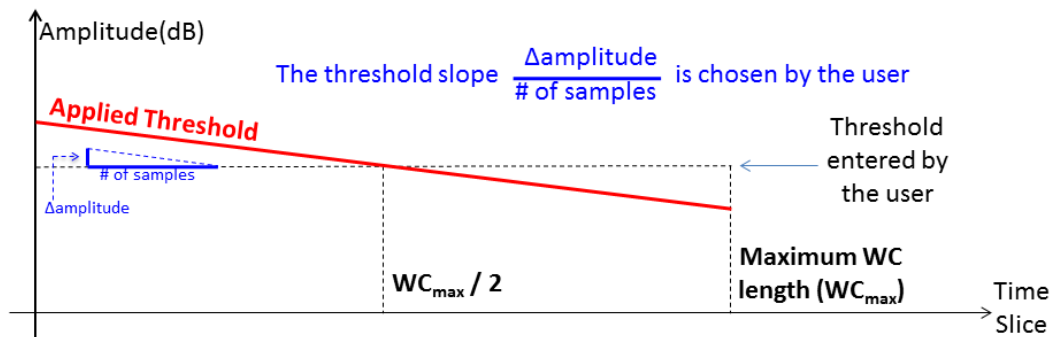


Figure 3.14: Within-swath linearly variable manual threshold

One relevant application of the within-swath linearly variable manual threshold is the possibility of potentially being able to increase the number of solutions in the outermost region of a swath without having to reduce the threshold entered by the user. This has the advantage of not having to cope with more solutions that a fixed threshold reduction may cause to the central beams (especially considering that this research focuses on the low-grazing-angle region), thus resulting in fewer calculations in the end and improved processing time responses. Figure 3.15 elucidates this concept. As can be seen, while this modification represents a slight improvement, ideally the threshold would be fully automatic and adjust for observed BSL and noise level.

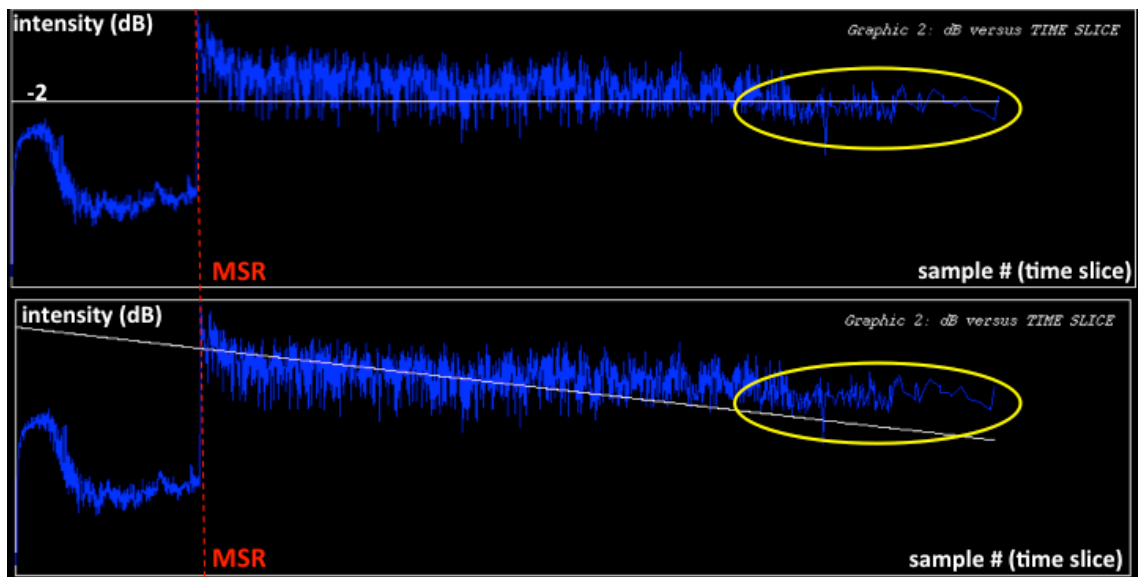


Figure 3.15: Comparing fixed with linearly variable manual threshold

On the top, a -2 dB fixed threshold (horizontal white line) applied to a particular EM 2040D swath (flat seafloor). At the bottom, the same -2 dB threshold entered by the user, but now with the implementation of linear variability with range (slope ~ 0.014 dB/time sample). The blue line represents the highest amplitude for each time slice. Note that, even with the TVG applied, intensities slightly decay after the minimum slant range (MSR). The second configuration results in more solutions to the outer beams (yellow ellipse) and less toward the nadir

3.4.2 Automatic Thresholding

Normally, as the seabed backscatter level varies spatially, the threshold should be adaptive. Additionally, as the noise floor rises with time, the threshold should identify the cutoff of usable data. Similarly, when shadows (no seabed detections) occur, the threshold criteria should identify and reject these time windows. Thus, an automatic threshold algorithm must consider all these requirements.

The automatic thresholding algorithm developed for this research calculates the “most appropriate” and unique threshold value for each time slice without input from the user. Calculation is based on the strengths of side lobes relative to the main lobe for each normalized time slice (as in Fig. 3.13C). The algorithm works as follows:

1st Step: For each time slice (Fig. 3.16), identify all peaks in the angle series plot and their maximum (*max*) and minimum (*min*) values, as in Fig. 3.13A (blue and red lines, respectively).

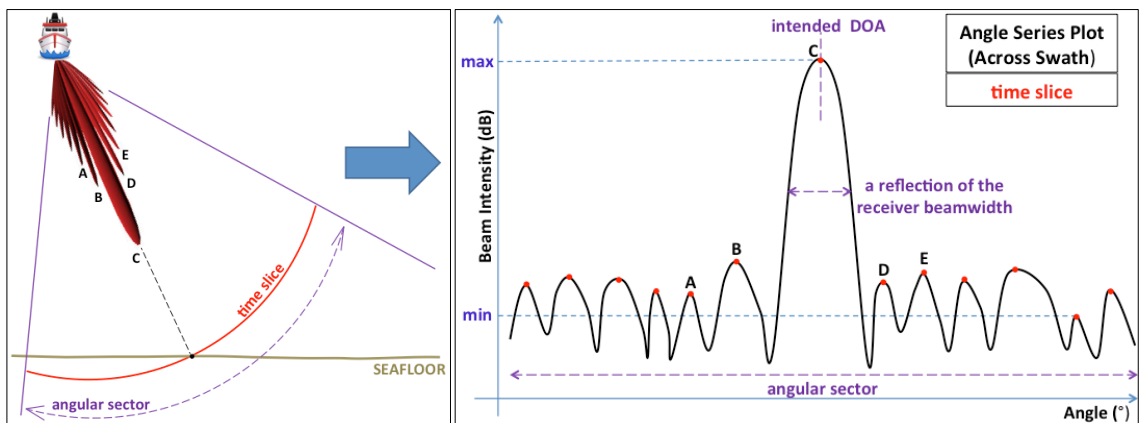


Figure 3.16: Automatic threshold algorithm – Step 1

Identification of all peaks (red dots in the right-hand image) and their maximum and minimum values

2nd Step: For each time slice (Fig. 3.17), calculate the mean of all peaks ($mean_{all}$) and the mean between the maximum and minimum peaks ($mean_{max_min}$) in the angle series plot. Thereafter, open up an interval of 10% of ($max - min$) centered on $mean_{max_min}$. Limits of the interval are defined by [$limit_{lower}$; $limit_{upper}$],

where

$$limit_{lower} = max - 0.55 * (max - min), \text{ and}$$

$$limit_{upper} = max - 0.45 * (max - min).$$

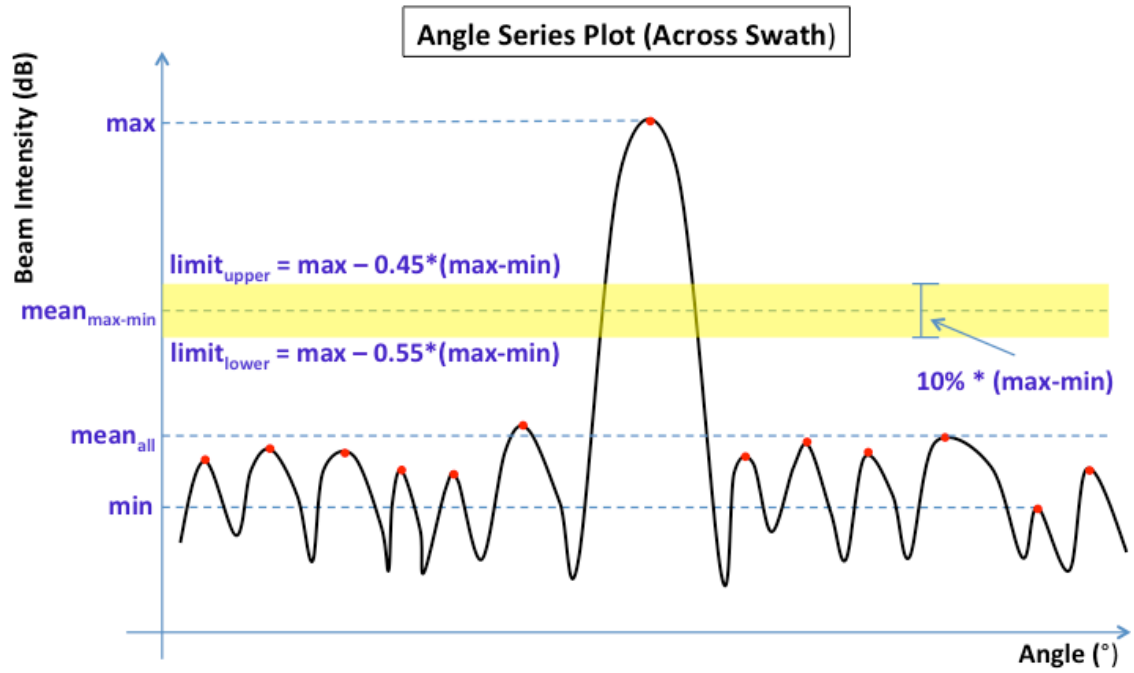


Figure 3.17: Automatic threshold algorithm – Step 2

Calculation of $mean_{all}$, $mean_{max_min}$, $limit_{lower}$, and $limit_{upper}$

3rd Step (final): Apply the following rule to define the threshold:

- (1) If $mean_{all}$ is outside the interval [$limit_{lower}$; $limit_{upper}$] (case of Fig. 3.17), which means that one or more strong peaks (“main lobes” or

detections) are pushing $mean_{max_min}$ upward, the threshold is set to:
 $max - 0.15 * (max - min)$. In this case, all distinct peaks above the threshold are solutions to be considered (Fig. 3.18).

- (2) Otherwise, which means that all peaks have very similar intensities (or the lack of one or more “main lobes”), the threshold is set to a high value above which it does not expect any echo intensity (100 dB). In this case, for the time slice considered, no detection is found (Fig. 3.19).

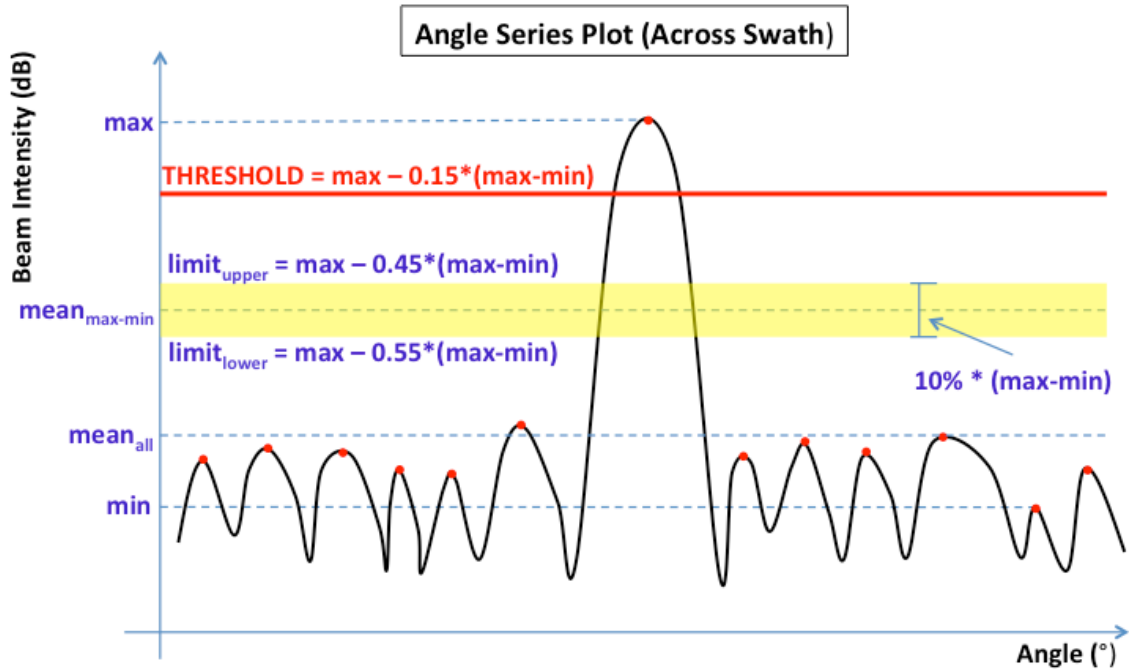


Figure 3.18: Automatic threshold algorithm – Step 3 (case 1)

Threshold definition. If $mean_{all} < limit_{lower}$ or $mean_{all} > limit_{upper}$, the threshold is set to:
 $max - 0.15 * (max - min)$

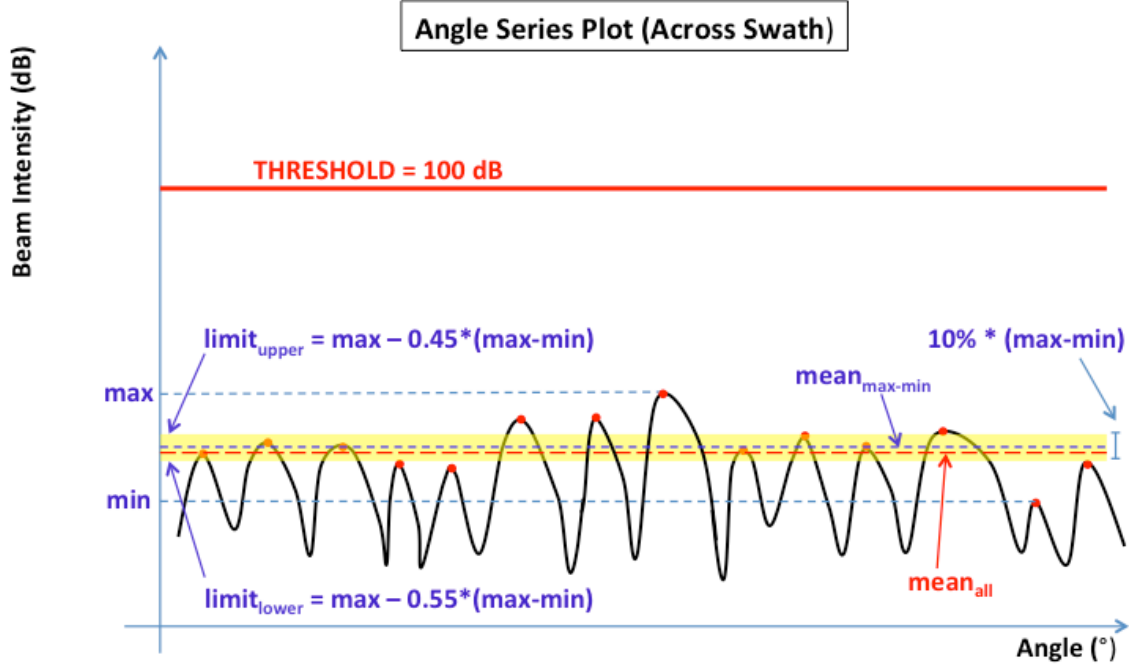


Figure 3.19: Automatic threshold algorithm – Step 3 (case 2)

Threshold definition. If $lower_{limit} \leq mean_{all} \leq upper_{limit}$, the threshold is set to a high value above which it does not expect any echo intensity (100 dB)

This automatic threshold technique capitalizes on the significant difference in terms of intensity between the main and side lobes. When detections occur, as only a few strong peaks (main lobes) are expected amidst many almost-equal weak noise peaks (side lobes), the mean of all peaks is slightly displaced upward if compared with a situation with no detection. On the other, the mean between the maximum and minimum peaks is strongly pushed upward when a detection is found. This, however, does not happen in the absence of detections. In this case, the two means will be very close. The proximity (or not) between $mean_{all}$ and $mean_{max_min}$ is, therefore, the key to the threshold definition.

One of the main limitations on the automatic thresholding algorithm developed for this thesis is the minimum number of peaks required to allow the threshold

computation. The algorithm only calculates a threshold if the number of peaks is at least three. It does not make sense when that value is less than three. In this case, $mean_{all}$ is always equal to $mean_{max_min}$, and no solution is computed. Usually, this situation occurs when the bottom tracking is located in both regions of the outermost beams and the most distant time slices simultaneously. As the WC samples of the inner beams in that intersection region are not made available for the user (although they are available in real time to KM), often the number of peaks is not enough to allow the automatic threshold calculation (Fig. 3.20). To circumvent this situation, the developed algorithm applies the last calculated threshold value for the TWTT with insufficient peaks.

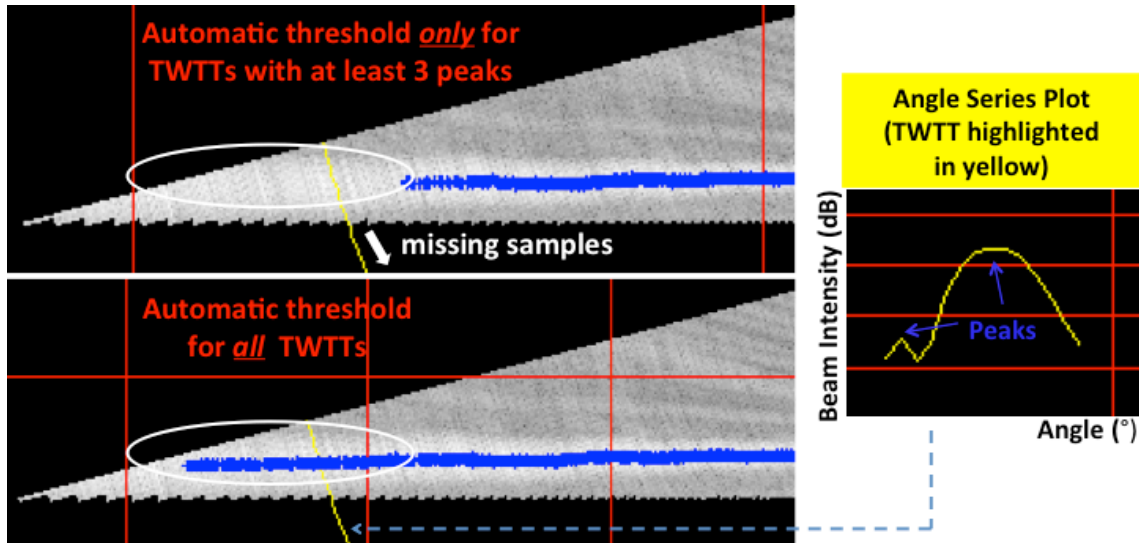


Figure 3.20: The limitation on the minimum number of three peaks required to allow automatic thresholding calculation

Section of the same EM 2040D swath in the outermost region by applying automatic threshold BDI, considering: (top figure) only TWTTs with at least three peaks, and (bottom figure) all TWTTs. Note that only two peaks are identified in the angle series plot for the particular TWTT highlighted in yellow. This happens because the manufacturer does not provide the samples of the inner beams in that region (white arrow). Thus, calculation of automatic threshold becomes not viable. To avoid losing solutions within the affected area (white ellipse), the algorithm considers, for those TWTTs with less than three peaks, the last usable (calculated) threshold

3.5 Sector Boundaries

Most MBES today make use of several across-track sectors with different transmit steering angles (case of EM 2040D—up to three sectors). This technique is, fundamentally, an attempt to make the along-track sounding density as uniform as possible. The pitch and yaw experienced by the surveying platform might make the along-track sounding density strongly uneven, depending on the amplitude of the movements. For that reason, steerable sectoring was implemented to compensate, in real time, for those irregularities.

Adjacent beams belonging to different sectors may have transmit steering angles with opposite directions. Depending on the difference of steering, elevation angle, and depth, those beams might be pointing out to completely distinct seabed locations (Fig. 3.21). In reality, each sector may be considered an independent swath. Therefore, parabola fitting involving samples from different sectors is inappropriate because they are not representing the same seafloor point.

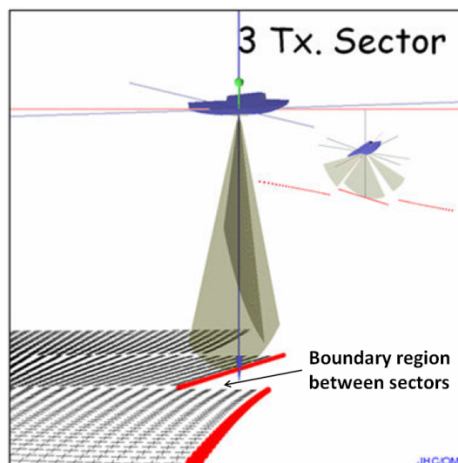


Figure 3.21: Illustrating the boundary region between sectors (after Hughes Clarke, 2013b)

It is not appropriate to compare samples of adjacent beams from distinct sectors for the same time slice because they are not representing the same seafloor point

For that reason, the algorithm developed for this thesis does not consider as potential solutions the highest peaks that are on the sector boundaries. In addition to the beam with the highest intensity, three- and five-point parabola fitting require the use of samples from one or two of its adjacent beams in each side, respectively. Thus, for three-point parabola, the first and last beams of each sector are discarded, which means that no solution is calculated within those beams. If the five-point parabola is applied, the discarding extends to the second and second-to-last beams. The end result is a data gap on the sector boundaries, which is more pronounced in the five-point parabola BDI (Fig. 3.22).

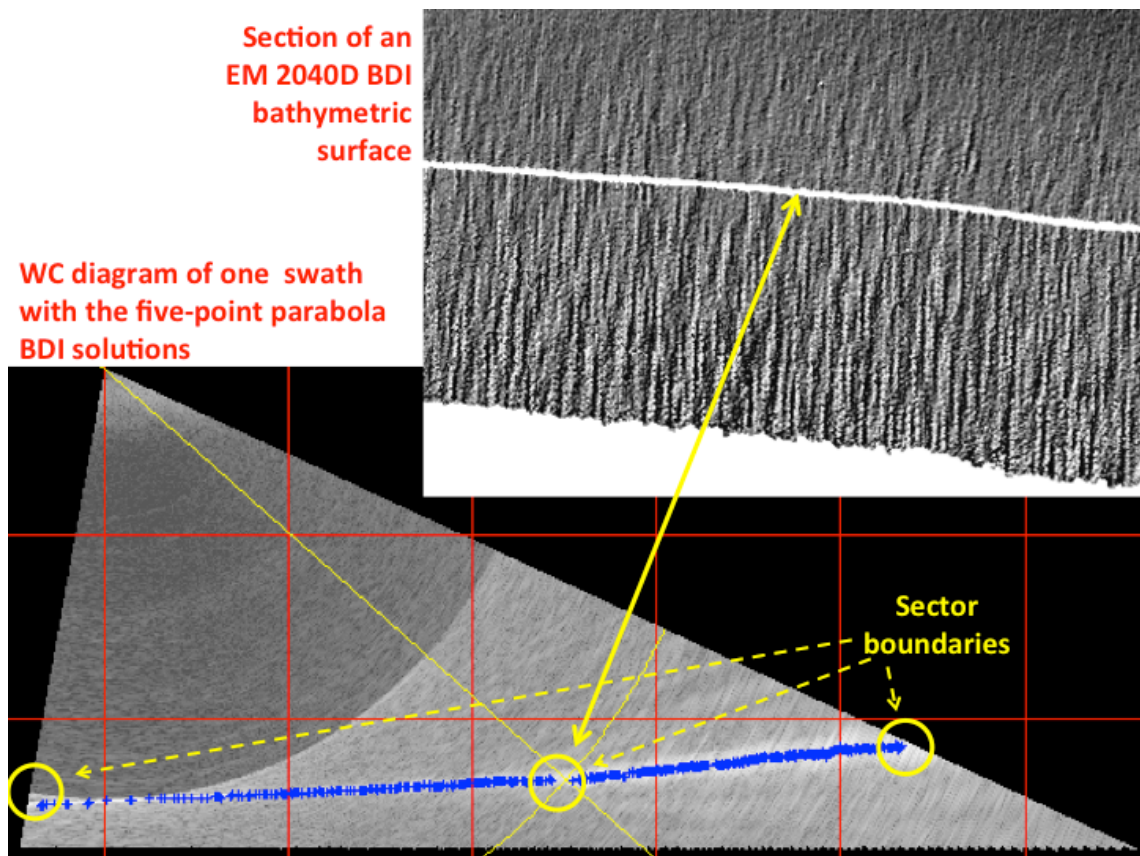


Figure 3.22: Example of a data gap on the sector boundaries caused by the application of five-point parabola BDI

3.6 Minimum Slant Range (MSR)

During the development of this thesis, calculation of the minimum slant range (MSR) was required so it could be incorporated into the filtering algorithm (section 3.7). The MSR is the shortest distance between the receiver and the section of the bottom ensonified by the transmitter. It represents the moment when the transmitted sound wave first touches the seabed. In a WC pie diagram, the MSR is identified by the arc of circle that separates the region with low (usually darker) from high (usually brighter) backscatter level (Fig. 3.23). The calculation of the MSR was needed because the BDI algorithm, by applying either manual or automatic threshold, may pick, as false solutions, spurious noise peaks in the data collected before the first seabed echo. The MSR then will be used as a cut-off filter for all those “spikes” that are eventually found before it.

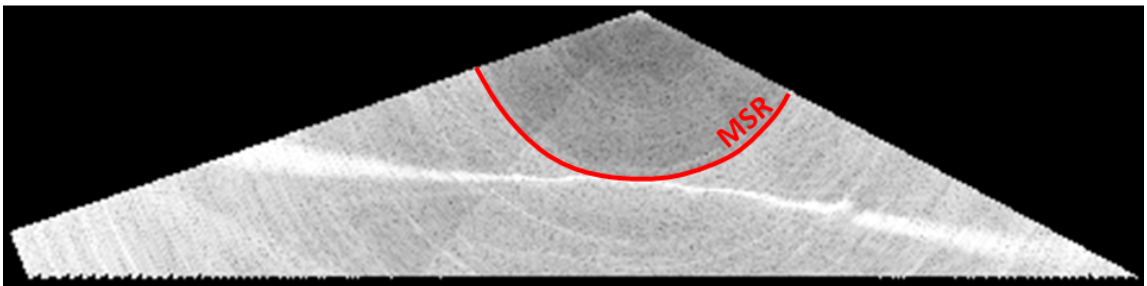


Figure 3.23: The MSR identification in the WC pie diagram

Another way of graphically identifying the MSR is to plot for each time slice the mean of all peaks (averaged backscatter level), calculated from the angle series plot (as described in the 1st and 2nd steps of section 3.4.2). A generic graphic is shown in Fig. 3.24. In the figure, it is possible to see the “leap” from the low to high backscatter region that denotes the MSR.

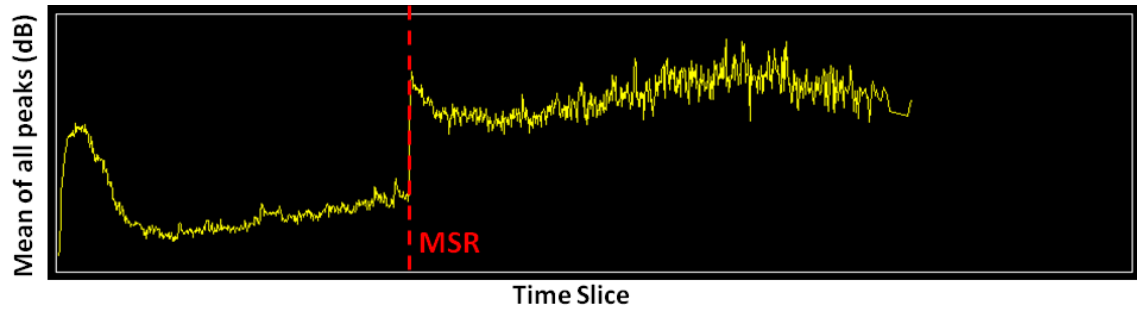


Figure 3.24: The MSR identification based on the plot of the mean of all peaks for each time slice

The MSR calculation developed for this research is based on the proper identification of the “leap” observed on the graphic shown in Fig. 3.24. The algorithm proceeds as follows:

1st Step: Calculate a 21-sample moving average and corresponding standard deviation for each time slice represented in Fig. 3.24. The time slice considered and ten samples before and after are used.

2nd Step (final): Identify the highest standard deviation within the swath. As the MSR corresponds to the boundary between the low and high backscatter regions, it is expected that, when the moving average is centered on it, the standard deviation will be maximum. The ten samples before and the ten after will have very similar low and high values, respectively, which maximizes the calculated standard deviation because no other “leap” other than that one associated with the MSR is awaited. The MSR is then the time slice with the highest standard deviation.

3.7 Filtering

The most challenging task in the BDI algorithm is the proper selection of the threshold for each TWTT. Either using manual or automatic thresholding, spurious solutions almost always appear. These undesirable false solutions sometimes may mask the correct localization of the seafloor or even a target.

Using manual threshold and depending on the chosen value, the majority of “spikes” occur in the region below the actual seafloor. The time slices after the real bottom of the outermost beam present most of the false solutions (Fig. 3.25).

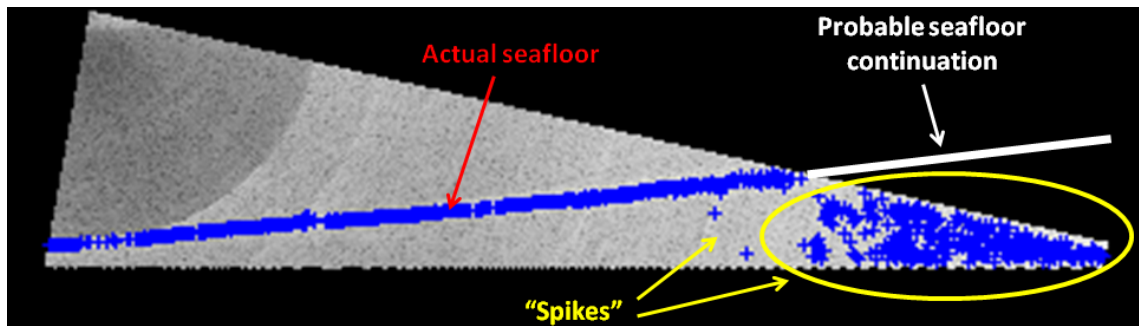


Figure 3.25: False BDI solutions in manual threshold

Note that most of fake solutions are concentrated in the region within the yellow ellipse

Regarding automatic threshold, false BDI solutions may appear anywhere. A significant number of solutions fall in the region prior to the MSR (Fig. 3.26).

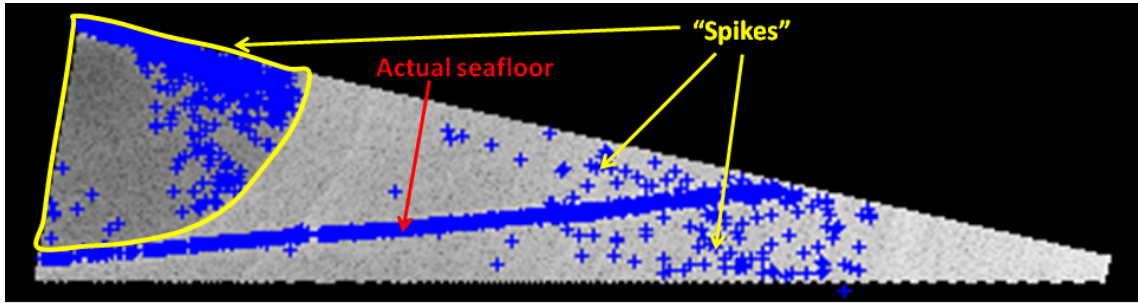


Figure 3.26: False BDI solutions in automatic threshold

Note that most of fake solutions are concentrated in the region before the MSR (within yellow closed curve)

Those erroneous BDI solutions clearly reveal the limitations both in manual and in automatic thresholding. To get around these imperfections, a filter algorithm was developed. It is based on the concept that, for a flat bottom, the across-track beam footprint increases while the bottom-projected pulse length decreases with the increase of the beam angle. Therefore, the greater the beam angle, the higher the number of potential BDI solutions and the more dispersed they are.

During the filter design, the governing idea was to maximize the “spike” elimination while preserving as much as possible of the actual solutions. This challenging assignment is extremely delicate, as actual targets on the bottom could potentially be incorrectly removed in the case of improper design and calibration of the filter. The filter algorithm works as follows:

1st Step: Delete all solutions before the MSR. Note that any possible object tracked by the BDI algorithm before the MSR, such as a large fish or the top of a mast, is filtered out. For the purposes of this research, that is not an issue because the focus is on the seabed objects at low grazing angles.

2nd Step: For each physical beam, calculate a sample-number-based mean (μ_{cal}) and standard deviation (σ_{cal}) of all remaining BDI solutions within the solid angle. Both statistics are weighted by the sample intensity with respect to the mean backscatter level at the TWTT considered (mean of all peaks in the angle series plot).

3rd Step: For each beam, calculate a maximum allowable sample-number-based standard deviation (σ_{max}). Firstly, based on a previous analysis of the data, the user chooses the most suitable σ_{max} for the outermost beam (an integer value ≥ 2 samples), herein denominated Filter Index. Secondly, assuming a flat seafloor, the algorithm linearly distributes that chosen value from the outermost beam to the nadir beam, where σ_{max} is preset to 1.5 samples. This value was adopted because it does not expect, for the nadir beam in shallow waters, a higher dispersion of BDI solutions. Normally, the seafloor within the nadir beam is covered by only one time sample (beam-limited instantaneous ensonified area), which means no dispersion of BDI solutions. Therefore, for the purposes of this thesis, σ_{max} equal to 1.5 samples at the nadir beam is wide enough. Figure 3.27 clarifies this procedure.

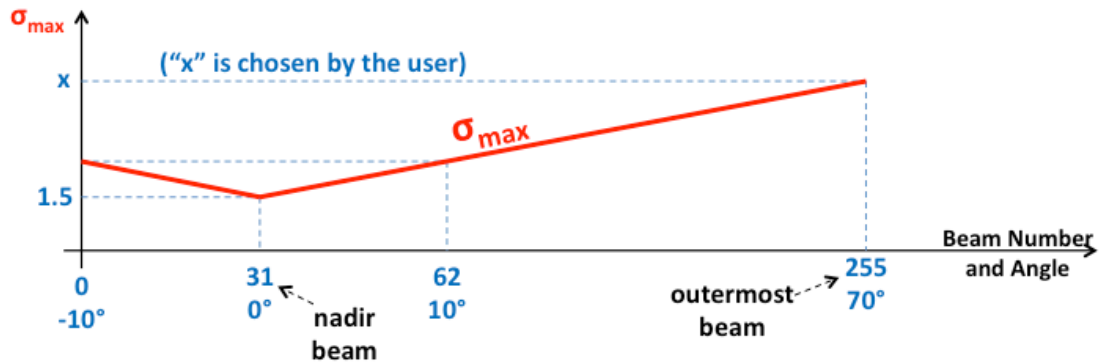


Figure 3.27: Maximum allowable sample-number-based standard deviation (σ_{max})

In this example, the swath contains 256 beams, spanning from -10° to 70° . Nadir beam number is 31

The linear distribution used to calculate σ_{\max} is merely an approximation. A more precise computation of the expected σ_{\max} should consider, for each beam: (1) the total number of time slices within the bottom interaction window, (2) the number of time slices with solutions, (3) how concentrated or dispersed they are, and (4) the weight of each solution.

4th Step (final): For each beam, compare σ_{cal} and σ_{\max} . If $\sigma_{\text{cal}} \leq \sigma_{\max}$ (condition of maximum dispersion), all remaining BDI solutions are conserved. Otherwise, the algorithm eliminates the farthest solution (with respect to μ_{cal}) and recalculates μ_{cal} and σ_{cal} . The process is iteratively executed until the condition of maximum dispersion is met (Fig. 3.28).

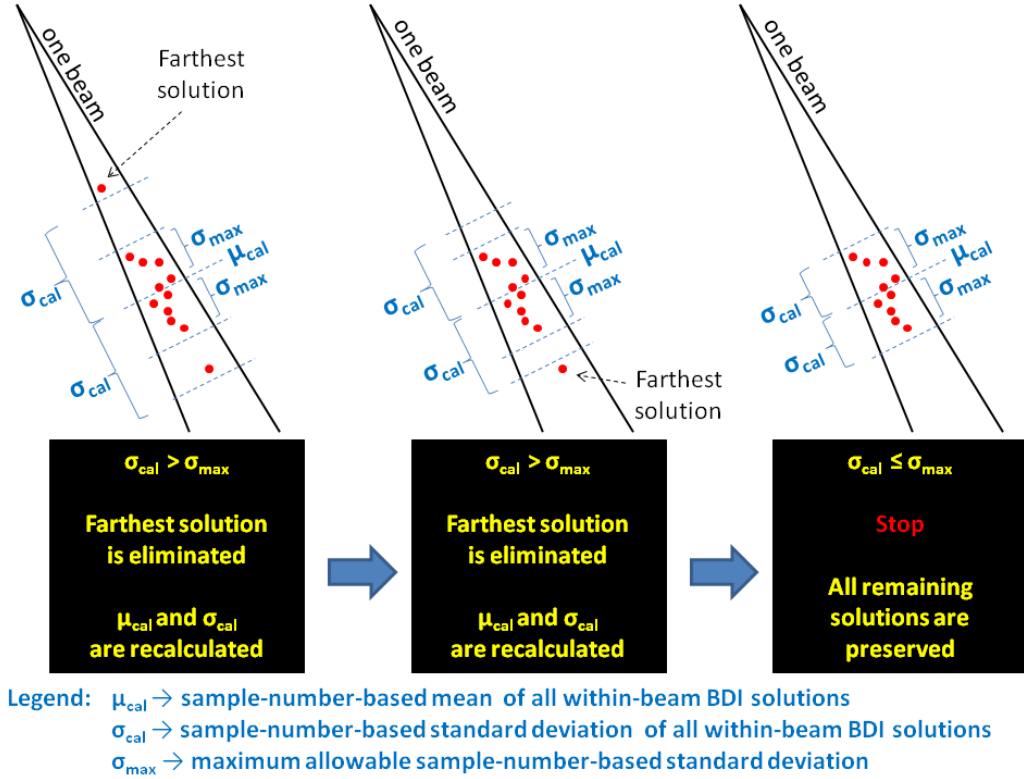


Figure 3.28: The within-beam BDI filtering process (final step)

Figures 3.29 and 3.30 compare before and after application of filtering for manual and automatic threshold BDI, respectively. As can be seen, the algorithm retains most solutions in the actual seafloor. On the other hand, it practically removes all “spikes.”

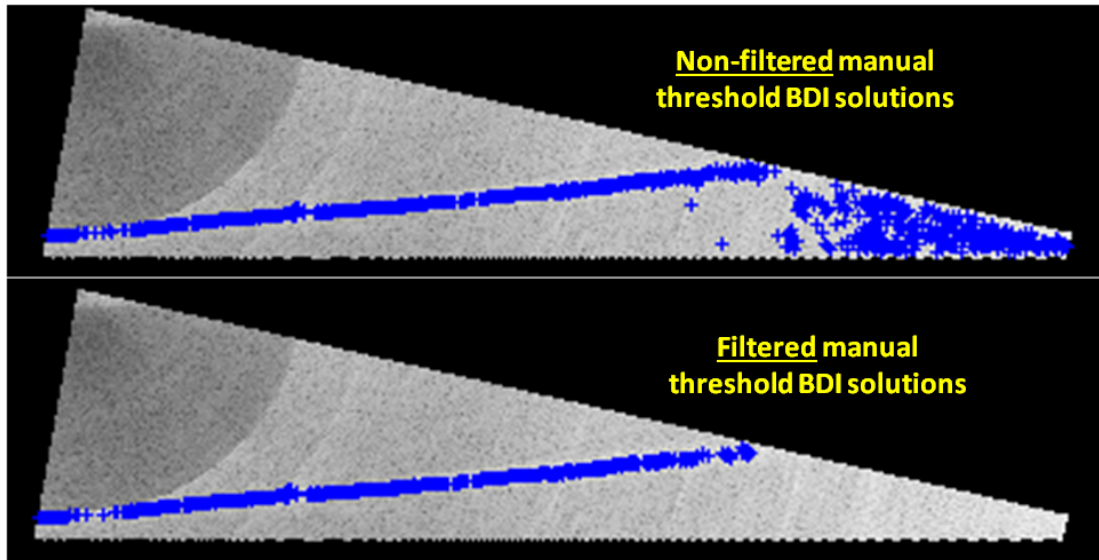


Figure 3.29: Comparing before and after filtering for manual threshold BDI (Filter Index = 9)

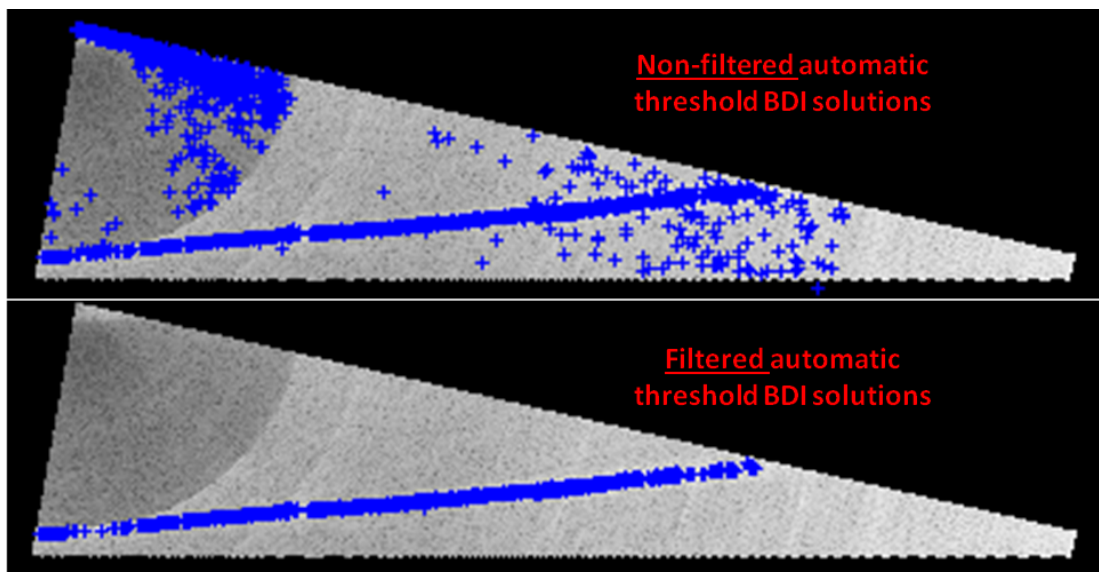


Figure 3.30: Comparing before and after filtering for automatic threshold BDI (Filter Index = 9)

Additionally, to allow the assessment of the algorithm under the presence of a seabed object (focus of this thesis), Fig. 3.31 presents a comparison between before and after filtering in the vicinity of a target. As can be seen, the solutions over the target are almost entirely preserved. Only a few solutions in the target shadow area are lost. For the purposes of this thesis, therefore, the BDI filtering algorithm has showed to be suitable.

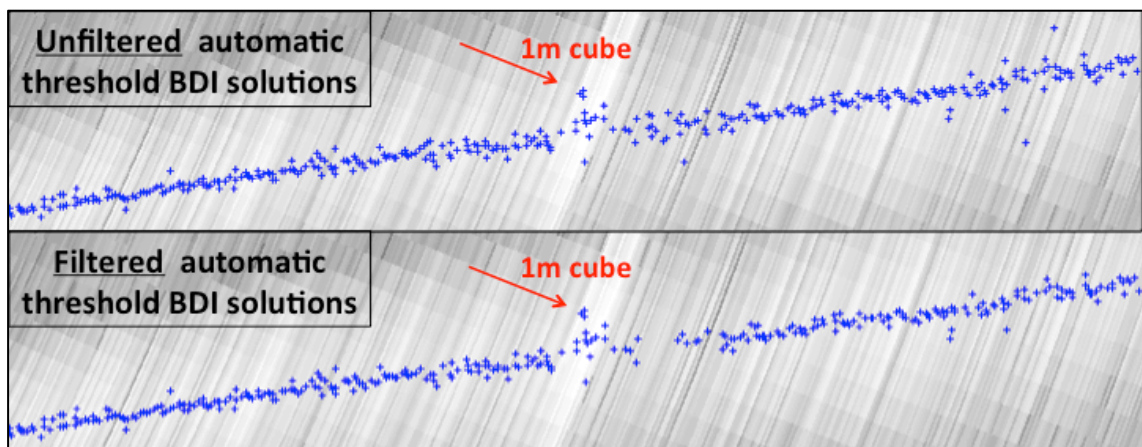


Figure 3.31: Comparing BDI solutions before and after filtering in the vicinity of a 1-meter cube at 40 m depth (Filter Index = 9)

In this EM2040D example, the target is seen at $+67^\circ$. Note that the filtering algorithm eliminates some spurious solutions above and below seafloor, but preserves data density over the target. The only drawback is loss of some target shadow data

3.8 Compression

In normal mode, EM 2040D provides up to 256 depth solutions per receiver, which means a maximum of one solution per physical beam forming channel. In high density mode, up to 400 solutions per receiver are provided, meaning approximately a maximum average of 1.56 solutions per physical beam, with generally more per beam at higher incidence angles.

One of the main characteristics of DOA-refined BDI is the possibility of having as many solutions as the number of time slices within the bottom interaction window for each beam. Depending on the amplitude threshold applied, the time sampling, and the number of time slices that cover the seafloor, the DOA-refined BDI might provide more than 400 solutions per receiver, thereby potentially improving across-track sounding density and short-wavelength feature definition, especially at low grazing angles. This is one of the benefits of BDI. However, by sampling all time slices, some solutions may be contaminated by noise, resulting in misleading representation of the actual seabed topography. Hence, it is necessary to find a balance between finer sampling and averaging to promote noise suppression.

Given that averaging of some BDI solutions might reduce noise on a smooth seafloor, but too much averaging could dampen out the expression of targets, what is a suitable level of sample combination on compression? What happens if the BDI solutions are compressed to deliver up to the same number of solutions provided by the manufacturer? This adds the convenience that the BDI solutions can be written out in the same structure size. Is the target detection capability still improved? To answer these questions and also to expand the range of this research, a compression algorithm was developed. Basically, the algorithm reduces data by averaging small and successive seabed sections so that an equidistant sampling of the bottom may be obtained. It works as follows:

1st Step: Assume that the seafloor is flat (Fig. 3.32).

2nd Step: Based on the angular sector and the MSR approximate depth, calculate the across-track swath width (Fig. 3.32).

3rd Step: Divide the across-track swath width into n (user-defined) equal footprints (Fig. 3.32).

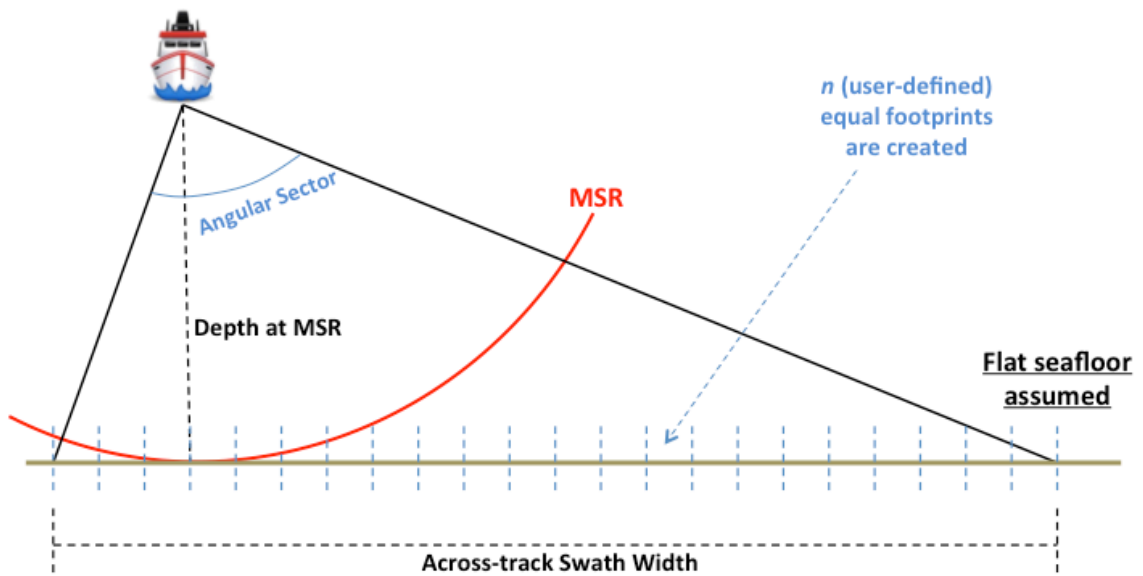


Figure 3.32: Illustrating the 1st, 2nd, and 3rd steps of the compression algorithm

4th Step: Based on the footprints, create n equidistant virtual beams (Fig. 3.33). Each virtual beam axis coincides with the geometric center of one footprint. The limits of each footprint define the corresponding virtual beamwidth. The virtual beamwidth and spacing are, therefore, variable. Virtual beams close to nadir are wider. As they move to the outer region, the virtual beamwidth gradually reduces.

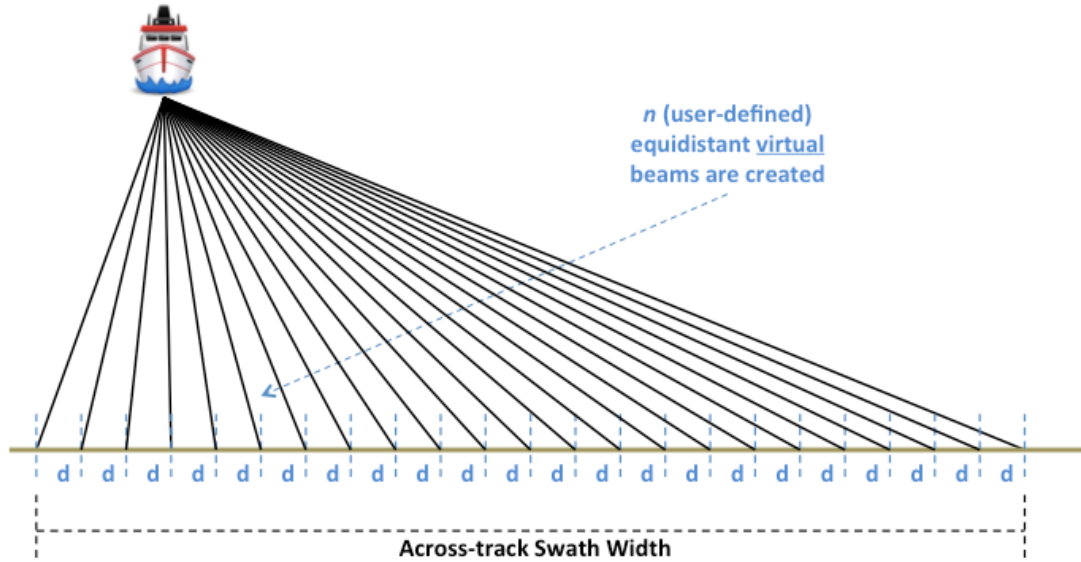


Figure 3.33: Illustrating the 4th step of the compression algorithm

5th Step (final): For each virtual beam, calculate two means for all BDI solutions within it: a sample-number-based mean (μ_{time}) and DOA-based mean (μ_{angle}). Afterward, compress the solutions. Both statistics are weighted by the sample intensity with respect to the mean backscatter level at the TWTT considered (mean of all peaks in the angle series plot). The compression works by replacing all within-virtual-beam BDI solutions by the corresponding $\mu_{\text{time}}/\mu_{\text{angle}}$ pair (Fig. 3.34), thus resulting in a maximum of one BDI solution per virtual beam.

Note that the averaging is performed over a range of angles significantly narrower than the physical beamwidth. Also, the final angle result is not necessarily the virtual beam axis. In addition to the flat seafloor assumption, this potentially off-axis solution degrades the initial attempt to achieve an equidistant sampling of the bottom after compression. Additionally, unlike the original SeaBeam[®] (2000) approach, the

solution angular spacing is not equiangular and is significantly finer than the physical beamwidth.

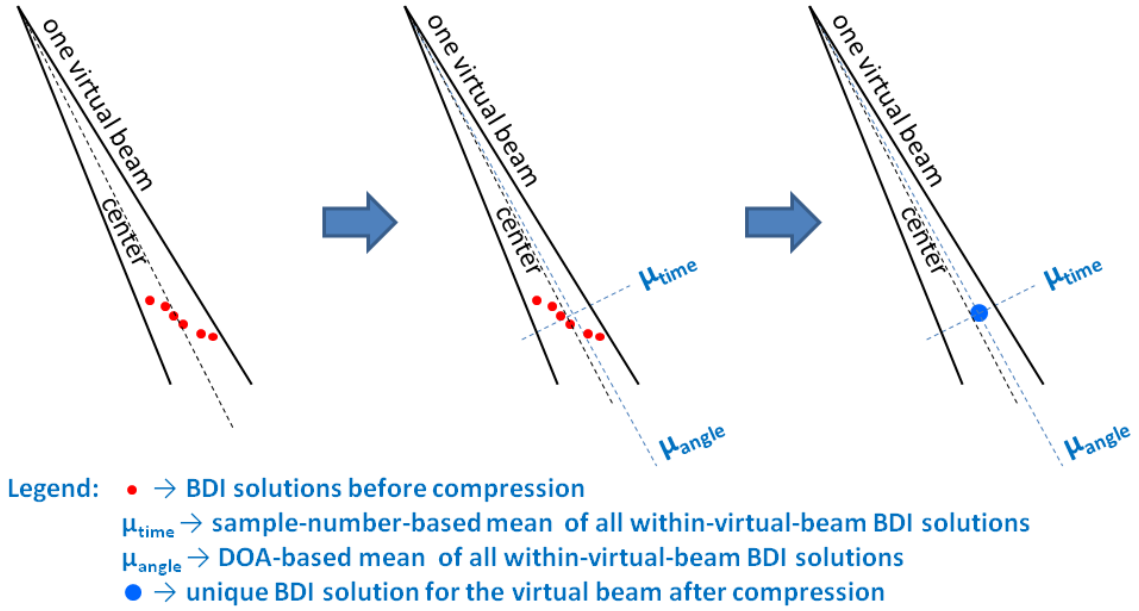


Figure 3.34: Illustrating the 5th step (final) of the compression algorithm

Figure 3.35 shows a section of the same EM 2040D swath before and after application of the BDI compression algorithm. As can be seen, the algorithm keeps the general shape of the seafloor and tries to sample it as equidistant as possible. Also, note that it eliminates some spurious solutions that abut the seabed.

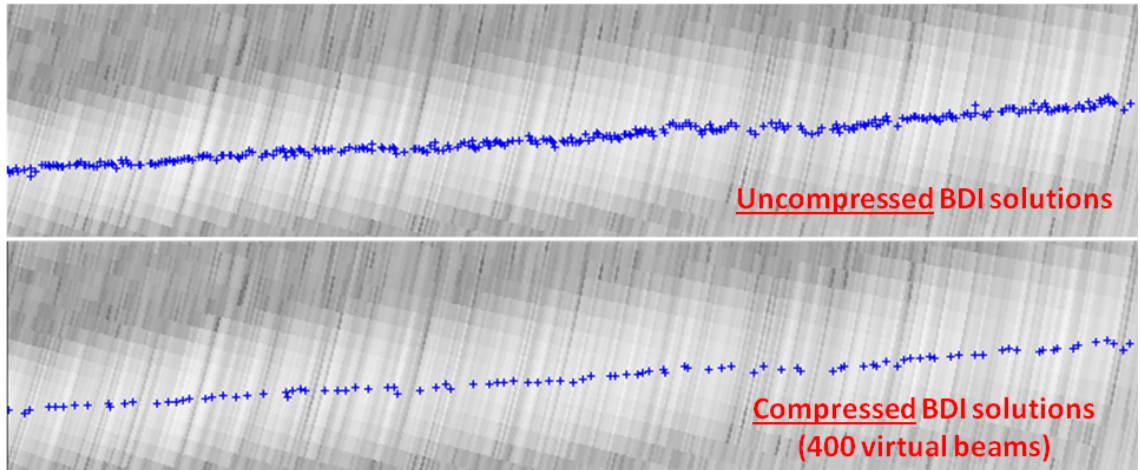


Figure 3.35: Comparing before (top) and after (bottom) application of the compression algorithm (400 virtual beams)

4. Tests, Results, and Analyses

4.1 Test Area

The algorithm developed to support this thesis was tested using appropriate datasets collected over a site with many anthropogenic objects. The area is located at the Saanich Inlet, close to the city of Sidney, British Columbia (BC), Canada (Fig. 4.1).

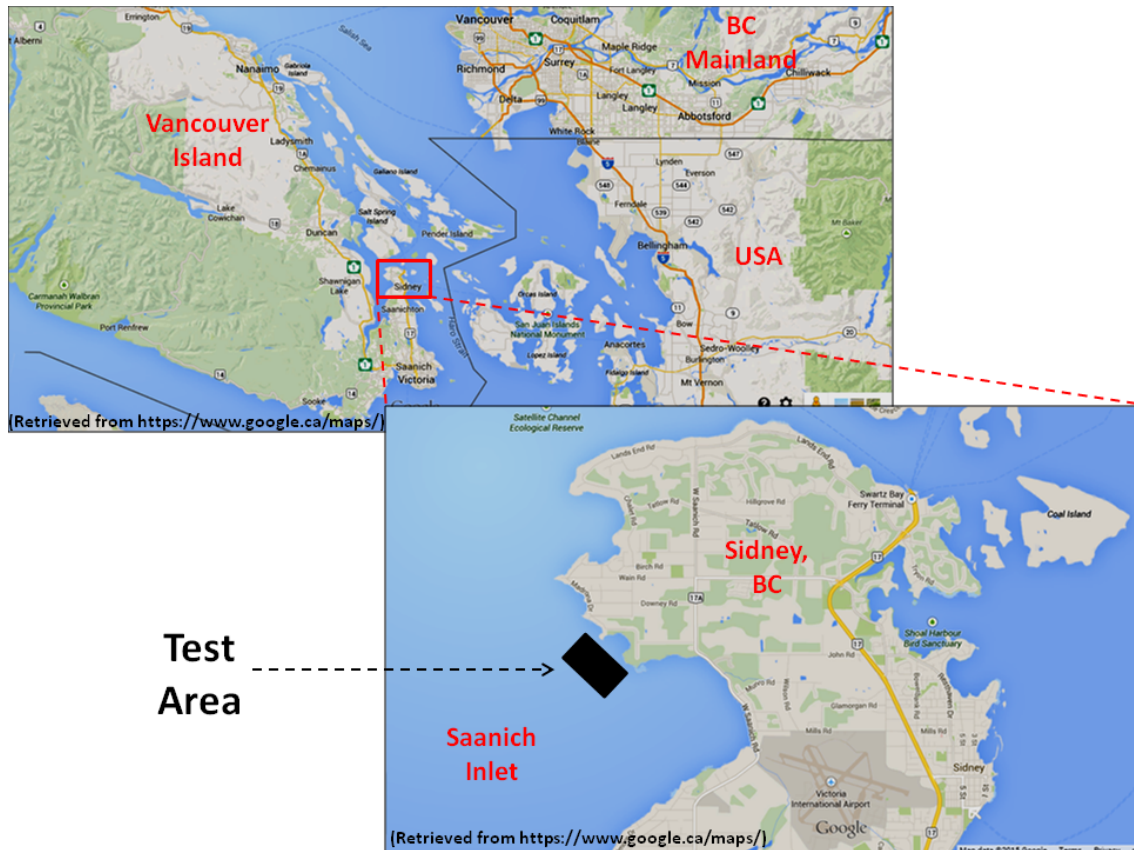


Figure 4.1: Test Area

In 2011, the United States Navy's Naval Oceanographic Office (NavO) deposited on the seabed of the test area a series of ten unnatural concrete cubes. Four 1-meter cubes were laid along the 40 m contour, three of them with attached concrete poles on their top faces. Two 1-meter and four 0.5-meter cubes were laid along the 20 m contour.

One 1-meter and one 0.5-meter cubes of this second line of targets also have protrusions (Fig. 4.2). This test area was artificially created to allow NavO to assess the target detection capability of its MBES installed in launches.

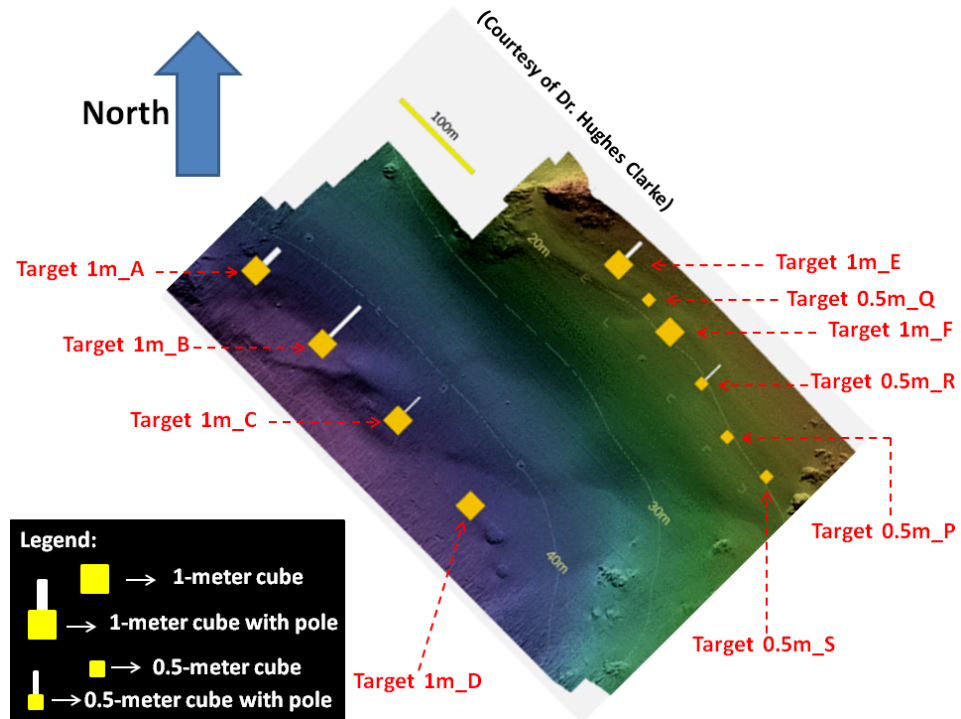


Figure 4.2: Target schema of the test area

4.2 Test Data

Two datasets were used to test the BDI algorithm. The data were collected by NavO and OMG in the summers of 2013 and 2014 using an EM 2040D in various swath aperture dispositions (Hughes Clarke, 2014). The following configuration was set: 300 kHz, 8 knots, dual swath, three sectors, and HDBF mode. In both years, WC data were retained. Several corridor lines were run in the test area. This allowed to image the targets at different incidence angles, ranging from 0° to $\pm 82^\circ$.

The tests and analyses performed in this thesis are restricted to only three targets without poles (Fig. 4.2) when ensonified at low grazing angles: **1m_D (40 m)**, **1m_F (20 m)**, and **0.5m_Q (20 m)**. The IHO-compliant 1-meter cubes were used to assess the EM 2040D target detection performance at 20 and 40 m depth. The 0.5-meter cube was examined as an opportunistic test of potential mine-like object (MLO) detection at 20 m depth. The other features with protrusions were not analyzed, as they are not within the scope of this thesis. They provide extensive data to study least depth determination of mast-like objects instead of pure IHO-compliant target detection.

4.3 Target Detection Criterion

The IHO target detection criterion specifies, for each order of survey, the minimum size of features to be detected. What is not stated, however, is which conditions must be met for a feature to be considered successfully detected. This task is up to the IHO members. Each hydrographic office has its own regulations. Some of them do not have any rule, which leads to a subjective interpretation of a successful detection. Brazil and Canada are included in this list of countries without objective target detection requirements.

The most common and utilized method to detect objects on the seafloor is by using sidescan sonars. The low altitude of the sensor with respect to the bottom allows any proud object to be strongly ensonified. Additionally, this near-specular incidence casts a relatively long shadow right after the feature, resulting in a contrasting high-low backscatter region, generally easily identified in a seafloor backscatter image. That

contrast is the evidence of the feature presence, even though interpretation is purely subjective, sometimes requiring an experienced hydrographer to analyze.

An alternative method to assess the detection of a target considers only the MBES bathymetric solutions. This is, ultimately, the subject of this thesis. In this case, the detection is assessed based on the number of vicinity-relative positive bathymetric solutions over the target in the across- and along-track direction. In this regard, the most accepted rule requires a minimum of 3×3 (across-track \times along-track) shots over the feature (Fig. 4.3).

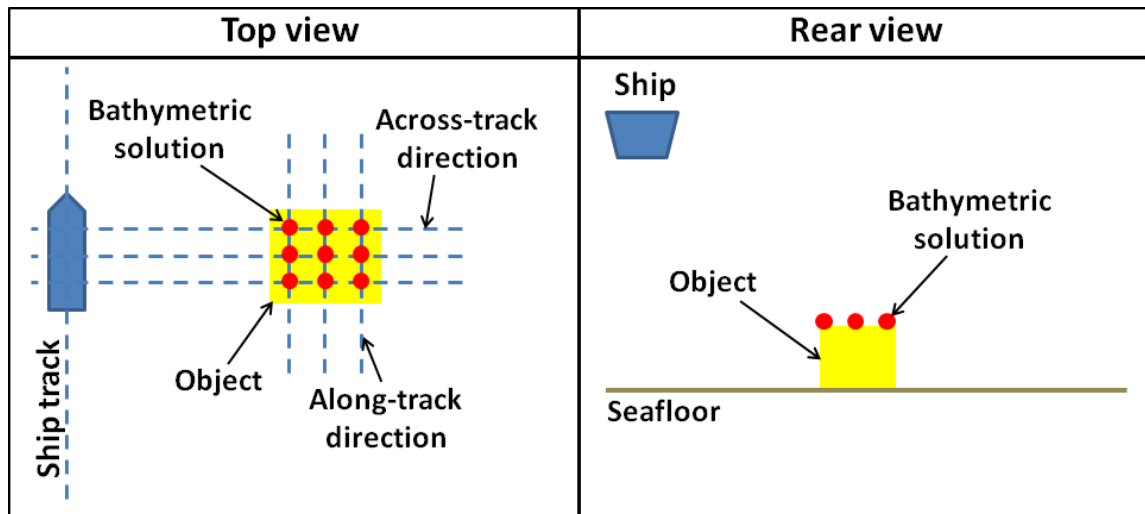


Figure 4.3: The target detection criterion based on a minimum of 3×3 shots

In this research, however, the adopted target detection criterion is less stringent. It is primarily based on the visual analysis of the two-dimensional across- and along-track sounding profiles. A target will be considered successfully detected if a cluster of outlying soundings is observed.

4.4 Data Presentation

The results of the performed tests are presented in the following section 4.5 (as tables with figures). Four image types were generated resulting from the application of a series of preexistent OMG code's subroutine packages over the bathymetric solutions around the target vicinity:

- (1) Sun-illuminated grayscale bathymetric surface with 0.25 m resolution (terrain size: 20 m \times 20 m).
- (2) Two-dimensional across-track sounding profile (terrain size: 4 m \times 4 m. Scale between two consecutive horizontal blue lines: 1 m).
- (3) Two-dimensional along-track sounding profile (terrain size: 4 m \times 4 m. Scale between two consecutive horizontal blue lines: 1 m).
- (4) Pie-diagram-derived WC snapshots with BDI solutions plotted on them for three consecutive swaths over the target and surroundings.

Before the creation of the aforementioned images (1), (2), and (3), the merged file with the new BDI solutions proceeding from the application of the developed subroutine package "applyBDI.c" was submitted to a ray tracing process. This was done by applying the already existent OMG subroutine package "newMergeAtt.c."

For each table, both KM and BDI solutions in the considered mode (automatic or manual threshold, compressed or uncompressed data, etc.) are presented, thus allowing a visual comparison of the different results. Analyses are done after the tables. Two different low grazing angles from the 2013 and/or 2014 dataset are evaluated for each target type (1-meter cube at 40 m and 20 m depth, and 0.5-meter cube at 20 m depth).

The following parameters were used to generate the BDI solutions, as they best suit the test datasets as a whole:

- (1) Five-point parabola fitting (section 3.2.3).
- (2) When applying manual thresholding (section 3.4.1), threshold equal to 0 dB.
- (3) Maximum of one BDI solution per TWTT (section 3.3).
- (4) Filter Index (section 3.7) equal to 9.
- (5) When compressing data (section 3.8), 400 virtual beams (same maximum number of solutions per receiver provided by the manufacturer).

The justification for applying the same parameters is to allow an unbiased analysis of the BDI algorithm, even though each target at each incidence angle might be better revealed using other values.

4.5 Results and Analyses

4.5.1 1-meter cube at 40 m depth

Tables 4.1 and 4.2 present the results from the 2013 dataset for a 1-meter cube at 40 m depth and ensonified at $+67^\circ$ by applying manual and automatic threshold BDI, respectively. Tables 4.3 and 4.4 present the results from the 2014 dataset for the same target, but ensonified at $+68^\circ$.

Table 4.1: 1-meter cube at 40 m depth - manual threshold BDI, 2013 dataset, +67° incidence angle

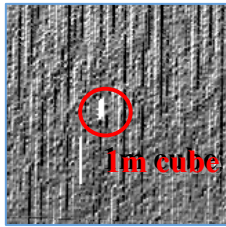
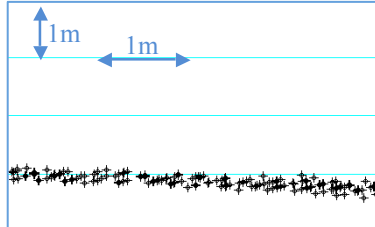
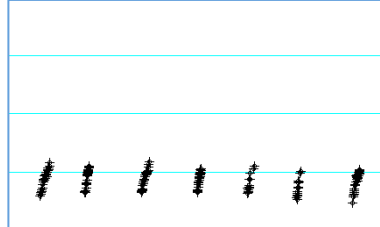
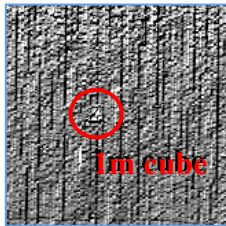
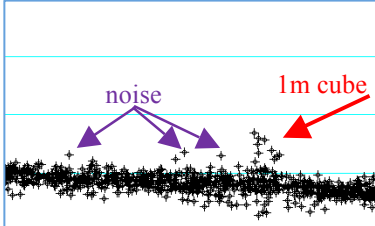
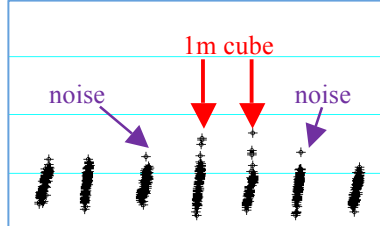
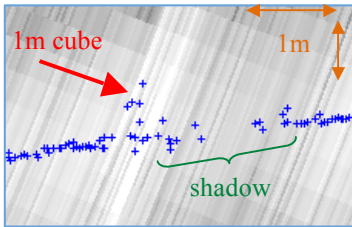
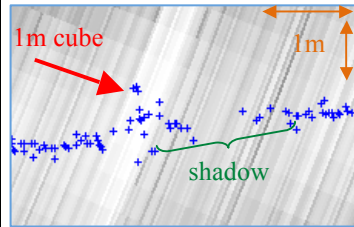
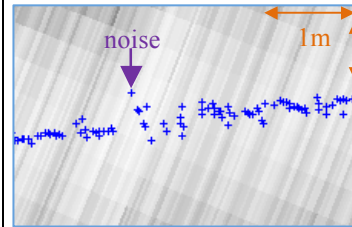
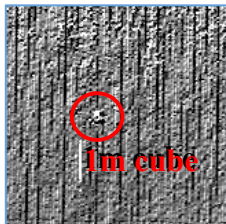
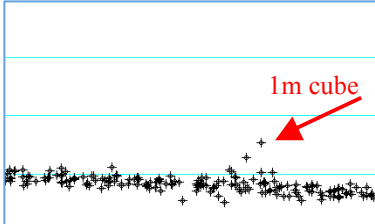
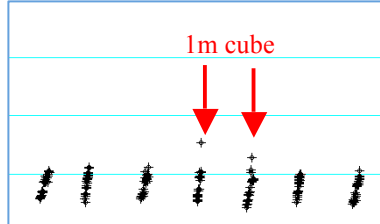
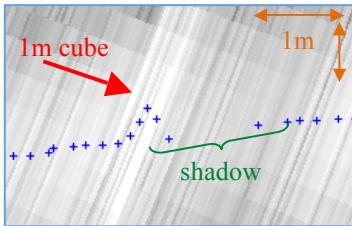
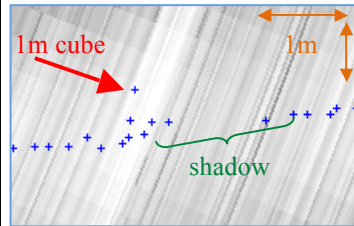
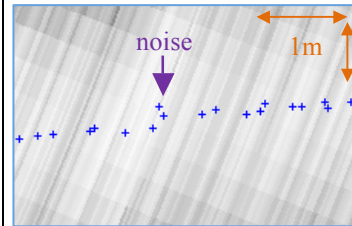
| 2013 Dataset | 40 m Depth | 75° Angular Sector | 1-meter Cube | Line 0020 | +67° Incidence Angle |
|---|--|---|---|-----------|----------------------|
| KM solutions | | | | | |
| Bathymetric surface | Across-track sounding profile | | Along-track sounding profile | | |
|  |  | |  | | |
| BDI solutions – manual threshold 0 dB, uncompressed data | | | | | |
| Bathymetric surface | Across-track sounding profile | | Along-track sounding profile | | |
|  |  | |  | | |
| WC sections – three consecutive swaths | | | | | |
|  |  |  | | | |
| BDI solutions – manual threshold 0 dB, compressed data | | | | | |
| Bathymetric surface | Across-track sounding profile | | Along-track sounding profile | | |
|  |  | |  | | |
| WC sections – three consecutive swaths | | | | | |
|  |  |  | | | |

Table 4.2: 1-meter cube at 40 m depth - automatic threshold BDI, 2013 dataset, +67° incidence angle

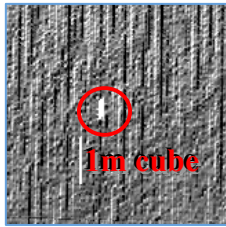
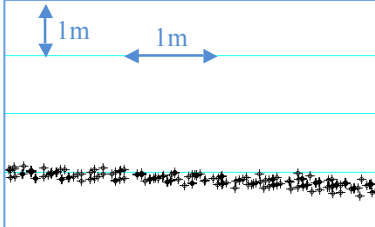
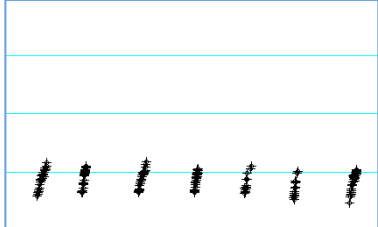
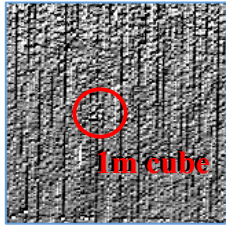
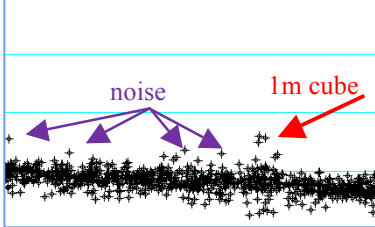
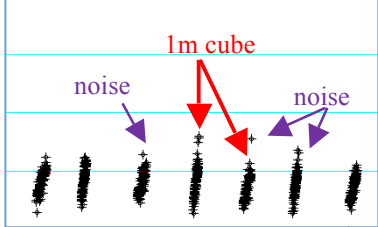
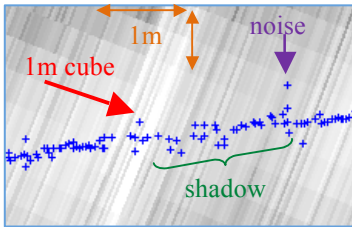
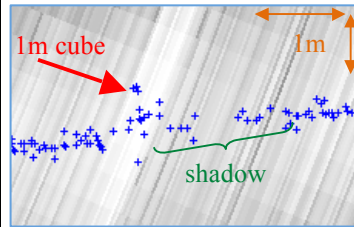
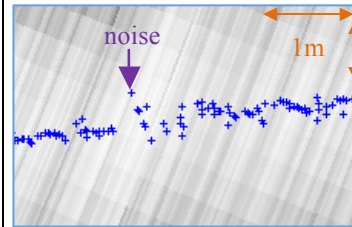
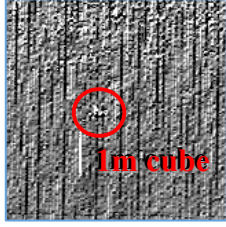
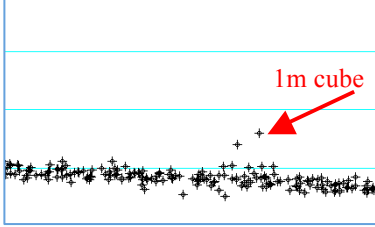
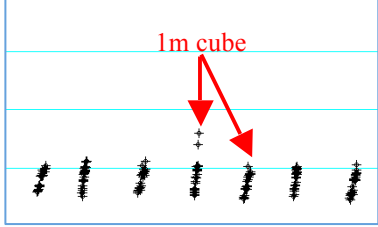
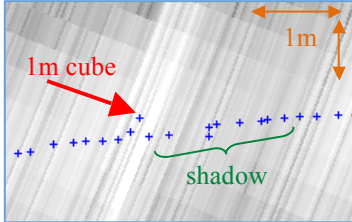
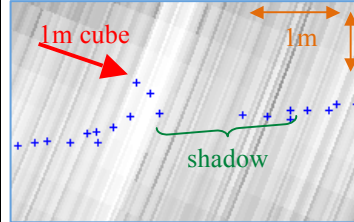
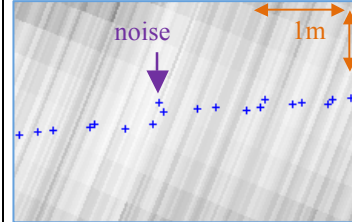
| 2013 Dataset | 40 m Depth | 75° Angular Sector | 1-meter Cube | Line 0020 | +67° Incidence Angle |
|---|--|---|---|-----------|----------------------|
| KM solutions | | | | | |
| Bathymetric surface | Across-track sounding profile | | Along-track sounding profile | | |
|  |  | |  | | |
| BDI solutions – automatic threshold, uncompressed data | | | | | |
| Bathymetric surface | Across-track sounding profile | | Along-track sounding profile | | |
|  |  | |  | | |
| WC sections – three consecutive swaths | | | | | |
|  |  |  | | | |
| BDI solutions – automatic threshold, compressed data | | | | | |
| Bathymetric surface | Across-track sounding profile | | Along-track sounding profile | | |
|  |  | |  | | |
| WC sections – three consecutive swaths | | | | | |
|  |  |  | | | |

Table 4.3: 1-meter cube at 40 m depth - manual threshold BDI, 2014 dataset, +68° incidence angle

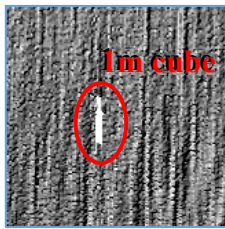
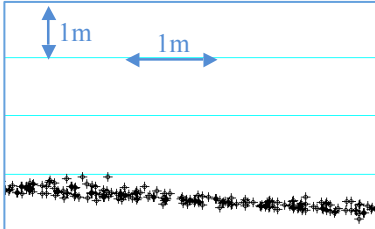
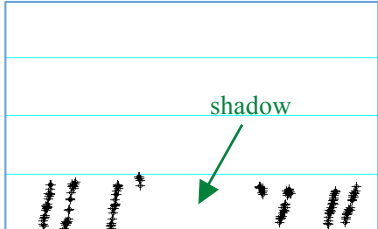
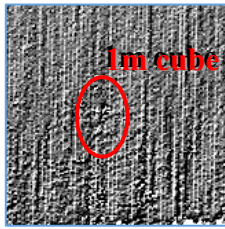
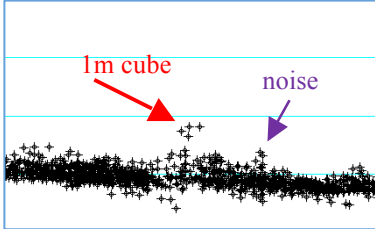
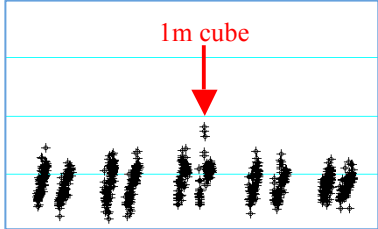
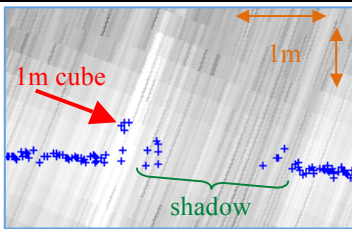
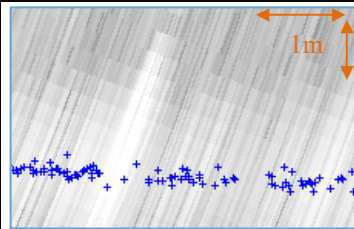
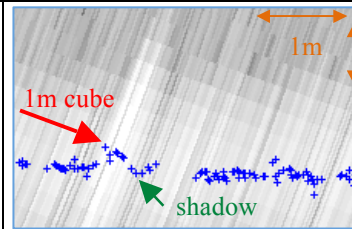
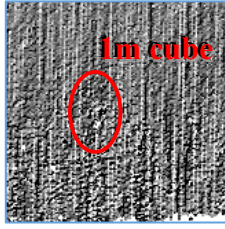
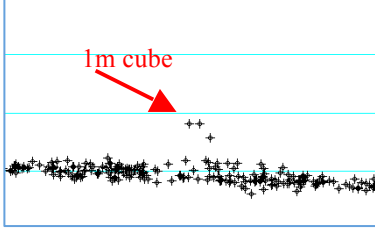
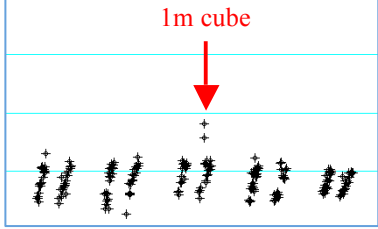
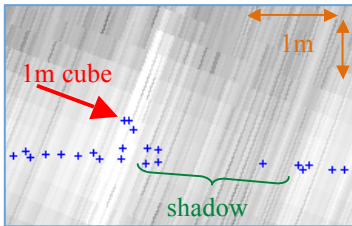
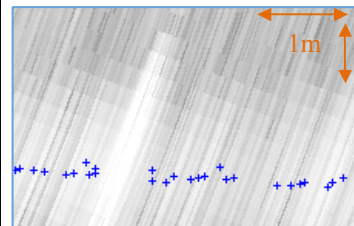
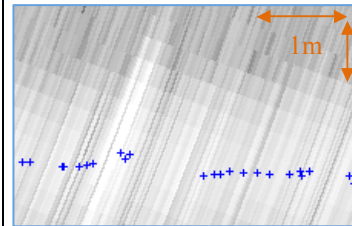

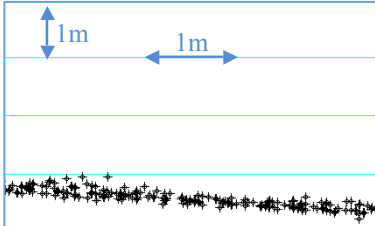
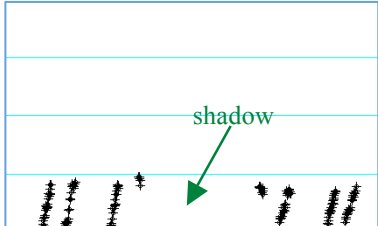
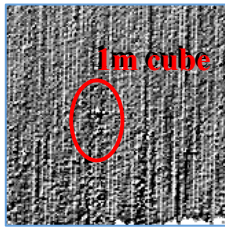
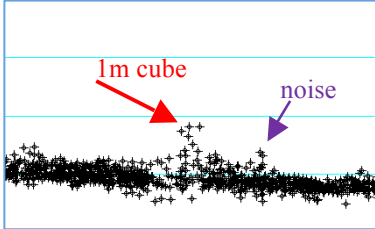
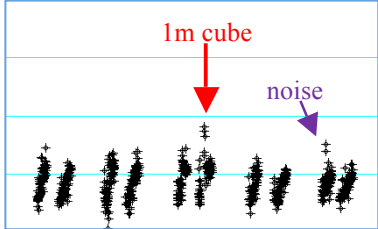
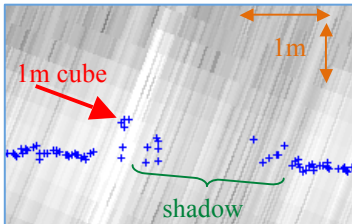
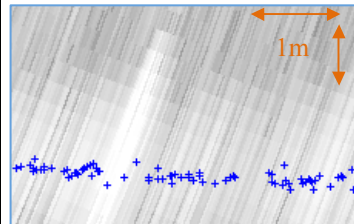
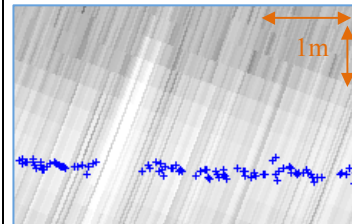

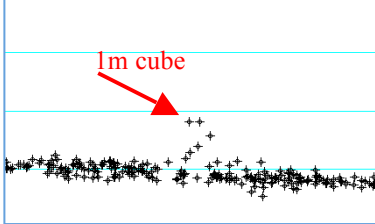
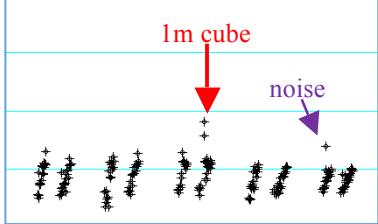
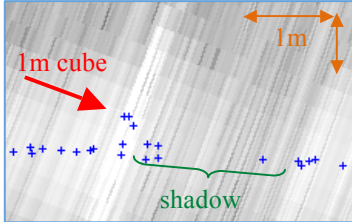
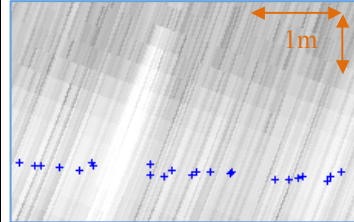
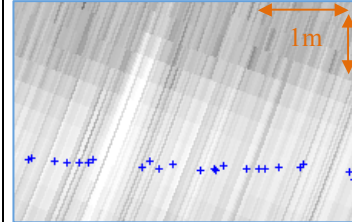
| 2014 Dataset | 40 m Depth | 72° Angular Sector | 1-meter Cube | Line 0010 | +68° Incidence Angle |
|---|--|---|---|-----------|----------------------|
| KM solutions | | | | | |
| Bathymetric surface | Across-track sounding profile | | Along-track sounding profile | | |
|  |  | |  | | |
| BDI solutions – manual threshold 0 dB, uncompressed data | | | | | |
| Bathymetric surface | Across-track sounding profile | | Along-track sounding profile | | |
|  |  | |  | | |
| WC sections – three consecutive swaths | | | | | |
|  |  |  | | | |
| BDI solutions – manual threshold 0 dB, compressed data | | | | | |
| Bathymetric surface | Across-track sounding profile | | Along-track sounding profile | | |
|  |  | |  | | |
| WC sections – three consecutive swaths | | | | | |
|  |  |  | | | |

Table 4.4: 1-meter cube at 40 m depth - automatic threshold BDI, 2014 dataset, +68° incidence angle

| 2014 Dataset | 40 m Depth | 72° Angular Sector | 1-meter Cube | Line 0010 | +68° Incidence Angle |
|---|--|---|---|-----------|----------------------|
| KM solutions | | | | | |
| Bathymetric surface | Across-track sounding profile | | Along-track sounding profile | | |
|  |  | |  | | |
| BDI solutions – automatic threshold, uncompressed data | | | | | |
| Bathymetric surface | Across-track sounding profile | | Along-track sounding profile | | |
|  |  | |  | | |
| WC sections – three consecutive swaths | | | | | |
|  |  |  | | | |
| BDI solutions – automatic threshold, compressed data | | | | | |
| Bathymetric surface | Across-track sounding profile | | Along-track sounding profile | | |
|  |  | |  | | |
| WC sections – three consecutive swaths | | | | | |
|  |  |  | | | |

For both analyzed cases, no real-time KM detection was achieved. Possible reasons for these unsuccessful detections are those previously discussed in section 2.3. The KM across- and along-track sounding profiles show no indication of the target presence. The along-track image of the $+68^\circ$ incidence (Table 4.3 or 4.4) reveals the shadow cast by the target, although the corresponding image of the $+67^\circ$ (Table 4.1 or 4.2) does not. As evidenced by the KM bathymetric surfaces, this may be justified by the longer shadow at the $+68^\circ$ incidence, when compared with the $+67^\circ$, for the same area presentation. The difference in size of the shadows (data gaps) can easily be identified in the bathymetric grids.

Concerning BDI solutions, a successful detection was made for all different modes in both analyzed cases. Although some spurious positive soundings (noise) are noticed, the solutions over the target, which are about 1 m above the surrounding seafloor, markedly show its existence. In this regard, the across-track sounding profiles provide the better way to assess the detection, as the slight slope of the seafloor across-track in the area may camouflage the target in the along-track profiles. Additionally, the compression applied to the data has indeed contributed to eliminate noise (“spikes”) both in manual and in automatic thresholding BDI, thus making the neighboring bottom smoother (as it probably is).

Although no data gap is observed in the BDI bathymetric surfaces, the target is not clearly discriminated. With a great, though subjective, visual effort, it is possible to distinguish the 1-meter cube at the $+67^\circ$ incidence in the bathymetric grids of manual threshold BDI (Table 4.1). That difficulty may largely be explained by the worse solutions quality at the outer beams, which is due primarily to refraction issues. This

causes a ribbing in the along-track direction, masking the target. Additionally, at the very low grazing angles, as the top face of the target, compared with the inboard face, is poorly ensonified, the target becomes distorted, making it seem small at the across-track aspect. This also hampers the target visualization.

The lack of data gaps in the BDI bathymetric surfaces indicates that the BDI algorithm can provide solutions in the target shadow area. As can be seen in the WC snapshots over the target, for all analyzed cases, BDI delivers many soundings in that area, but not for the whole area.

Furthermore, note that the BDI algorithm especially improves across-track solution density. In contrast, no improvement is observed in the along-track direction, as the swath density does not change with the application of BDI. Also, the successful detection of the target under data compression for a maximum of 400 soundings attests to the BDI ability to resolve low-grazing-angle targets adequately even when limited to the same maximum number of KM solutions.

4.5.2 1-meter cube at 20 m depth

Tables 4.5 and 4.6 present the results from the 2013 dataset for a 1-meter cube at 20 m depth and ensonified at -65° by applying manual and automatic threshold BDI, respectively. Tables 4.7 and 4.8 present the results for the same target and dataset, but ensonified at $+71^\circ$.

Table 4.5: 1-meter cube at 20 m depth - manual threshold BDI, 2013 dataset, -65° incidence angle

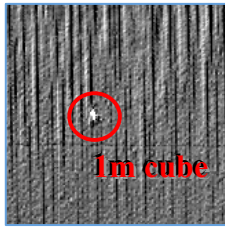
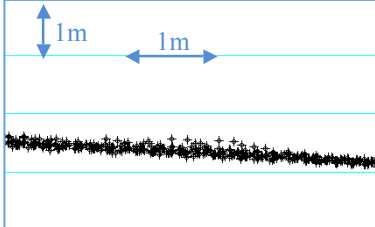
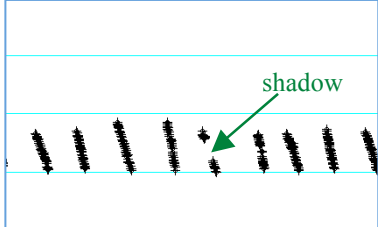
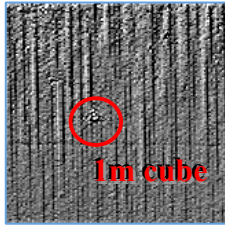
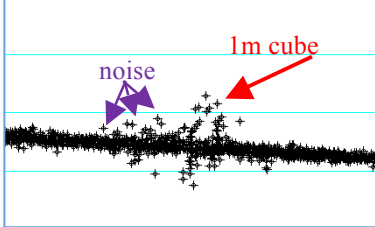
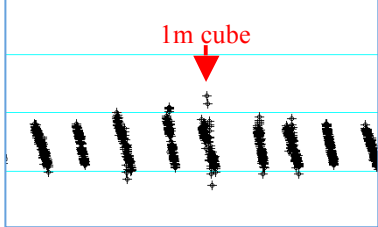
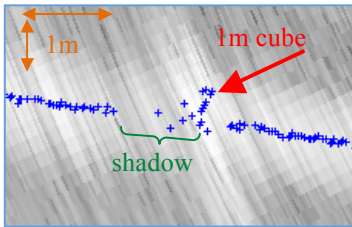
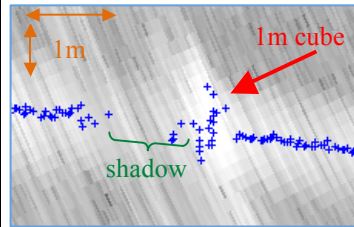
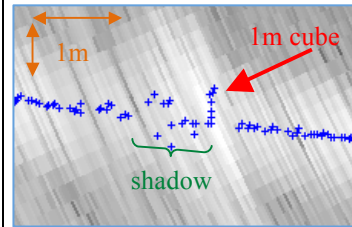
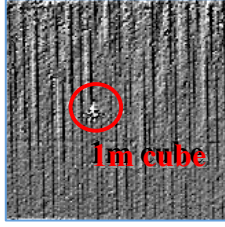
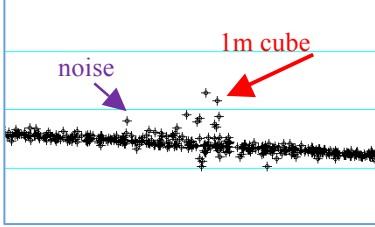
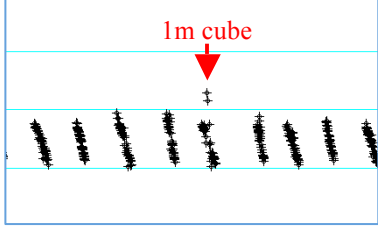
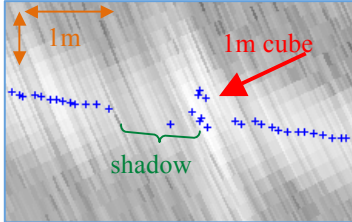
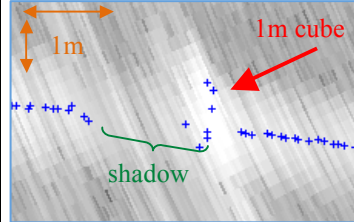
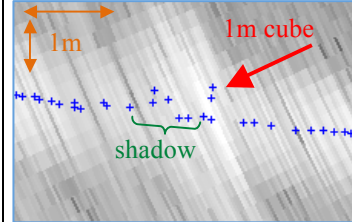
| 2013 Dataset | 20 m Depth | 75° Angular Sector | 1-meter Cube | Line 0011 | -65° Incidence Angle |
|---|--|---|---|--------------|-------------------------|
| KM solutions | | | | | |
| Bathymetric surface | Across-track sounding profile | | Along-track sounding profile | | |
|  |  | |  | | |
| BDI solutions – manual threshold 0 dB, uncompressed data | | | | | |
| Bathymetric surface | Across-track sounding profile | | Along-track sounding profile | | |
|  |  | |  | | |
| WC sections – three consecutive swaths | | | | | |
|  |  |  | | | |
| BDI solutions – manual threshold 0 dB, compressed data | | | | | |
| Bathymetric surface | Across-track sounding profile | | Along-track sounding profile | | |
|  |  | |  | | |
| WC sections – three consecutive swaths | | | | | |
|  |  |  | | | |

Table 4.6: 1-meter cube at 20 m depth - automatic threshold BDI, 2013 dataset, -65° incidence angle

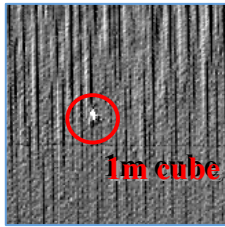
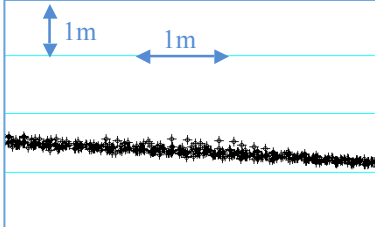
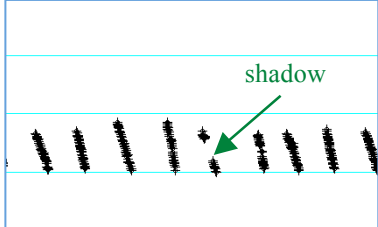
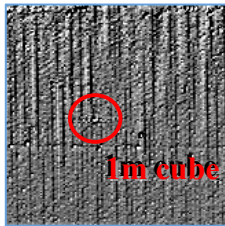
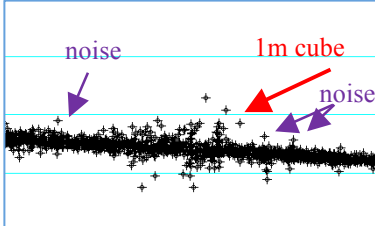
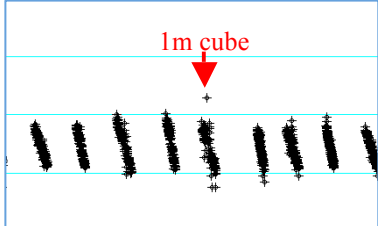
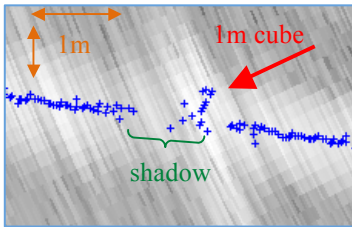
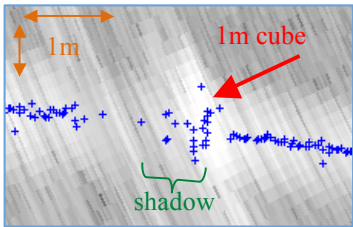
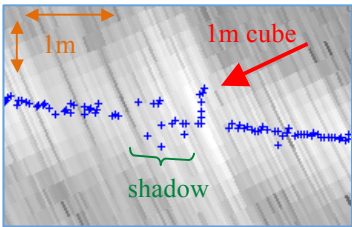
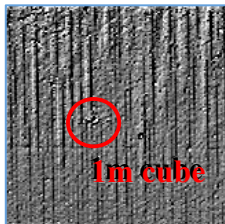
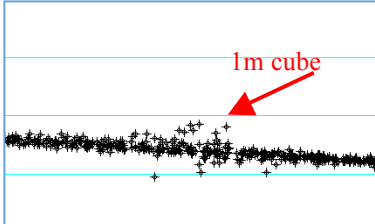
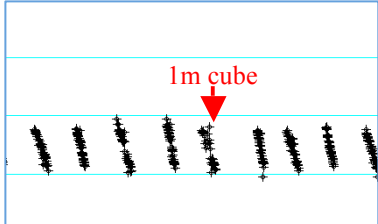
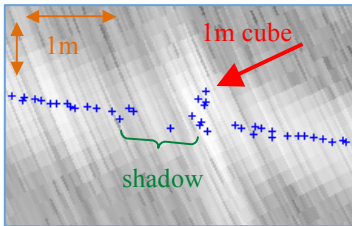
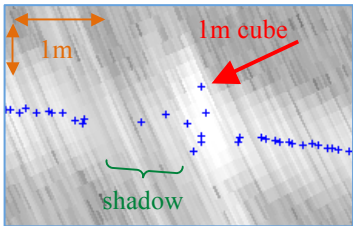
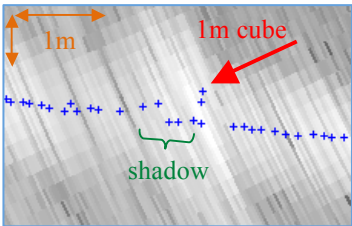
| 2013 Dataset | 20 m Depth | 75° Angular Sector | 1-meter Cube | Line 0011 | -65° Incidence Angle |
|---|--|---|---|-----------|----------------------|
| KM solutions | | | | | |
| Bathymetric surface | Across-track sounding profile | | Along-track sounding profile | | |
|  |  | |  | | |
| BDI solutions – automatic threshold, uncompressed data | | | | | |
| Bathymetric surface | Across-track sounding profile | | Along-track sounding profile | | |
|  |  | |  | | |
| WC sections – three consecutive swaths | | | | | |
|  |  |  | | | |
| BDI solutions – automatic threshold, compressed data | | | | | |
| Bathymetric surface | Across-track sounding profile | | Along-track sounding profile | | |
|  |  | |  | | |
| WC sections – three consecutive swaths | | | | | |
|  |  |  | | | |

Table 4.7: 1-meter cube at 20 m depth - manual threshold BDI, 2013 dataset, +71° incidence angle

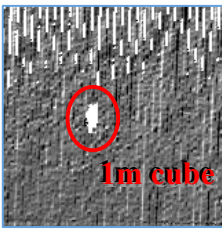
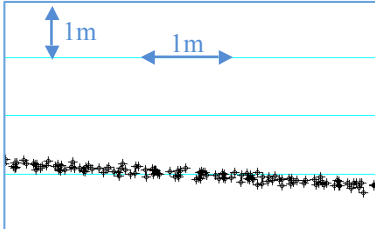
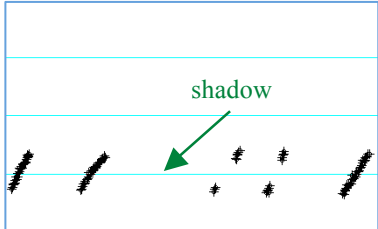
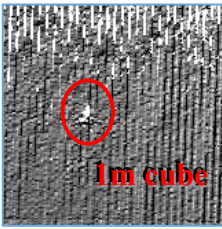
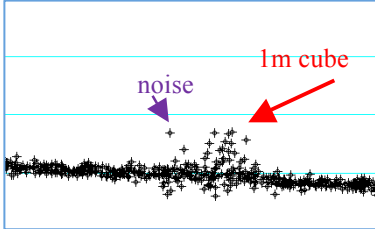
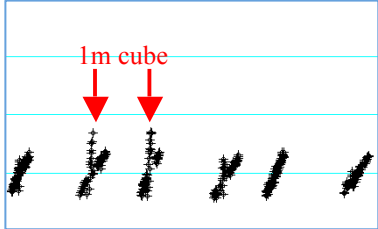
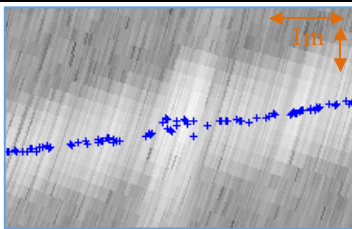
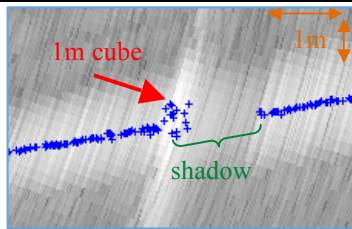
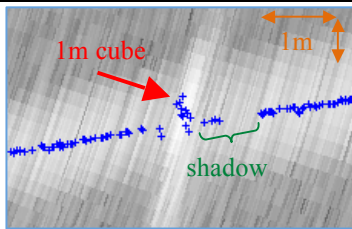
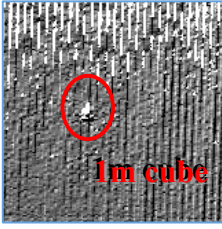
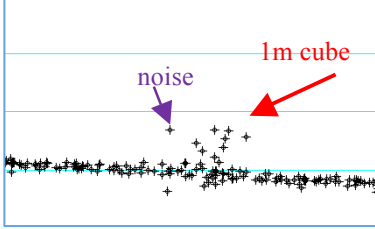
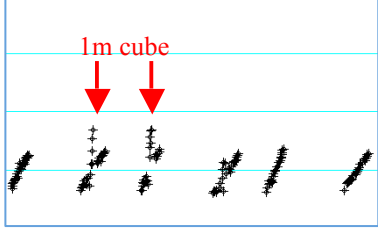
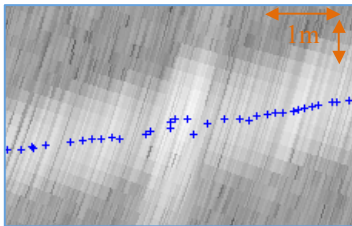
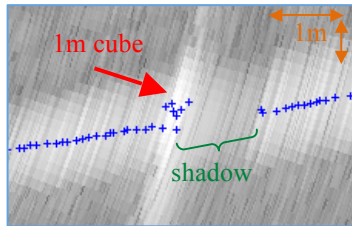
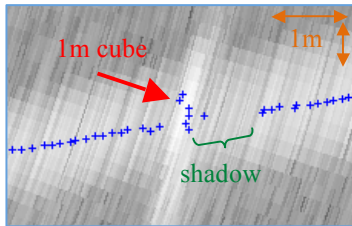
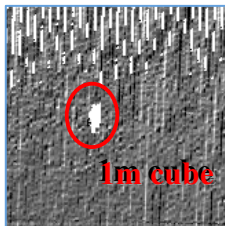
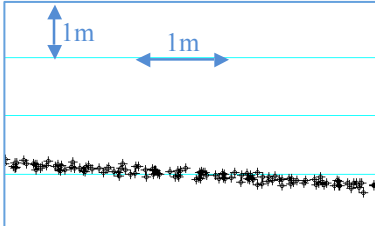
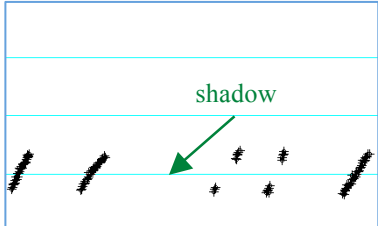
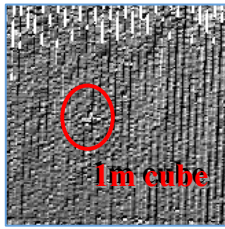
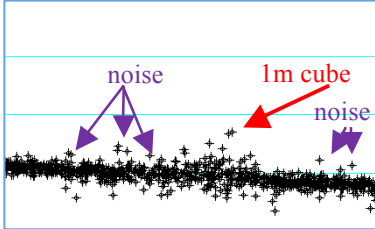
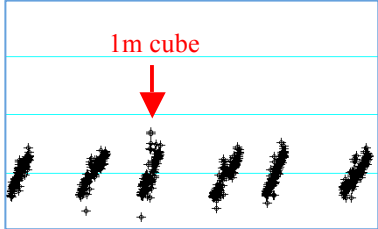
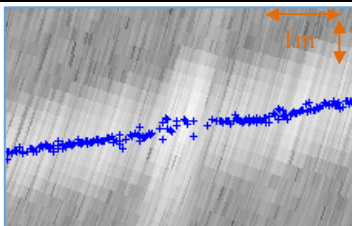
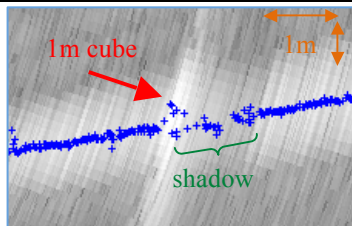
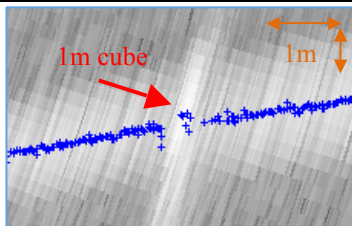
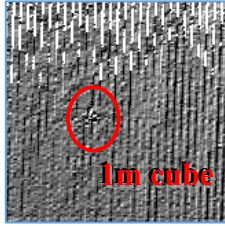
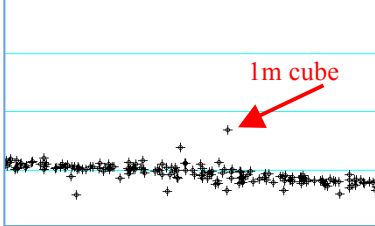
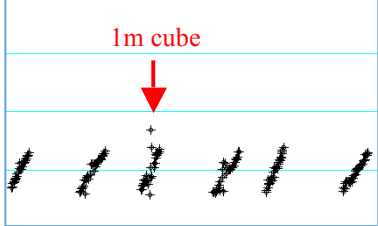
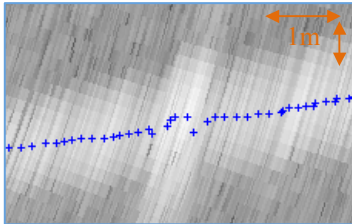
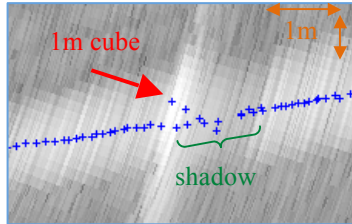
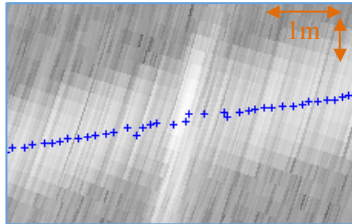
| 2013 Dataset | 20 m Depth | 82° Angular Sector | 1-meter Cube | Line 0010 | +71° Incidence Angle |
|---|--|---|---|-----------|----------------------|
| KM solutions | | | | | |
| Bathymetric surface | Across-track sounding profile | | Along-track sounding profile | | |
|  |  | |  | | |
| BDI solutions – manual threshold 0 dB, uncompressed data | | | | | |
| Bathymetric surface | Across-track sounding profile | | Along-track sounding profile | | |
|  |  | |  | | |
| WC sections – three consecutive swaths | | | | | |
|  |  |  | | | |
| BDI solutions – manual threshold 0 dB, compressed data | | | | | |
| Bathymetric surface | Across-track sounding profile | | Along-track sounding profile | | |
|  |  | |  | | |
| WC sections – three consecutive swaths | | | | | |
|  |  |  | | | |

Table 4.8: 1-meter cube at 20 m depth - automatic threshold BDI, 2013 dataset, +71° incidence angle

| 2013 Dataset | 20 m Depth | 82° Angular Sector | 1-meter Cube | Line 0010 | +71° Incidence Angle |
|---|--|---|---|-----------|----------------------|
| KM solutions | | | | | |
| Bathymetric surface | Across-track sounding profile | | Along-track sounding profile | | |
|  |  | |  | | |
| BDI solutions – automatic threshold, uncompressed data | | | | | |
| Bathymetric surface | Across-track sounding profile | | Along-track sounding profile | | |
|  |  | |  | | |
| WC sections – three consecutive swaths | | | | | |
|  |  |  | | | |
| BDI solutions – automatic threshold, compressed data | | | | | |
| Bathymetric surface | Across-track sounding profile | | Along-track sounding profile | | |
|  |  | |  | | |
| WC sections – three consecutive swaths | | | | | |
|  |  |  | | | |

Similarly to the 1-meter cube at 40 m depth, no real-time KM detection was achieved. The KM across-track sounding profiles, which offer the best way to discern a possible seabed object, show no indication of the target presence. Only a bathymetric gap immediately after the target (shadow area) can be observed in the along-track sounding profiles and in the bathymetric grids.

With respect to the BDI solutions, a successful detection was made for all different modes in both analyzed cases. The same analysis performed for the 1-meter cube examples at 40 m depth is valid here. Additionally, note that in general the user-defined threshold BDI approach provides better results, as can be seen in all 1-meter cube examples at 40 and 20 m deep. Automatic threshold BDI usually produces more false solutions around target vicinity, even though the target is always detected. The automatic thresholding algorithm developed for this research is a convenient method to calculate the BDI solutions without user interference or previous data analysis, although some improvements are still needed for a more reliable seafloor representation.

4.5.3 0.5-meter cube at 20 m depth

Tables 4.9 and 4.10 present the results from the 2013 dataset for a 0.5-meter cube at 20 m depth and ensonified at $+57^\circ$ by applying manual and automatic threshold BDI, respectively. Tables 4.11 and 4.12 present the results from the 2014 dataset for the same target, but ensonified at $+70^\circ$.

Table 4.9: 0.5-meter cube at 20 m depth - manual threshold BDI, 2013 dataset, +57° incidence angle

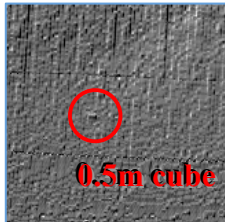
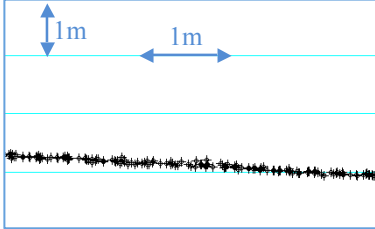
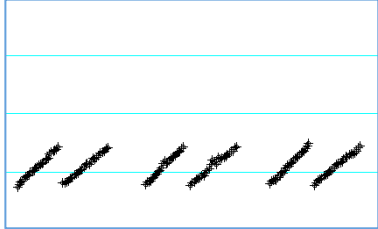
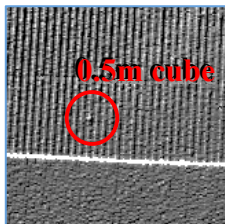
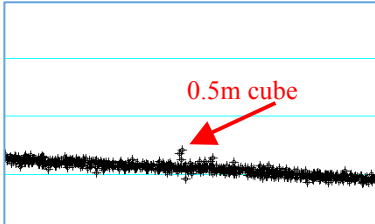
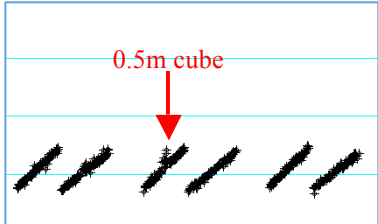
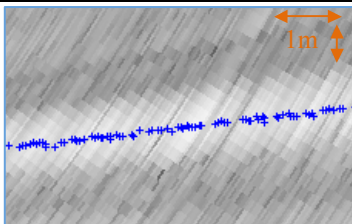
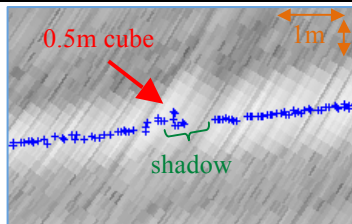
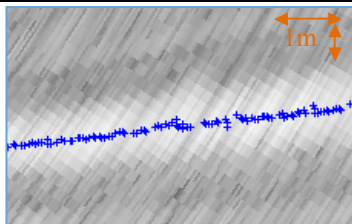
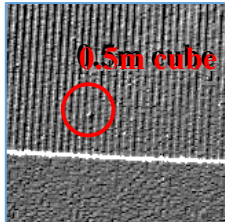
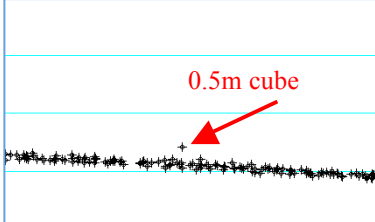
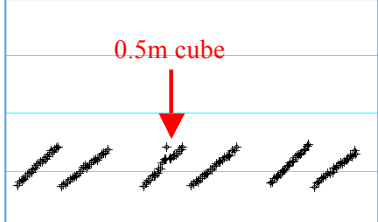
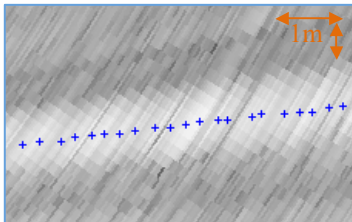
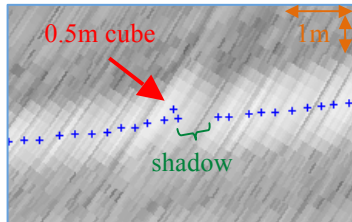
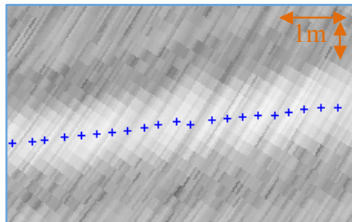
| 2013 Dataset | 20 m Depth | 82° Angular Sector | 0.5-meter Cube | Line 0012 | +57° Incidence Angle |
|---|--|---|---|-----------|----------------------|
| KM solutions | | | | | |
| Bathymetric surface | Across-track sounding profile | | Along-track sounding profile | | |
|  |  | |  | | |
| BDI solutions – manual threshold 0 dB, uncompressed data | | | | | |
| Bathymetric surface | Across-track sounding profile | | Along-track sounding profile | | |
|  |  | |  | | |
| WC sections – three consecutive swaths | | | | | |
|  |  |  | | | |
| BDI solutions – manual threshold 0 dB, compressed data | | | | | |
| Bathymetric surface | Across-track sounding profile | | Along-track sounding profile | | |
|  |  | |  | | |
| WC sections – three consecutive swaths | | | | | |
|  |  |  | | | |

Table 4.10: 0.5-meter cube at 20 m depth - automatic threshold BDI, 2013 dataset, +57° incidence angle

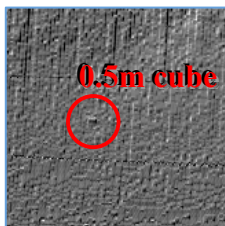
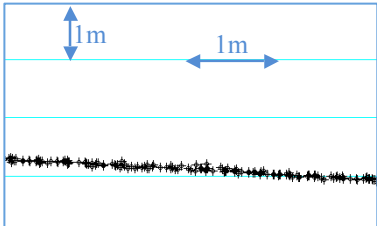
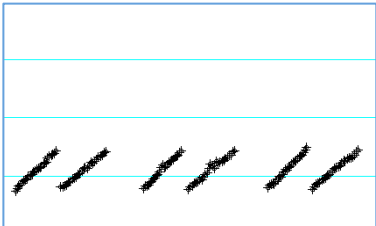
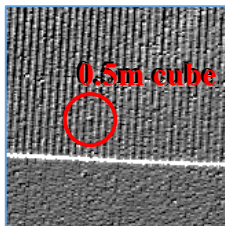
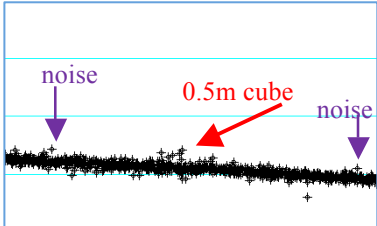
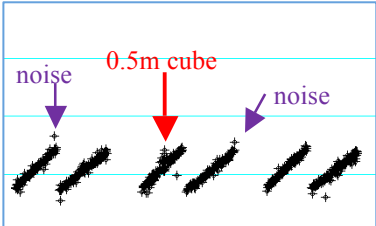
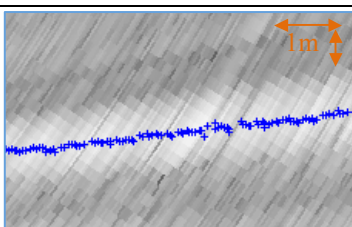
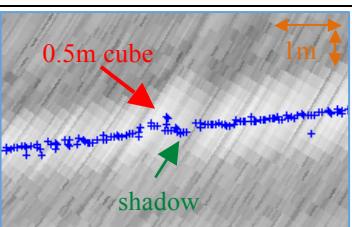
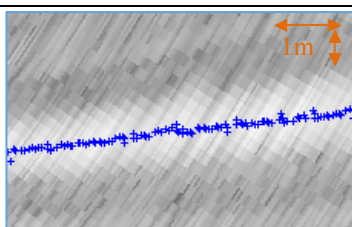
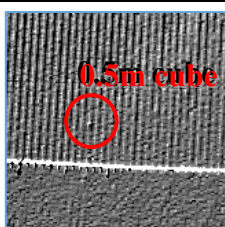
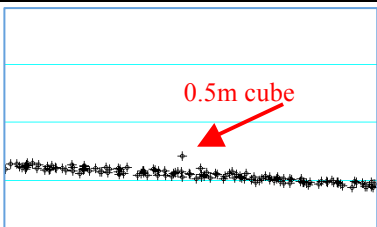
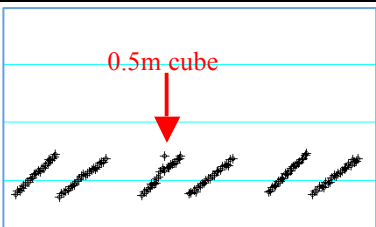
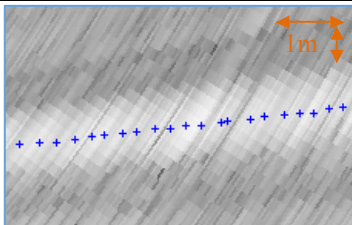
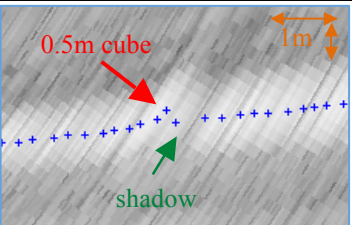
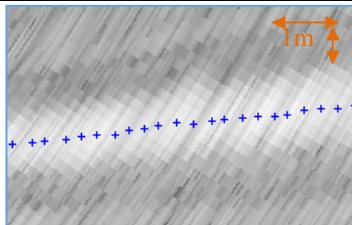
| 2013 Dataset | 20 m Depth | 82° Angular Sector | 0.5-meter Cube | Line 0012 | +57° Incidence Angle |
|---|--|---|---|-----------|----------------------|
| KM solutions | | | | | |
| Bathymetric surface | Across-track sounding profile | | Along-track sounding profile | | |
|  |  | |  | | |
| BDI solutions – automatic threshold, uncompressed data | | | | | |
| Bathymetric surface | Across-track sounding profile | | Along-track sounding profile | | |
|  |  | |  | | |
| WC sections – three consecutive swaths | | | | | |
|  |  |  | | | |
| BDI solutions – automatic threshold, compressed data | | | | | |
| Bathymetric surface | Across-track sounding profile | | Along-track sounding profile | | |
|  |  | |  | | |
| WC sections – three consecutive swaths | | | | | |
|  |  |  | | | |

Table 4.11: 0.5-meter cube at 20 m depth - manual threshold BDI, 2014 dataset, +70° incidence angle

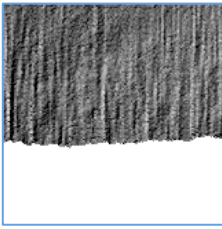
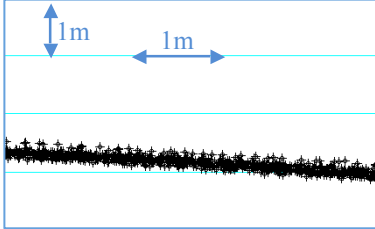
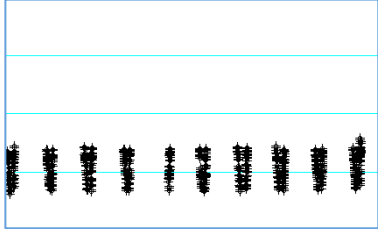
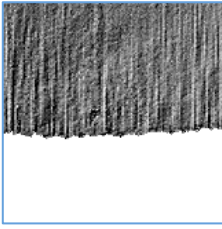
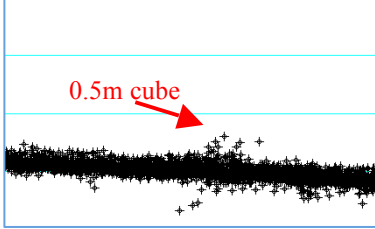
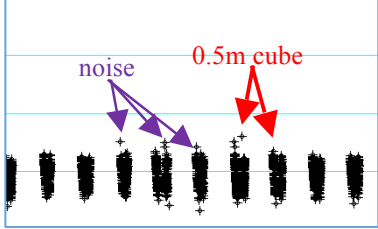
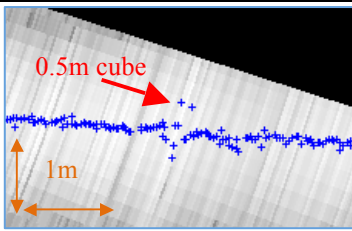
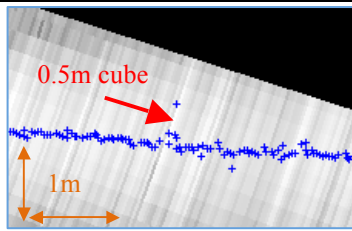
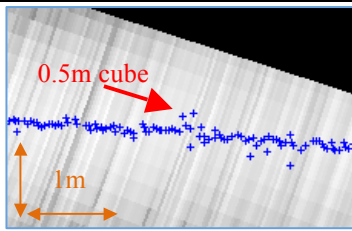
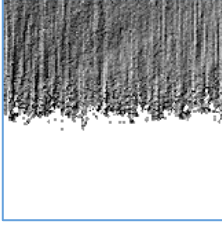
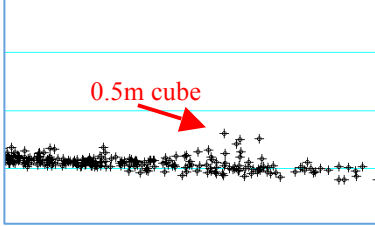
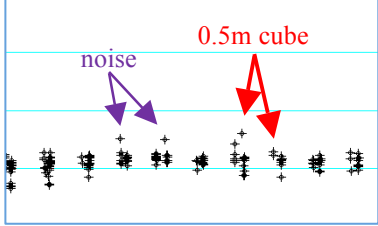
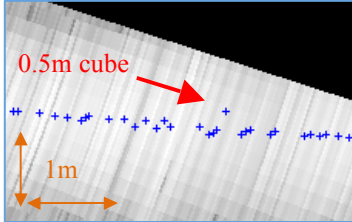
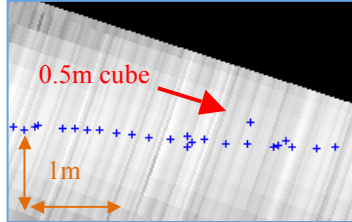
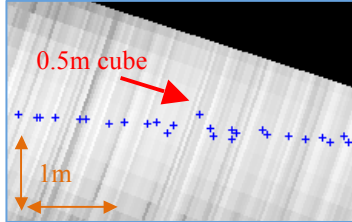
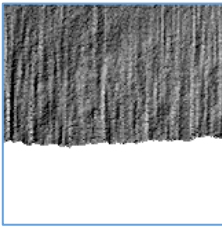
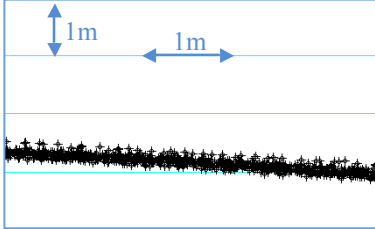
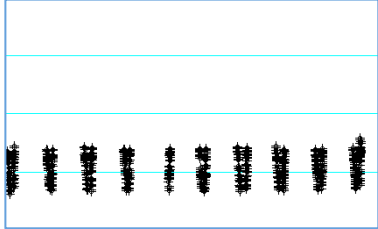
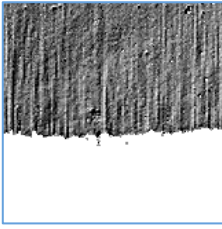
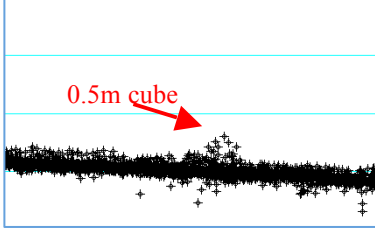
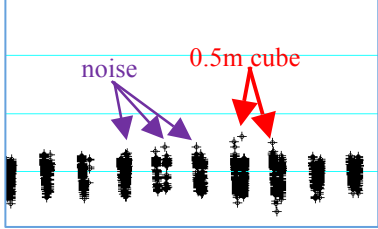
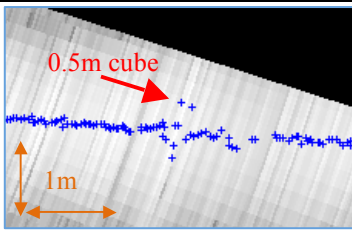
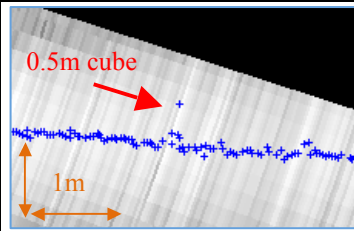
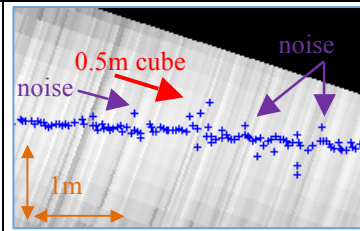
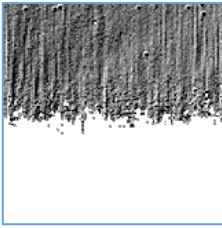
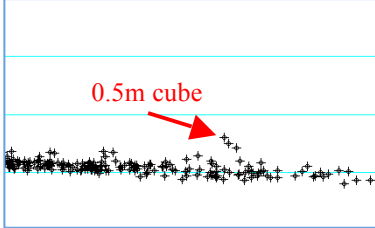
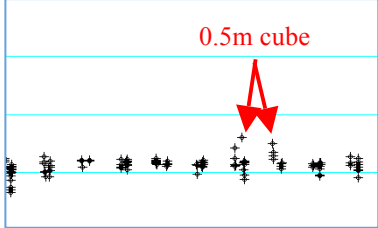
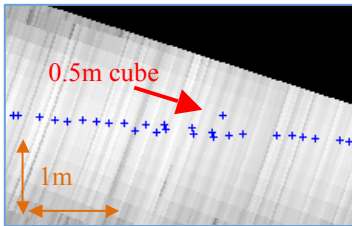
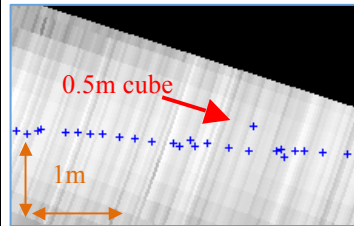
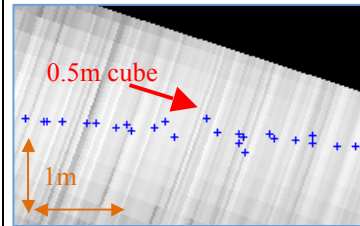
| 2014 Dataset | 20 m Depth | 72° Angular Sector | 0.5-meter Cube | Line 0018 | +70° Incidence Angle |
|---|--|---|---|-----------|----------------------|
| KM solutions | | | | | |
| Bathymetric surface | Across-track sounding profile | | Along-track sounding profile | | |
|  |  | |  | | |
| BDI solutions – manual threshold 0 dB, uncompressed data | | | | | |
| Bathymetric surface | Across-track sounding profile | | Along-track sounding profile | | |
|  |  | |  | | |
| WC sections – three consecutive swaths | | | | | |
|  |  |  | | | |
| BDI solutions – manual threshold 0 dB, compressed data | | | | | |
| Bathymetric surface | Across-track sounding profile | | Along-track sounding profile | | |
|  |  | |  | | |
| WC sections – three consecutive swaths | | | | | |
|  |  |  | | | |

Table 4.12: 0.5-meter cube at 20 m depth - automatic threshold BDI, 2014 dataset, +70° incidence angle

| 2014 Dataset | 20 m Depth | 72° Angular Sector | 0.5-meter Cube | Line 0018 | +70° Incidence Angle |
|---|--|---|---|-----------|----------------------|
| KM solutions | | | | | |
| Bathymetric surface | Across-track sounding profile | | Along-track sounding profile | | |
|  |  | |  | | |
| BDI solutions – automatic threshold, uncompressed data | | | | | |
| Bathymetric surface | Across-track sounding profile | | Along-track sounding profile | | |
|  |  | |  | | |
| WC sections – three consecutive swaths | | | | | |
|  |  |  | | | |
| BDI solutions – automatic threshold, compressed data | | | | | |
| Bathymetric surface | Across-track sounding profile | | Along-track sounding profile | | |
|  |  | |  | | |
| WC sections – three consecutive swaths | | | | | |
|  |  |  | | | |

The same analysis for the 1-meter cube at 40 m depth is valid here for this 0.5-meter cube at 20 m depth. A data gap in the along-track profile for the KM solutions is not observed in both analyzed cases, likely because of the smaller object size for the same area presentation. Additionally, note that the KM bottom detection algorithm was not able to detect a 0.5-meter cube at 20 m depth even at an incidence angle smaller than 60° ($+57^\circ$, Tables 4.9 or 4.10). This happened because the sector limit of detection decreases with the reduction of the object size. A $\pm 60^\circ$ angular sector is not enough to assure a 0.5-meter cube detection at 20 m depth with the current KM algorithm based only on WMT and phase detection (Hughes Clarke, 2014). For the second analyzed case, what is remarkable to point out is the fact that the BDI approach can confidently detect such a small feature (0.5-meter cube) at such a low grazing angle (20°).

5. Conclusions

5.1 Summary

The well-established and widespread joint use of WMT and phase detection for the multibeam bottom calculation has many benefits, even though some weaknesses may appear in situations such as a high-aspect-ratio object ensonified at low grazing angles. Even with a system endowed with the required range and angular resolution to resolve a seabed object, the within-beam layover and the bottom detection filters applied by Kongsberg® might omit a potentially resolvable feature. When these situations occur, an alternative method based on the BDI technique has proven to be a better approach.

The aim of this research was to investigate the potential BDI ability to better detect/define IHO-compliant objects at low grazing angles in shallow waters, especially when the so-called conventional real-time bottom detection algorithms fail. For this purpose, all performed tests have demonstrated that the non-conventional BDI method always detects the target when WMT and phase detection do not, including a sub-IHO object of the size of a 0.5-meter cube at 20 m deep as an opportunistic test of potential MLO detection. In addition, BDI is also able to provide solutions even in the target shadow area, which may improve the overall seafloor representation.

Although this research was based on, and tailored, to the EM 2040D, the developed BDI algorithm might be applied to any echosounder whose manufacturer provides WC data for a post-acquisition analysis, or even might be added to the current algorithms. In this regard, surely incorporating BDI into the manufacturers' bottom detection algorithms in addition to WMT and phase detection may be a positive approach toward a better multibeam target detection/definition at low grazing angles in

shallow waters. If an appropriate algorithm that smartly chooses one of the three techniques for each unique situation is developed, certainly a more reliable seafloor representation will be accomplished.

5.2 Future Work

The BDI algorithm developed for this research certainly is not a finished product. It was tailored to best suit the datasets used to test it. Improvements still needed include:

- (1) The use of all samples above noise within the effective receiver main-lobe beamwidth rather than only three or five in the parabola fitting process.
- (2) Addressing and accounting for the non-symmetric shape of the receiver main-lobe beamwidth (including distortion due to the TVG), also in the parabola fitting process.
- (3) Assessing the apparent width of the receiver main lobe as described by the parabola fit and comparing it to the modeled width as a way of looking for evidence of layover (which would artificially widen the parabola).
- (4) Considering all possible BDI solutions per TWTT rather than only a maximum of two.
- (5) Refinements both in the automatic thresholding calculation and in the filtering algorithm to better eliminate the spurious solutions (noise) above the seafloor.
- (6) Accounting for the irregular seabed topography instead of the flat assumption when compressing the data.
- (7) Coping with detection of targets near the sector boundaries.

5.3 Contribution

Three significant research contributions can be enumerated:

- (1) Confidently reveal the existence of a resolvable small target (when it really exists) at low grazing angles in shallow waters.
- (2) Potentially allow surveyors to shorten the survey time of any seabed object-finding mission in shallow waters, as a reliable wider swath may be considered.
- (3) Reinforce the concept that an integrated WMT, phase detection, and BDI techniques in the same system provides the best bottom detection results (de Moustier, 2009; Hughes Clarke *et al.*, 2013).

Bibliography

- Davis, P.J. (1975). Interpolation and approximation. New York: Dover Publications, Inc.
- de Moustier, C. (1993). Signal processing for swath bathymetry and concurrent seafloor acoustic imaging, in *Acoustic Signal Processing for Ocean Exploration*, J. M. F. Moura and I. M. G. Lourtie, Eds, The Netherlands: Kluwer, 329-354.
- de Moustier, C. (2009). Bottom detection methods. Lecture Notes No. 10, 51st Multibeam Sonar Training Course, Rio de Janeiro, Brazil, 23-28 November.
- Hammerstad, E., Pohner, F. & Bennett, J. (1991). Field testing of a new deep water multibeam echo-sounder. *Proceedings of the IEEE Oceans '91*, 2, 743-749.
- Hammerstad, E. (2008). Multibeam Echo Sounder Accuracy. Kongsberg EM Technical Note.
- Hughes Clarke, J.E. (1998). The effect of fine scale seabed morphology and texture on the fidelity of swath bathymetric sounding data. *Proceedings of the Canadian Hydrographic Conference*, 168-181.
- Hughes Clarke, J.E. (2006). Applications of multibeam Water Column Imaging for hydrographic survey. *Hydrographic Journal*, 120(1), 3-14.
- Hughes Clarke, J.E. (2009). USNS Sumner (TAGS-61) - EM710 and EM122 Assessment. January 14th-28th, 2009, Vicinity of Saipan and Guam. Contract to U.S. Naval Oceanographic Office, via Mantech Ltd.
- Hughes Clarke, J.E. (2010). USNS Heezen (TAGS-63) - EM710 Assessment. April 16th to May 8th, 2010, Vicinity of Saipan and Guam. Contract to U.S. Naval Oceanographic Office, via Mantech Ltd.
- Hughes Clarke, J.E. (2013a). HSL-16 - EM2040 dual v. single head trials. September 21st to October 21st, 2012, Orange Beach, Alabama. Contract to U.S. Naval Oceanographic Office, via Mantech Ltd.
- Hughes Clarke, J. E. (2013b). Imaging and Mapping II Course. Lecture Notes, Department of Geodesy and Geomatics Engineering, University of New Brunswick, Fredericton, Canada.
- Hughes Clarke, J.E., Martinolich, R. & Smith, G. (2013). EM 2040 / EM 710 target detection trials: What qualifies as a successful detection? *Forum for Exchange of Mutual Multibeam Experiences (FEMME)*, Boston, USA, April 18th (presentation only).

- Hughes Clarke, J.E. (2014). HSL-16 - EM2040D Trials. Institute of Ocean Sciences, Sidney, BC, July. Contract report to U.S. Naval Oceanographic Office.
- International Hydrographic Organization (2005). Manual on Hydrography – Publication C-13 (1st Edition). International Hydrographic Bureau, Monaco.
- International Hydrographic Organization (2008). IHO Standards for Hydrographic Surveys – Special Publication No. 44 (5th Edition). International Hydrographic Bureau, Monaco.
- Kongsberg Maritime (2012). EM 2040 Multibeam Echo Sounder – Product description. Horten, Norway.
- Kongsberg Maritime (2013). EM Series Multibeam Echo Sounders – Datagram formats. Horten, Norway.
- Lurton, X. (2010). An Introduction to Underwater Acoustics – Principles and Applications (Second Edition). London: Springer / Praxis Publishing.
- Nilsen, K.E. (2011). Kongsberg EM 2040 introduction course. Horten, Norway.
- Nilsen, K.E. (2012). Kongsberg EM 2040 bottom detection course. Horten, Norway.
- Satriano, J.H., Smith, L.C. & Ambrose, J.T. (1991). Signal processing for wide swath bathymetric sonars. *Proceedings of the IEEE Oceans'91*, 1, 558-561.
- SeaBeam Instruments (2000). Multibeam sonar theory of operation (Manual), East Walpole, USA.
- van der Werf, A. (2010). Mast tracking capability of EM 3002D using Water Column Imaging. M.Sc.E. thesis, Department of Geodesy and Geomatics Engineering, University of New Brunswick, Fredericton, Canada.
- Rubrio Videira Marques, C. (2012). Automatic mid-water target detection using multibeam water column. M.Sc.E. thesis, Department of Geodesy and Geomatics Engineering, University of New Brunswick, Fredericton, Canada.

Curriculum Vitae

Candidate's full name: Douglas Luiz da Silva Pereira

Universities attended:

Directorate of Hydrography and Navigation (DHN)

City of Niterói, State of Rio de Janeiro, Brazil

January 2006 – December 2006

Extension course in Hydrography (IHO Category “A”)

Naval School

City of Rio de Janeiro, State of Rio de Janeiro, Brazil

January 1999 – December 2003

B.Sc. Naval Sciences (Major Electronics)

Conference Paper and Presentation:

Pereira, D.L.S. & Hughes Clarke, J.E. (2015). Improving shallow water multibeam target detection at low grazing angles. *Proceedings of the United States Hydrographic Conference 2015*.